Input and state estimation for compliant motion stages

Estimating modal contributions for guidance flexures

Pim de Bruin

Master Thesis

TU Delft Delft University of Technology

Delft Center for Systems and Control
Department of Precision and Micsorystems Engineering

Input and state estimation for compliant motion stages

Estimating modal contributions for guidance flexures

Master Thesis

For the degree of Master of Science in Mechanical and Control Engineering at Delft University of Technology

Pim de Bruin

October 7, 2022

Faculty of Mechanical, Maritime and Materials Engineering (3mE)
Delft University of Technology

Preface

For the purpose of graduating an Individual Double Degree program between the master programs High-Tech Engineering and Systems & Control, this work documents the process and results of my thesis project.

During the last year, this project has gone from a vague application field and requirements to a proper proposal followed by execution. I am therefore grateful to present the final results of this effort which has truly explored all ranges of mechanical, mechatronics and control engineering. At the end of it, I am still baffled by the shear amount of knowledge from all sorts of fields required to bring such a project to a successful end. From creativity, organisational, and academic skills at the beginning of the literature research, to electrical, mechanical, control engineering and computer science during actual implementation. Even my skills at the mill were put to the test. I am therefore grateful for the time I have spent at Delft University of Technology developing at least the basic skills in these areas, for the entirety of my years spent here was definitely necessary.

While finding a suitable subject area and research question to satisfy the requirements for both master programs was challenging, the actual implementation and execution of the project described in this work has been a challenge in many more ways. Many of which not represented in this work. Even attempting relatively simple integration steps require a lot more work and thorough understanding then expected, especially when working on embedded systems like the one used here.

Even though the process has been long, and much more involved then expected, I am satisfied with the result as it covers everything from theoretical evaluation to physical implementation. The completeness of the project has however left some things to be desired in evaluation, where more thorough or in-depth result validation might have been appropriate. A compromise between completeness and depth had to be struck here however due to time constraints. Nevertheless a complete work has been delivered.

Al in all, I would like to thank my supervisors Manon Kok and Hassan HosseinNia for their guidance and time. In addition, I would like to thank Marcin Kaczmarek for the endless availability and involvement in the project as daily supervisor.

Abstract

To improve Active Vibration control methods like Independent Modal Space Control (IMSC), an estimate of the modal contribution of vibrational eigenmodes of compliant structures is required. In this work, three Recursive Bayesian input and state estimation algorithms previously introduced in civil engineering are evaluated for use on on high-tech compliant mechanisms to estimate modal contributions for use in Active Vibration Control. The difference in environment when applying these algorithms from civil engineering into high-tech compliant motion stages allows for a significantly different sensor configuration possibly improving estimation performance.

The three algorithms, namely, the Augmented Kalman Filter (AKF), Dual Kalman Filter (DKF) and Gilijns de Moor Filter (GDF) are implemented in simulation and on an experimental compliant motion stage setup. The modal contributions of the guidance flexures are estimated through a noisy acceleration measurement at the stage and strain measurement at the flexure base.

For validation, the filters are evaluated on overall fit quality and system acceleration dependency through the quality of estimation of the flexure tip location. The DKF is shown worst performance with lowest fit scores overall and high acceleration dependency while the AKF and GDF perform comparably well. The GDF is shown to transmit less noise into the estimate however, and thus performed overall best.

Contents

Chapter 1

Introduction

The problem of moving produce and objects around during manufacturing has been an important one through the age of industrialisation. Now, with the dawn of digitisation, doing this with high accuracy has become a significant area of research. In addition to accuracy, high demands on production volume on for instance the silicon industry requires these handling solutions to move faster than they have before while maintaining accuracy specifications. Moving towards these high accuracy, high yield systems provides the base for a whole new set of problems to be solved.

One such problem is the problem of vibration. When moving at high speeds, components in the system will start to vibrate in unwanted vibrational modes introducing sources of error into the system, thus reducing possible achievable accuracy. Addressing this problem in a more traditional (passive) way would result in an increase in stiffness or damping of these components by either using more structural material, or applying passive damping elements like viscous layers or tuned mass dampers [1]. A major drawback of these solutions however is the addition of weight to the system [2], which is often highly undesired especially in fast moving motion systems. For these applications, active vibration control (AVC) could provide the required vibration attenuation, with decreased mass addition compared to passive solutions.

Active vibration control could thus help increase accuracy and yield for high precision motion systems. It is however noteworthy that the problem of vibration exists in a much wider range of research fields like civil engineering, or aerospace engineering where vibrations could decrease lifetime expectancy of structural components [3; 4; 5]. It is thus worthwhile to keep in mind the theory and results derived in this work can be applied to a wide range of similar problems in different engineering disciplines, which increases the motivation for research into the topic of active vibration control.

For this work however, the focus will mainly be active vibration control for compliant motion stages. To provide some framework and intuition for this, section 1-1 will sketch this application field. Hereafter, the problem in the state of the art, and thus the research gap that will be addressed in this work is introduced in section 1-2. The formal research objectives are

presented in section 1-3 followed up by a short overview of this work in section 1-4.

1-1 Background and motivation

To provide some intuition, and introduce compliant motion stages, subsection 1-1-1 discusses the general concept while also introducing the problem with vibration of these stages at high velocities. A short introduction to a possible solution for this, namely active vibration control, will be introduced in subsection 1-1-2.

1-1-1 Compliant motion stages

As sketched above, the problem of moving with high precision at high velocity provides a large area of research. One industry for instance facing this problem is the semiconductor industry, where the speed of translation of silicon wafers and degree of accuracy of processing steps limits production of much needed chips. One way of attempting to improve precision is through the use of compliant motion stages. An advantage of this over more traditional systems like linear- or air bearings is the lack of stick-slip and friction which makes for a very predictable motion system while retaining significant stiffness in the load carrying direction. Also, lubrication and friction wear are not of concern when using compliant guidance flexures since no sliding or rolling contact is present anywhere.

The general concept of a motion stage using compliant guidance flexures is presented in Figure 1-1a with its main operating mode in Figure 1-1b. Here, the stage itself is represented in black, being supported by two linear guidance flexures rigidly connected to a fixed world.

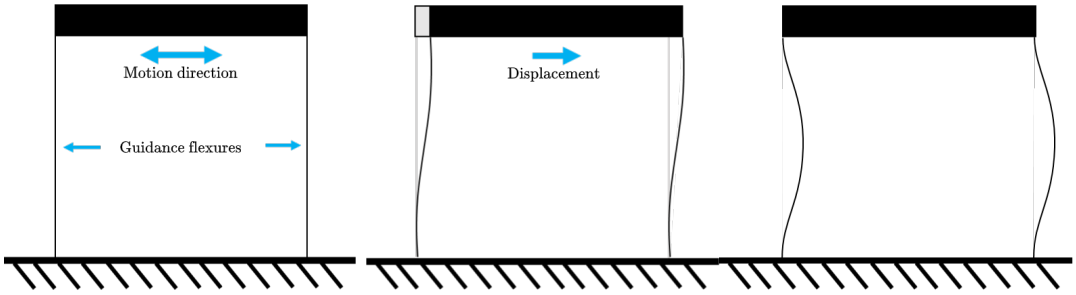

(a) General compliant motion stage concept **(b)** Deformed configuration during operation **(c)** Second vibrational mode flexure vibration

Figure 1-1: General compliant motion stage concept and operational modes.

When operating this stage at high bandwidth (high acceleration) however, higher vibrational modes of these flexures can be excited which can introduce transient vibrational forces on the stage body itself. For illustration, the second vibrational mode of these flexures is also presented in Figure 1-1c where it is already apparent this mode is not advantageous for the stage operation. Due to low inherent damping in the flexure material, the transient behaviour of these modes can remain present for extended amounts of time, and keep introducing disturbing vibrations into the positioning of the stage. It is thus required to add damping to these flexures. As mentioned before, passive methods can add significant mass which could negatively impact the possible bandwidth the stage can achieve. It is for this reason active vibration control is of much interest, as it could provide a low mass solution to this problem.

1-1-2 Active vibration control

Many - more traditional - ways of active vibration control only require collocated measurements and actuation, where one side of a structure like these compliant guidance flexures is fitted with an actuator, and the other with a sensor at the same location. The output of the sensor can then be fed back through a control algorithm like Positive Position Feedback (PPF) [6] or Direct Velocity Feedback (DVF) [7] to the actuator on the other side [8]. This is generally applied by using multiple sensor/actuator pairs on large strain locations of the structure, resulting in a fully decentralised control structure.

This way of active vibration control can be very effective for certain systems, and through its simplicity, is easily implementable [8]. For further introduction into this way of approaching the problem, the reader is referred to [8] as this will not be elaborated on further in this work.

For more complex control methods like Linear Quadratic Regulation (LQR) Model Predictive Control (MPC) or more specific active vibration control approaches like Independent Modal Space Control (IMSC), knowledge of the current deformation state of the system is required [9; 10]. In IMSC, the current vibrational state of the system is decomposed into its independent modal contributions, by which each mode can then be controlled independently through linear control techniques like PID or LQR. This allows for targeting specific modes without spending control energy on modes that are not of interest (for instance at high frequencies) and decomposing the MIMO problem of controlling multiple modes with multiple actuators into a set SISO problems of controlling in dependant modes. To do this, however, knowledge of the current modal contribution state of the system is required. This knowledge can not be obtained by a decentralised measurement system as used in PPF or DVF, and requires some sort of centralised estimation.

A solution for this, commonly found in literature, is the use of modal filters, as developed by L.Meirovitch and H.Baruh [9]. This approach makes use of the orthogonality principle of the mode shapes of a flexible structure to obtain the modal contributions desired for IMSC from a limited amount of discrete measurements, trough the use of a static gain matrix. These modal contributions represent the amount a single mode is contributing to the current state of vibration.

Due to the static nature of these modal filters however, they are sensitive to measurement and process noise which could limit the overal AVC scheme performance [9]. It is here the field of state estimation through Recursive Bayesian Filtering (RBF) is introduced.

In this field, the objective is to obtain real-time information about the current modal contribution states of the entire structure like the compliant flexure through the use of RBFs. These RBFs inherently assume a stochastic system model, allowing for process and measurement noise to be taken into account. This could improve modal contribution estimation compared to the traditional modal filters, and thus improve AVC performance overall.

1-2 Problem definition

When applying RBF modal contribution estimation to these systems however, it can be seen that more traditional methods like Kalman Filtering require information on the input to the system. This input can be anything from control forces used to move the stage, to probe testing of chip components, to general unknown disturbances. It is thus obvious

this information is hard to obtain in the real world without thorough modelling of the entire system which is not always possible or economic. To still obtain a modal contribution estimate however, the problem of simultaneous input and state estimation is introduced.

In the problem of simultaneous input and state estimation, the objective is to obtain an estimate of the input to a system together with an estimate of the current state of the system. This problem is present in almost all dynamical systems where the input can not directly be measured. Large research areas can be found in civil engineering, where wind loading on turbines or car loading on bridges can not directly be measured [11; 12] but an estimate of the deformation of the structure still is required for for instance Structural Health Monitoring (SHM). Here, a state estimate can be used to estimate strain loading on structural components, and therefore evaluate their lifetime or degradation. Is is also in this field that significant amounts of work exist on the use of RBFs, and their development.

For this work however, an attempt is made to address this problem for compliant guidance flexures of high precision motion stages with the aim of active vibration control. To the author's knowledge, no implementation of joint input and state estimation for motion stage guidance flexures has been made. An implementation and evaluation of possible algorithms can thus be regarded as a gap in the state of the art, and important problem to work on.

1-3 Research objectives

As established before, an estimate of the current modal contribution state of guidance flexures for compliant motion stages is desired, and has not yet been obtained through the use of joint input and state RBFs. An estimate of the current modal contribution state could yield interesting new performance increases through the ability to implement more complex control algorithms into active vibration control.

The field of SHM in civil engineering already developed solutions for this problem in the form of development and evaluation of multiple RBF solutions. In addition to this, the change of operating environment from civil structures to compliant motion stages provides some interesting possibilities in sensor configurations. For these civil structures for instance, strain measurements are hard to obtain, whereas acceleration measurements are cheap and easy. This unavailability of strain measurements can reduce estimate performance significantly as sketched by [13; 14] and [11]. For high-tech compliant mechanisms, however, these strain measurements are much easier to implement due to small system size and a highly controlled environment. In addition to this, high-tech systems often benefit from in-depth system knowledge allowing for accurate modelling which also benefits RBF implementation.

Applying methods from SHM on high-tech compliant motion stages could thus yield estimation performance increases, and is worthy of evaluation.

Among other approaches, like the Augmented Discrete Extended Kalman Filter (A-DEKF) [15] and proposed Maximum Aposteriori Prediction (MAP) based methods [16], three methods are often evaluated [12] for SHM, namely:

- **Augmented Kalman Filter (AKF)**
  As introduced in [17]. This approach shortly consists of a standard Kalman filter implementation using an autonomous system model formulation with augmented state and random walk assumption on the input dynamics.

- **Dual Kalman Filter (DKF)**
  As introduced in [14]. This approach consists of a standard Kalman filter implementation using a preceding extra Kalman filter providing a preliminary estimate of the input. Assuming a random walk model for the input dynamics as well.
- **Gilijns de Moor Filter (GDF)**
  As introduced in [18]. This approach consists of a standard Kalman filter implementation using a preceding minimum variance unbiased estimator for input estimation.

The main novelty of this work however is the evaluation of these three input and state estimation algorithms for high-tech compliant motion systems through implementation in simulation and an experimental motion stage setup. The general research question can thus be formulated as:

Which of the selected existing Bayesian simultaneous input and state estimation techniques is most viable for implementation on high precision compliant motion stage flexures?

For this research question, three main research objectives together with some sub objectives have been developed as intermediate objectives in the project as:

1. Build and test a suitable compliant motion stage setup
   (a) Build test setup
   (b) Implement actuation
   (c) Implement sensing
   (d) Implement closed loop position control
2. Build and validate system model
   (a) Build system model
   (b) Identify actual plant
   (c) Validate and tune system model
3. Validate filter performance in simulation
4. Implement off-line input and state estimation of three previously selected filters

Here, the first main objective will focus on the design and construction of a compliant motion stage, which will serve as test platform on which the filters can be tested. To be able to implement the desired filters, a model of the system needs to be set up as well, which serves as the second main objective, which is also constructed in simulation in the third objective. The fourth, and foremost objective then results in actually implementing the state estimation off-line on the motion stage setup. After this goal is reached, the results can be analysed, and conclusions about the feasibility of this input and state estimation and filter performance in the field of active vibration control can be drawn.

1-4 Outline

This work first shortly presents the contribution, method and results in paper format in Chapter 2. This summarises the remainder of the report, which is set up in a similar manner

containing more in-depth evaluations. These additional sections are constructed to be self-contained, not requiring the paper in Chapter 2 and presenting a similar story.

For these more in-depth evaluations, the required preliminaries are presented in Chapter 3 where section 3-1 first elaborates on the way the system boundary is defined, and section 3-1 the modelling procedure presents. Hereafter, section 3-2 presents the relevant algorithms.

To show validity of these filters, they are shortly evaluated in simulation in Chapter 4 on a system similar to the finally implemented true system. This completes the third research objective. Here however, no conclusions about performance can be made since they have to be implemented on the true system.

For the actual implementation on this true system, Chapter 5 elaborates more on the hardware and software side of this. In section 5-1, the experimental setup is shortly presented thus catering to the first research objective. Extended design considerations and a more detailed overview of the setup is also presented in Appendix B. The method for the fourth research objective is then shortly discussed in section 5-3 where the off-line implementation considerations of the three filters is presented.

The results from implementation can then be presented in Chapter 6 whereafter the discussion, conclusions and recommendations are presented in Chapter 7 and Chapter 8.

Chapter 2

Evaluation of recursive Bayesian filters for modal contribution estimation in high-tech compliant mechanisms.

Evaluation of recursive Bayesian filters for modal contribution estimation in high-tech compliant mechanisms.

P. E. de Bruin * **M. B. Kaczmarek** ** **M. Kok** *** **H. HosseinNia** ****

* *Delft University of Technology, Delft, 2628 CD The Netherlands (e-mail: P.E.deBruin@student.tudelft.nl).*
** *Delft University of Technology, Delft, 2628 CD The Netherlands (e-mail: M.B.Kaczmarek@tudelft.nl).*
*** *Delft University of Technology, Delft, 2628 CD The Netherlands (e-mail: M.Kok-1@tudelft.nl).*
**** *Delft University of Technology, Delft, 2628 CD The Netherlands (e-mail: s.h.hosseinniakani@tudelft.nl).*

Abstract: In this work, three Recursive Bayesian input and state estimation algorithms previously introduced in civil engineering are evaluated for use on on high-tech compliant mechanisms to estimate modal contributions for use in Active Vibration Control, since this allows for significantly different sensor configurations. The three algorithms, namely, the Augmented Kalman Filter (AKF), Dual Kalman Filter (DKF) and Gilijns de Moor Filter (GDF) are implemented in simulation and on an experimental compliant motion stage setup. Their performance is evaulated on system acceleration dependency and overall fit quality resulting in the GDF performing overall best.

Keywords: AVC, IMSC, state estimation, motion stages, compliant mechanisms

1. INTRODUCTION

Recent advances towards high-throughput high-precision in the high-tech industry has led to increasing interest in compliant motion systems. When operating these systems in an high-acceleration environment however, higher frequency vibrational modes can reduce overall accuracy and thus throughput. One possible solution for this is an active attempt to add damping to the system often referred to Active Vibration Control (AVC).

More traditional methods of AVC require collocated measurements, where a sensor and actuator are placed at the same location on the compliant flexure, and are connected through a control algorithm like Positive Position Feedback (PPF) as sketched in Preumont (1999). A more centralised approach is Independent Modal Space Control (IMSC), where every vibrational mode can be dampened independently as introduced by Meirovitch and Oz (1979) and Balas (1978). This class of methods allows for the damping of specific higher order vibrational modes without spending control effort on modes of less interest by decoupling the MIMO AVC control problem for all modes into a SISO problem for every controlled mode separately.

IMSC methods generally require information about the modal contribution of each mode in a compliant system. This information is traditionally obtained by employing a static modal filter (Pusch, 2018; Pusch and Ossmann, 2019) as introduced in Meirovitch and Baruh (1985) and Preumont et al. (2003).

These static filters, however, do not take measurement and process noise into account, limiting performance of the overall AVC system (Meirovitch and Baruh, 1985).

To obtain an estimate about the modal contribution based on noisy measurements, recursive Bayesian filters (RBFs) for state estimation can be implemented instead of static modal filters. These RBFs assume stochastic system modelling, and therefore inherently assume a noise corrupted system. A problem with more traditional RBFs like the original linear Kalman Filter (KF) when implemented on compliant structures is they require information about the input to the system to make a prediction about the state. Often for compliant systems however, the input is not known since it includes not only known control inputs, but also disturbances. While some disturbances can be measured or modelled, most can not.

Similar problems can be found in fields like Structural Health Monitoring (SHM) for civil structures, where state estimates in structures like bridges and buildings are required for strain and lifetime analysis. Here, knowledge about system input is also scarce. As a solution, output-only RBFs were introduced for simultaneous input and state estimation based on acceleration measurements.

Among other approaches, like the Augmented Discrete Extended Kalman Filter (A-DEKF) (Naets et al., 2015a) and proposed Maximum Aposteriori Prediction (MAP) based

⋆ No sponsor or financial acknowledgement required

methods (Sedehi et al., 2019), the Augmented Kalman Filter (AKF) introduced by Lourens et al. (2012b), Dual Kalman Filter introduced by Eftekhar Azam et al. (2015) and Gilijns de Moor Filter introduced by Lourens et al. (2012a) are often evaluated in SHM (Moradi et al., 2021). These three methods, represent state of the art in SHM.

The implementation of these algorithms into high-tech compliant mechanisms instead of civil structures presents a significantly different environment and is worthy of evaluation. Due to this environmental difference, alternative sensor configurations can be used. For these civil structures for instance, strain measurements are hard to obtain, whereas acceleration measurements are cheap and easy. This unavailability of strain measurements can reduce estimate performance significantly as sketched by Naets et al. (2015b); Eftekhar Azam et al. (2015) and Tatsis and Lourens (2017). For high-tech compliant mechanisms, however, these strain measurements are much easier to implement due to small system size and a highly controlled environment. In addition to this, high-tech systems often benefit from in-depth system knowledge allowing for accurate modelling which also benefits RBF implementation.

To the best of the authors' knowledge, the possibilities of implementing RBF solutions from SHM into compliant mechanisms have not been previously studied. This forms a research gap which we attempt to address in this work. For the first time, the RBFs for modal contribution estimation are implemented on a compliant motion stage. The operation of filters is studied both when the system is disturbed by external forces as well as during the tracking of reference signals in closed loop. Since closed loop reference tracking intruces high accelerations into the system, the performance of the RBFs with respect to dependence on the magnitudes of system accelerations is evaluated in addition to their overall fit performance.

The remainder of the paper is organized as follows. To provide a system model, section 2 first introduces the necessary Finite-Element modelling approach, hereby establishing notation and introducing the desired modal contributions. Using this resulting model definition, section 3 introduces the three RBFs taken from the field of SHM being evaluated for implementation in high-tech compliant flexures, herewith concluding the background section. The implementation on an actual compliant motion stage guidance flexure is presented in section 4 whereafter the design of experiments is presented in section 5. The results, discussion and conclusions & recommendations are presented in section 6, section 7 and section 8 respectively.

2. MATHEMATICAL PROBLEM FORMULATION

The implementation of recursive Bayesian filters requires a system model. For compliant flexures, this system model is set up through a Finite-Element (FE) assumption using 1D Euler-Bernoulli beam theory. This section is included to introduce a system model formulation, establish notation and define the desired modal contributions. All methods introduced here are further substantiated and presented in more detail in Cook et al. (2001).

The dynamics equations are presented in subsection 2.1 whereafter the measurement equations are introduced in subsection 2.2. These are then combined into a linear time invariant state space model in subsection 2.3 whereafter a modal decomposition is presented to introduce the desired modal contributions into the state vector.

2.1 Dynamics

When applying a finite-element discretisation to the compliant flexure, the system dynamics can be described by the evolution of the degrees of freedom (DOF) of the element nodes (the system states in nodal space). These system dynamics are captured by a linear second-order continuous time differential equation as derived in Cook et al. (2001) as:

$$M\ddot{\bar{x}} + C'\dot{\bar{x}} + K\bar{x} = B'\bar{f}, \tag{1}$$

where the matrices M, C' and $K \in \mathcal{R}^{2n\times 2n}$ denote the mass, damping and stiffness matrices of the system. With n representing the amount of nodes used for the FE approximation. These matrices can be constructed following standard FE procedures as mentioned in Cook et al. (2001) or any other textbook on the subject. The system state $\bar{x} \in \mathcal{R}^{2n\times 1}$ represents a collection of the nodal degrees-of-freedom (DOFs), with $\dot{\bar{x}}$ and $\ddot{\bar{x}}$ denoting their first and second time derivatives. For the Euler-Bernoulli FE assumption, each node is attributed a lateral displacement and rotational DOF. The location of the external input forces $\bar{f} \in \mathcal{R}^{n_u\times 1}$ is determined by the selection matrix $B' \in \mathcal{R}^{2n\times n_u}$ with n_u the amount of external input forces acting on the system.

2.2 Measurements

For compliant flexures, three measurements that can be used are displacement, acceleration and strain measurements. The configuration that will be used for simulation and implementation will be introduced later on. Here however, only the measurement equations are introduced for a general configuration.

For displacement measurement, the interpolation matrix $S_d \in \mathcal{R}^{n_d\times 2n}$ is introduced as

$$\bar{y}_d = S_d\bar{x}, \tag{2}$$

where S_d merely interpolates the nodal DOFs through a third order shape function $N(y)$ as presented in Cook et al. (2001). The amount of displacement measurements is denoted by n_d.

For an acceleration measurement, (1) is used to obtain an expression for the state acceleration $\ddot{\bar{x}}$, and is again premultiplied by an interpolation matrix $S_a \in \mathcal{R}^{n_a\times 2n}$ as:

$$\bar{y}_a = S_aM^{-1}B'\bar{f} - S_aM^{-1}C'\dot{\bar{x}} - S_aM^{-1}K\bar{x}. \tag{3}$$

Thereby resulting in an expression for the lateral acceleration at any location along the compliant system.

The strain measurement is obtained using a similar approach as mentioned by Preumont (1999) and Aktas and Esen (2020). Here, the strain over one element is extracted by integrating the second spatial derivative of the elemental shape function $N(y)$ over the length of the element L. This is multiplied by the collection of DOFs for that specific element $\bar{d}_i$ and the distance away from the center line of the flexure h resulting in:

$$\epsilon_i = \underbrace{h \int_0^L \frac{d^2}{dy^2} N(y) dy}_{S_{s,i}} \bar{x}_i, \tag{4}$$

where the strain ϵ_i over element i is thus defined by multiplying the elemental matrix $S_{s,i} \in \mathcal{R}^{1\times 4}$ with the 4 nodal DOFs of element i (one element contains 2 nodes, thus 4 DOFs) in $\bar{x}_i$. The system matrix $S_a \in \mathcal{R}^{n_s \times 2n}$ is then constructed by applying this elemental selection matrix for every element the strain is measured over, resulting in the strain measurement as:

$$\bar{y}_s = S_s \bar{x}, \tag{5}$$

where n_s represents the amount of strain measurements, and $\bar{y}_s$ the actual measurements.

2.3 System construction

To combine the dynamics equation in (1), and measurement equations in (2), (3) and (5) into a full linear Time Invariant (LTI) continuous time state space system, the second order linear continuous time differential equation introduced in (1) is first decoupled. This is done by defining the nodal state vector $\bar{d} = \begin{bmatrix} \bar{x} \\ \dot{\bar{x}} \end{bmatrix}$ resulting in the system dynamics and measurement equations in nodal space as:

$$\dot{\bar{d}} = \underbrace{\begin{bmatrix} 0 & I \\ -M^{-1}K & -M^{-1}C' \end{bmatrix}}_{A_{c,n}} \bar{d} + \underbrace{\begin{bmatrix} 0 \\ M^{-1}B' \end{bmatrix}}_{B_{c,n}} \bar{f} \tag{6}$$

$$\bar{y} = \underbrace{\begin{bmatrix} S_d & 0 \\ -S_a M^{-1}K & -S_a M^{-1}C' \\ S_s & 0 \end{bmatrix}}_{C_{c,n}} \bar{d} + \underbrace{\begin{bmatrix} 0 \\ S_a M^{-1}B' \\ 0 \end{bmatrix}}_{D_{c,n}} \bar{f}, \tag{7}$$

with $A_{c,n} \in \mathcal{R}^{4n\times 4n}$, $B_{c,n} \in \mathcal{R}^{4n\times n_u}$, $C_{c,n} \in \mathcal{R}^{(n_d+n_a+n_s)\times 4n}$ and $D_{c,n} \in \mathcal{R}^{(n_d+n_a+n_s)\times n_u}$ representing the continuous time (denoted by $_c$) state space matrices in nodal domain (denoted by $_n$). The measurement equation in (7) now contains displacement, acceleration and strain measurements by combining (2), (3) and (5).

As can be seen, the system scales proportional to four times the amount of nodes used for FE approximation, $4n$, therefore scaling $A_{c,n}$ and $C_{c,n}$ and the state $\bar{d}$. To reduce system order, and introduce the desired modal contribution η in the state vector, the system is modally decomposed by solving the un-damped eigenvalue problem:

$$(K - \omega^2 M)\bar{v} = 0, \tag{8}$$

hereby obtaining the eigenvector matrix $\Phi \in \mathcal{R}^{2n\times N}$ with N the amount of modelled eigenmodes $\bar{v}$. The corresponding system eigenfrequencies ω are captured in the matrix $\Omega = \text{diag}\,[\omega_1 \dots \omega_N]$. Assuming the system is spanned by its eigenvectors, the state transformation is defined as:

$$\bar{x} = \Phi \bar{z}, \tag{9}$$

with $\bar{z}$ containing the modal contributions η as $\bar{z} = [\eta_1 \dots \eta_N]^T$. Applying this state transformation to (6) and (7) and mass normalising Φ such that $\Phi^T M \Phi = \mathcal{I}$ and $\Phi^T K \Phi = \Omega^2$, the full state space system can be reformulated in modal space as:

$$\dot{\bar{q}} = \underbrace{\begin{bmatrix} 0 & I \\ -\Omega^2 & -\Phi^T C' \Phi \end{bmatrix}}_{A_{c,m}} \bar{q} + \underbrace{\begin{bmatrix} 0 \\ \Phi^T B' \end{bmatrix}}_{B_{c,m}} \bar{f} \tag{10}$$

$$\bar{y} = \underbrace{\begin{bmatrix} S_d\Phi & 0 \\ -S_a\Phi\Omega^2 & -S_a \\ S_s\Phi & 0 \end{bmatrix}}_{C_{c,n}} \bar{q} + \underbrace{\begin{bmatrix} 0 \\ S_a\Phi\Phi^T B' \\ 0 \end{bmatrix}}_{D_{c,n}} \bar{f}, \tag{11}$$

where the new modal state vector is defined as $\bar{q} = \begin{bmatrix} \bar{z} \\ \dot{\bar{z}} \end{bmatrix}$ now containing the desired modal contributions and velocities. The modal system in (10) and (11) thus follows from pre-multiplying (6) and (7) by Φ, and applying the state transformation defined in (9). This results in an LTI state space system scaling with the amount of modelled modes N instead of the amount of nodes n, allowing for arbitrarily meshed FE models, and containing the desired modal contributions η in its state vector.

The objective of the RBFs considered in this paper is to obtain an estimate of these modal contributions η. For this, the LTI state space model introduced in (10) and (11) is discretised to obtain a discrete model with the modal contributions represented in the state vector. This is done by making a Zeroth Order Hold (ZOH) assumption by assuming a constant behaviour in between samples. The resulting discrete time linear state space system is summarised as:

$$\bar{q}_{k+1} = A\bar{q}_k + B\bar{f} + \bar{w}_k \tag{12}$$

$$\bar{y}_k = C\bar{q}_k + D\bar{f} + \bar{v}_k \tag{13}$$

where in addition, the discrete noise sequences $\bar{w}$ and $\bar{v}$ are added to represent process and measurement noise respectively. The noise is assumed Gaussian with zero mean and covariance matrices Q and R respectively.

3. RECURSIVE BAYESIAN SIMULTANEOUS INPUT AND STATE ESTIMATION

As mentioned in section 1, three RBF solutions for simultaneous input and state estimation are evaluated in this work, namely:

- Augmented Kalman Filter (AKF)
- Dual Kalman Filter (DKF)
- Gilijns de Moor Filter (GDF)

In this section, the main model formulation and filter equations are presented for these three approaches as well as some background. It is important to note all filters essentially assume the system matrices presented in (12) and (13). The model formulation however differs for every filter based on the assumptions made.

3.1 Augmented Kalman Filter (AKF)

Even though the Augmented Kalman Filter (AKF) formulation has existed for a while as shown by Verhaegen and Verdult (2007), its introduction into structural mechanics was done by Lourens et al. (2012b) where it was implemented for estimation of external forces on submerged wind turbine foundations. Its formulation only requires an augmented system model, whereafter the regular linear Kalman filtering framework as introduced in Kalman

(1960) can be used. For this augmented system model, the input $\bar{f}$ is assumed to vary along a random walk process as

$$\bar{f}_{k+1} = \bar{f}_k + \bar{z}_k, \tag{14}$$

where the fictional noise sequence $\bar{z}_k$ allows for variation in the derivative of the input, and is assumed Gaussian distributed with zero mean and covariance matrix Q_f. Assuming these dynamics for the system input, the state vector $\bar{q}$ can be augmented by defining the augmented state vector as $\bar{q}^a = \begin{bmatrix} \bar{q} \\ \bar{f} \end{bmatrix}$. This allows for the re-formulation of the system dynamics introduced in (12) and (13) to:

$$\bar{q}^a_{k+1} = \underbrace{\begin{bmatrix} A & B \\ 0 & I \end{bmatrix}}_{A^a} \bar{q}^a_k + \underbrace{\begin{bmatrix} \bar{w}_k \\ \bar{z}_k \end{bmatrix}}_{\bar{\zeta}_k} \tag{15}$$

$$\bar{y} = \underbrace{[C \;\; D]}_{C^a} \bar{q}^a_k + \bar{v}_k, \tag{16}$$

thus introducing an autonomous system formulation. In addition to this, the state covariance matrix Q is augmented with the fictional noise covariance matrix Q_f as

$$Q_\zeta = \begin{bmatrix} Q & 0 \\ 0 & Q_f \end{bmatrix}.$$

For the actual filter equations, the standard Kalman filtering equations also introduced by Kalman (1960) are applied using the autonomous model defined in (15) and (16). These AKF equations are recalled as:

Time update:

$\hat{\bar{q}}^a_{k|k-1} = A^a \hat{\bar{q}}^a_{k-1|k-1}$

$P_{k|k-1} = A^a P_{k-1|k-1} A^{aT} + Q_\zeta$

Measurement update:

$K_k = P_{k|k-1} C^{aT} (C^a P_{k|k-1} C^{aT} + R)^{-1}$

$\hat{\bar{q}}^a_{k|k} = \hat{\bar{q}}^a_{k|k-1} + K_k (y_k - C^a \hat{\bar{q}}^a_{k|k-1})$

$P_{k|k} = P_{k|k-1} - K_k C^a P_{k|k-1}$

---

with the state covariance matrix P defined as

$$P = E\left[(\bar{q}^a - \hat{\bar{q}}^a)(\bar{q}^a - \hat{\bar{q}}^a)^T\right].$$

In addition to the tuning of the Q and R matrices, this augmented filter formulation also requires the tuning of the input variation covariance matrix Q_f. This can limit real-world application since information about the variation $\bar{z}$ is often not available (Lourens et al., 2012b). This, however, is fundamental to the assumption of a random walk process for the input as presented in (14).

3.2 Dual Kalman Filter (DKF)

A second approach to the simultaneous input and state estimation problem is presented by Eftekhar Azam et al. (2015) as a remedy to instability of the AKF for acceleration-only measurements. Here, instead of incorporating the input into the state of a new augmented system formulation as done in the AKF, an additional Kalman filtering stage is introduced to obtain an estimate for the input. This stage precedes the second Kalman filtering stage which uses the estimated input to estimate the current state.

To formulate the first Kalman filtering stage for input estimation, again, the same random walk process equation for input dynamics is assumed as presented in (14). To complete a system model for the input dynamics however, the measurement equation presented in (13) is assumed. Here the system input force $\bar{f}_k$ now takes up the role of system state, and $\bar{q}_k$ the external input already estimated by the previous time step. This thus results in a re-formulated state-space system for the input dynamics as:

$$\bar{f}_{k+1} = \bar{f}_k + \bar{z}_k \tag{17}$$

$$\bar{y}_k = D\bar{f}_k + C\hat{\bar{q}}_k + \bar{v}_k, \tag{18}$$

where $\bar{z}_k$ is again assumed Gaussian distributed with covariance matrix Q_f. The first (input) Kalman filtering stage is obtained by evaluating the Kalman filter equations for this system model definition, assuming the previously estimated state as input estimate.

The second (state) Kalman filtering stage is then set up by evaluating the standard Kalman filtering equations again for the system introduced in (12) and (13) using the previously estimated input $\hat{\bar{f}}_{k|k}$.

The resulting DKF filtering equations are recalled here as:

Input time update:

$\hat{\bar{f}}_{k|k-1} = \hat{\bar{f}}_{k-1|k-1}$

$P^f_{k|k-1} = P^f_{k-1|k-1} + Q_f$

Input measurement update:

$K^f_k = P^f_{k|k-1} D^T (D P^f_{k|k-1} D^T + R)^{-1}$

$\hat{\bar{f}}_{k|k} = \hat{\bar{f}}_{k|k-1} + K^f_k (\bar{y}_k - C\hat{\bar{q}}_{k-1|k-1} - D\hat{\bar{f}}_{k|k-1})$

$P^f_{k|k} = P^f_{k|k-1} - K^f_k D P^f_{k|k-1}$

State time update:

$\hat{\bar{q}}_{k|k-1} = A\hat{\bar{q}}_{k-1|k-1} + B\hat{\bar{f}}_{k|k}$

$P^q_{k|k-1} = A P^q_{k|k-1} A^T + Q$

State measurement update

$K_k = P^q_{k|k-1} C^T (C P^q_{k|k-1} C^T + R)^{-1}$

$\hat{\bar{q}}_{k|k} = \hat{\bar{q}}_{k|k-1} + K_k (\bar{y}_k - C\hat{\bar{q}}_{k|k-1} - D\hat{\bar{f}}_{k|k})$

$P^q_{k|k} = P^q_{k|k-1} - K_k C P^q_{k|k-1},$

---

where the covariance matrices for the state $\bar{q}$ and the input $\bar{f}$ are defined as:

$$P^q = E\left[(\bar{q} - \hat{\bar{q}})(\bar{q} - \hat{\bar{q}})^T\right]$$

$$P^f = E\left[(\bar{f} - \hat{\bar{f}})(\bar{f} - \hat{\bar{f}})^T\right].$$

Even though this DKF employs a fundamentally different approach from the AKF by separating the problem into two separate Kalman filtering stages, it still requires

information about the input variation sequence $\bar{z}$ in the form of the covariance matrix Q_f, again inherent to the random walk input process equation assumed in (17). Similar to the AKF, this limits real-world tuning capability according to Tatsis and Lourens (2017).

3.3 Gilijns de Moor Filter (GDF)

This third approach was first introduced by Kitanidis (1987) whereafter it was augmented in Gillijns and De Moor (2007a) and Gillijns and De Moor (2007b) with a new minimum variance unbiased formulation for systems with direct feedthrough. It is first introduced into structural mechanics in Lourens et al. (2012a) where additional work on this formulation has been done to incorporate the case where more sensors than modal states are used. This however is outside the scope of this work.

For the original filter formulation as proposed in Gillijns and De Moor (2007b), a similar two-stage estimation structure is set up as in the DKF. Instead of a Kalman filter estimate for the input however, a recursive Weighted Least-Squares estimation is used. For this, no assumption on the input dynamics is required thus eliminating the need for the additional tuning of an input covariance matrix.

The resulting GDF filtering equations are recalled here as:

Time update:

$$\hat{\bar{q}}_{k|k-1} = A\hat{\bar{q}}_{k-1|k-1} + B\hat{\bar{f}}_{k-1}$$

$$P^q_{k|k-1} = [A\ B]\begin{bmatrix} P^q_{k-1|k-1} & P^{qf}_{k-1} \\ P^{fq}_{k-1} & P^f_{k-1} \end{bmatrix}\begin{bmatrix} A^T \\ B^T \end{bmatrix} + Q$$

Input estimate:

$$\tilde{R}_k = CP^q_{k|k-1}C^T + R$$

$$M_k = (D^T\tilde{R}_k^{-1}D)^{-1}D^T\tilde{R}_k^{-1}$$

$$\hat{f}_k = M_k(\bar{y}_k - C\hat{\bar{q}}_{k|k-1})$$

$$P^f_k = (D^T\tilde{R}_k^{-1}D)^{-1}$$

Measurement update:

$$K_k = P^q_{k|k-1}C^T\tilde{R}_k^{-1}$$

$$\hat{\bar{q}}_{k|k} = \hat{\bar{q}}_{k|k-1} + K_k(\bar{y}_k - C\hat{\bar{q}}_{k|k-1} - D\hat{\bar{f}}_k)$$

$$P^q_{k|k} = P^q_{k|k-1} - K_k(\tilde{R}_k - DP^f_kD^T)K_k^T$$

$$P^{qf}_k = (P^{fq}_k)^T = -K_kDP^f_k$$

Where the state covariance matrix P^q again defined as:

$$P^q = E\left[(\bar{q} - \hat{\bar{q}})(\bar{q} - \hat{\bar{q}})^T\right]. \tag{19}$$

Note that the time and measurement update of the state estimate resemble the Kalman filter, except that the true value of the input is replaced by an optimal estimate $\hat{\bar{f}}_k$. Also, note that in case $D_k = 0$ and $B_k = 0$, the actual Kalman filter is obtained. Minimum variance and unbiasedness of the input estimate are proven in Gillijns and De Moor (2007a).

4. METHOD

To be able to evaluate performance of the three RBFs introduced in section 3 on the estimation of modal contribution of high-tech compliant mechanisms, they are implemented on a compliant motion stage flexure in simulation and physical experimental setup.

This section elaborates on the design of the experimental setup and system definition in subsection 4.1 whereafter the modelling approach is substantiated and validated against the actual system in subsection 4.2. The filter initialisation and implementation is presented in subsection 4.3. The simulation environment and motivation is also introduced in subsection 4.4.

4.1 Experimental setup

The setup used for filter evaluation is a compliant motion stage flexure. The mechanical setup is presented in Figure 1 where in addition, the measurement and sensing equipment is also introduced. For reference, general

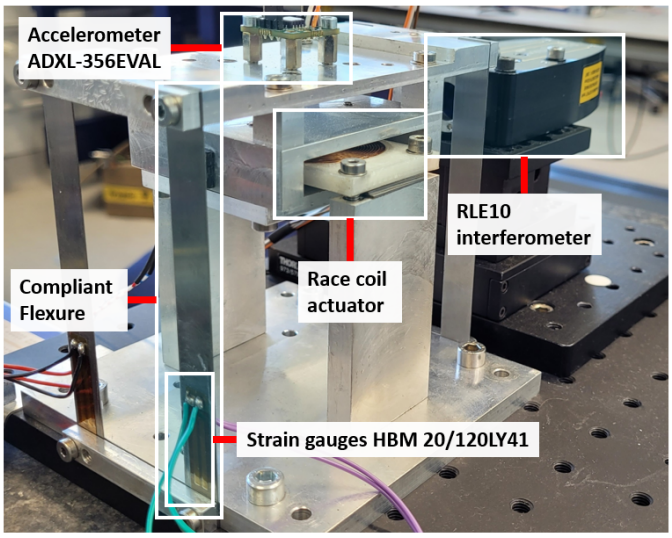

Fig. 1. Compliant motion stage setup actuated by a race coil and implemented acceleration, strain and position measurements.

mechanical properties of the stage flexures are presented in Table 1. On this setup, a strain measurement (HBM

Table 1. Dimension and material of compliant guiding flexures

Material	AISI 1095 Spring Steel
Length	100 mm
Width	12.7 mm
Height	0.4 mm

20/120/LY41) at the base of the flexure, an acceleration measurement at the tip (ADXL-356EVAL) and a position measurement (RLE10) of the stage are implemented. It is assumed the stage is rigidly connected to the flexure tip, and dynamics of the stage itself is neglected. The stage is actuated by a current controlled race-coil providing closed loop position control using the position measurement.

The strain measurements are implemented in full Wheatstone bridge configuration conditioned by a SCAIME CPJ

module. The two actual measurement strain gauges are placed at the second mode strain maximum at the base of the flexure in order to increase observability of the second mode and thus its contribution. The two dummy gauges are mounted to a separate piece of flexure material.

Data is acquisitioned by a TI f28379d Launchpad, also implementing closed-loop position control when required. This board allows for a sampling frequency of $10Khz$.

4.2 Modelling

To obtain an actual model of the system, the FE modelling approach introduced in section 2 is used. To be able to apply this approach, all displacements are assumed small in order to neglect geometrical non-linearity and apply linear Euler-Bernoulli beam theory. In addition, the stage body is assumed rigid. This allows for the assumption that the tip of the flexure is fixed in rotation, and only one interaction force f exists in the lateral direction on this tip, containing all interaction between the stage and the flexure. The boundary of the modelled system can thus be drawn around the flexure without having to take the stage itself into account. This also allows for the application of the methods in this work to become invariant to stage loading, or unknown disturbances on the stage itself since this is all captured in the estimated interaction force f.

Lastly, the stage is assumed fully symmetrical, allowing for the modelling of only one flexure at a time. A graphical representation of this single flexure model using 12 1D Euler-Bernoulli finite elements is presented in Figure 2 for the first and second mode shape. Here, the location of the strain measurement at the base (red elements), acceleration measurement at the tip (green cross) and interaction force f is also presented.

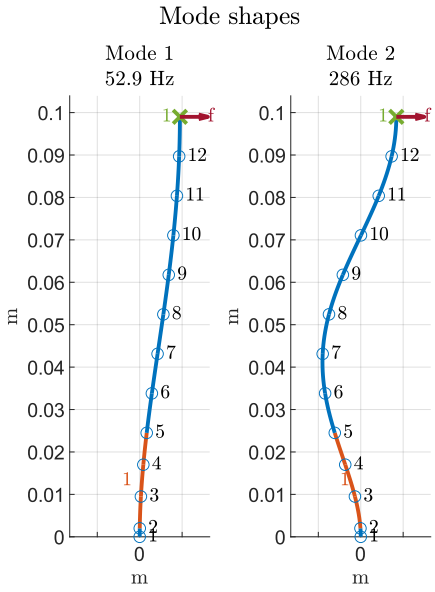

Fig. 2. FE model system boundary definition and mode shape visualisation with the strain measurement (red elements), acceleration measurement (green cross) and interaction force f locations.

As can be seen, the modal frequency of the second mode is located at 286Hz. Since additional higher order vibrational modes will have higher natural frequencies above available measurement capabilities, the full system is truncated to the first two modes using the modal decomposition as introduced in subsection 2.3. Thus resulting in a state vector $\bar{q} \in \mathcal{R}^{4\times1}$ containing the modal contributions η and modal velcoities $\dot{\eta}$ in (10).

Since it is not possible to obtain the free system as modelled due to the inability to apply the input force (interaction force f), the model is slightly altered for validation. Here, a mass representing roughly 1/4 the stage body mass is added to the tip of the flexure, thus shifting the input force from the flexure-stage interaction force, to the race coil actuation force. This system is identified using multiple sine sweeps over the expected first and second mode locations. The resulting identification from the race coil input force to the measured position output is presented in Figure 3.

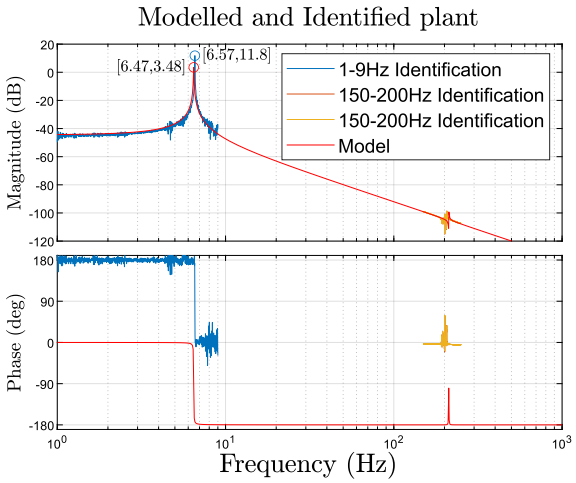

Fig. 3. Modelled (red) and identified (blue, yellow and orange) plant dynamics. Bode plot from input force to flexure tip position.

Here, the modelled stage mass is adjusted to obtain accordance between the system model and identified plant modal peak locations. In addition, the modal damping of the model is also tuned since this is not directly obtained from material properties. As can be seen, the location and amplitude of the first modelled mode coincides well with identified dynamics. The two independent identification sequences for the second mode however show some additional dynamics compared to the modelled response. It is assumed this is due to additional modes occurring from flexure interaction, since the true system does not consist of merely 1 flexure but 4. The interaction between these flexures can introduce degenerate modes close to the resonance frequency of the individual mode.

Since the first mode is correct, and the location of the second mode is close to the measured dynamics, the model is assumed sufficiently accurate for use in the RBF implementations.

It is important to note that for the RBF implementation, only the strain and acceleration measurements are used

for estimation. The position measurement as represented by the first block row in (11) is used only for validation of the model and validation of estimation performance.

4.3 Filter Implementation

For the RBF implementation, all states and covariance matrices require initialisation in addition to the filter parameters requiring tuning.

For initialisation, the true system states $\bar{q}$ are assumed unknown due to possible remnant vibrations or internal stresses. The filter states $\bar{q}_{k=0}$ for all three filters are thus initialised at 0. No information is available about the variance of this estimate, which is thus assumed relatively large by initialising all state covariance matrices P_0 at $10^3 \cdot \mathcal{I}$. These initialisation parameters are used for all states and state covariance matrices for all three filters.

For filter tuning, the AKF and DKF require the tuning of the process noise, measurement noise and input variance covariance matrices Q, R and Q_f respectively. The GDF again does not assume a random walk process equation for the input, and only requires tuning of the Q and R matrices.

To reduce tuning parameter space, the Q and R matrices are assumed diagonal as $Q = q_{\text{tune}}\mathcal{I}$ and $R = r_{\text{tune}}R_0$ with scalar tuning parameters q_{tune} and r_{tune} similar to Petersen et al. (2019). Since only one input force is assumed, Q_f already computes to a scalar therefore reducing the tuning parameter space to three dimensions. The initial measurement covariance matrix R_0 is constructed using measured noise covariance values as:

$$R_{\text{init}} = \begin{bmatrix} \text{cov}_{\text{acc}} & 0 \\ 0 & \text{cov}_{\text{strain}} \end{bmatrix}, \tag{20}$$

with $\text{cov}_{\text{acc}} = 0.0587\text{m}^2/\text{s}^2$ and $\text{cov}_{\text{strain}} = 1.095 \cdot 10^{-16}\text{m}^2/\text{m}^2$. This ensures relative covariance between the sensors is maintained when only tuning r_{tune}.

The first two parameters, q_{tune} & r_{tune}, are tuned using a non-linear Nelder-Mead simplex algorithm for all three filters after an initial empirical tuning step is made. Here, the cost function is set up as a minimisation of the Normalised Root-Mean-Squared Error (NRMSE) fit score of the estimated tip position versus the measured tip position for an independent 20s long training data set. This thus 'trains' the filters by adjusting the tuning parameters to obtain a better NRMSE fit score of the tip position. It is important to note no global optimality is guaranteed, as this is sensitive to local minima. Grid searches are however used to attempt finding the best local minimum.

After convergence of the NRMSE fit score used as objective function, the AKF and DKF still require tuning for Q_f, which is done using an L-curve regularisation similar to Tatsis and Lourens (2017). This L-curve plots the NRMSE again between the estimated and measured tip position for a training data set versus the regularisation parameter Q_f as can be seen in Figure 4.

As can be seen, no real improvement in the fit performance of the filters is observed after the steep decline in error. The input variance is thus chosen shortly after this decline. It is noteworthy that this regularisation is only possible due to the availability of a validation position measurement. In many real systems however, this validation and thus this tuning approach is not available.

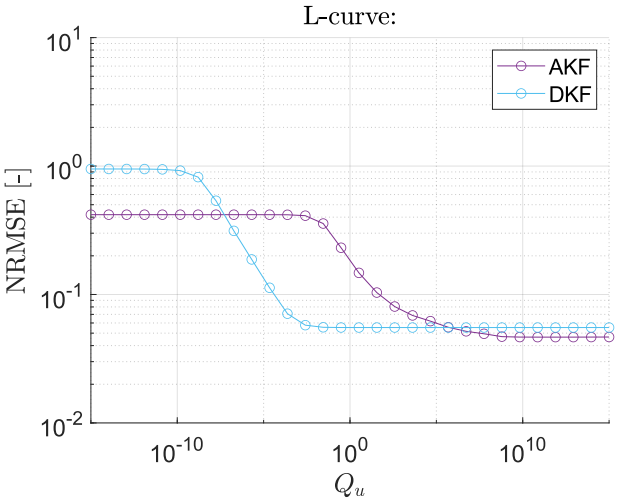

Fig. 4. NRMSE versus Q_f plot for the AKF and DKF for L-curve regularisation.

Since the L-curve depends on the values chosen for q_{tune} and r_{tune}, the process of optimisation followed by L-curve regularisation is iterated until parameters converge. These final filter parameters are presented in Table 2.

	AKF	DKF	GDF
q_{tune}	$1.86{\cdot}10^{-9}$	$3.03{\cdot}10^{-13}$	$2.24{\cdot}10^{-5}$
r_{tune}	$2.26{\cdot}10^{4}$	$1.11{\cdot}10^{4}$	$2.29{\cdot}10^{14}$
Q_f	$1{\cdot}10^{10}$	$1 \cdot 10^{1}$	-

Table 2. Tuned filter parameters

The filters that are implemented on the actual setup and simulations both use this set of parameters.

4.4 Simulations

Since the only available validation signal in the experimental setup is the measured tip position, the performance of the RBFs with respect to the reconstruction of the modal contributions can not be verified properly since the true values for these are not measured. To remedy this, simulations are first used to show a relation between the tip position estimate and state reconstruction performance. This relation is later used to draw conclusions about the filter's modal contribution reconstruction performance based on its tip location fit performance.

For the simulated system, an erroneous model is used which has a 5% flexure density error and a 1 mm accelerometer and strain gauge positioning error added. The measurements are also augmented with Gaussian distributed noise signals with similar covariance as the experimental setup. To simulate unknown initial system states, the filters are initialised with a relatively large state of $\bar{q} = 10^{-3}$. This is only done in simulation.

For the simulated sequence, an impulse input force f is applied to the tip of the flexure at 0.5s. Hereafter the flexure is allowed to dampen out to be able to evaluate the system's impulse response.

The filters that are used for this simulation do have the same parameters summarised in Table 2 as the filters for the experimental setup to allow comparison.

5. DESIGN OF EXPERIMENTS

To be able to draw relevant conclusions about the evaluation of these filters on high-tech compliant motion stages, their performance is evaluated on two performance metrics:

- system acceleration dependency
- overall fit performance

Since high-tech compliant systems experience high accelerations and velocities, the filter's acceleration dependence is a significant performance metric for this specific application. Overall fit score provides a metric to evaluate and compare the filter's overall performance.

For the experiments on the actual setup, four independent data sets are gathered to evaluate the two performance metrics as mentioned above.

The first two data sets aim at evaluating different acceleration regimes of the stage, where the stage is initiated in open loop before a reference position is tracked in closed loop PID control. The first data set employs a square wave as reference alternating between $\pm 2 \cdot 10^{-}4$ m, whereas the second data set requires the tracking of a 10Hz sinusoidal reference of the same amplitude. The system is allowed to dampen out after the closed loop section resulting in 3 distinct acceleration regions per data set (initialisation, closed loop and remnant oscillation). For these in total 6 regions, the mean absolute acceleration of the stage is computed per section and used for evaluating the filter's response under 6 different acceleration regimes.

To evaluate overall fit performance, two additional data sets are used. Here, an impulse force is provided, whereafter the stage is allowed to dampen out. These two data sets are used in addition to the first two to evaluate the filters on different types of inputs together with the first two.

6. RESULTS

To show validity of the filters used, and establish a relation between filter state reconstruction and tip estimation, the simulation results are first presented in subsection 6.1. Hereafter, results for the implementation on the experimental setup with respect to the two performance metrics are presented in subsection 6.2.

6.1 Simulations

For the simulations, Figure 5 presents the NRMSE fit scores of the three RBFs on three simulated signals namely, the tip location, first mode contribution η_1 and the second mode contribution η_2. To also allow for empirical understanding of the filter performance, Figure 6 presents a small section of the simulated response.

As can be seen in Figure 5 and Figure 6, all three filters are able to reconstruct the flexure tip position. The DKF undershoots consistently for both the tip position and the

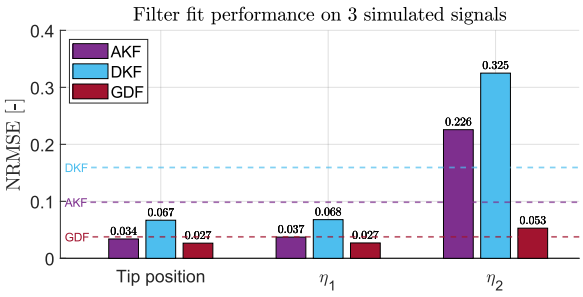

Fig. 5. Simulation fit scores on 3 simulated signals where the dashed lines show the average filter performance over all three signals.

first modal contribution η_1. The AKF and GDF show similar performance where the GDF transmits less noise into the estimate (as can be seen in the actual estimated signals in Figure 6).

It is shown here that the tip position estimate is proportional to the first and second modal contribution estimation performance since the order of estimation quality remains similar. At least for relative comparison, the tip position performance can thus be used as performance metric for modal contribution reconstruction.

6.2 Experiments

The results for the experimental setup are sub-divided into a system acceleration performance evaluation and overall fit performance.

For the acceleration performance evaluation, the mean absolute error between the estimated and measured tip location is computed for every section of the first two data sets (6 sections in total). These values are plotted in Figure 7 on the left y-axis. To evaluate noise transmission into the estimated tip location, the error bar shows one standard deviation off of the average absolute filter error for every section. The second y-axis presents the mean absolute acceleration measurement per section.

As can be seen, the three filters perform significantly different based on the measured acceleration in the system. To show a possible correlation, the mean absolute filter error for all 6 data set sections is plotted against the mean absolute measured acceleration in Figure 8. The the Pearson correlation coefficient is computed as well as a least squares linear fit to show the possible different correlation.

As can be seen, a relatively large correlation coefficient for the DKF in conjunction with the steep gradient of the least squares fit suggests the DKF performs poorly on high acceleration signals. The AKF and GDF perform very comparably, where again the GDF transmits less noise than the AKF as can be seen by the lower standard deviation in Figure 7.

For overall fit performance, the NRMSE fit between the estimated and measured tip position for all four data sets is presented in Figure 9.

Here, it can again be seen the AKF and GDF perform similarly, where the DKF builds up considerably more error. The GDF out performs the AKF slightly overall.

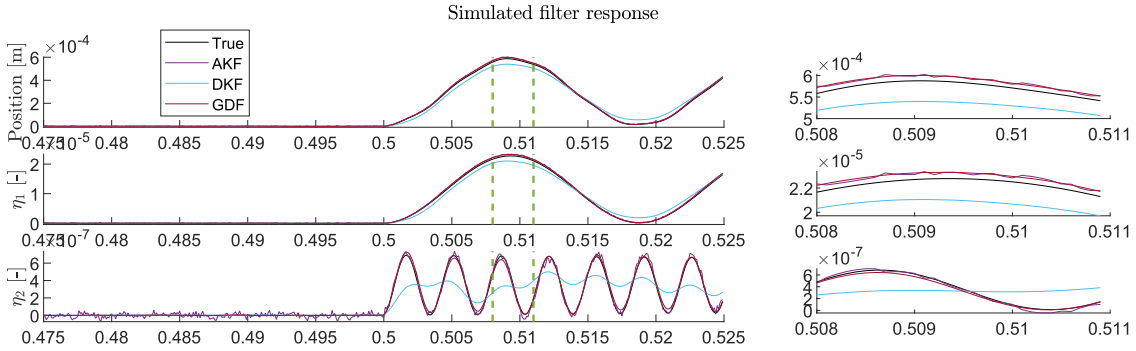

Fig. 6. Simulated system results for the flexure tip position and first and second modal amplitude η_1 and η_2. The green-dashed section is magnified in the right column

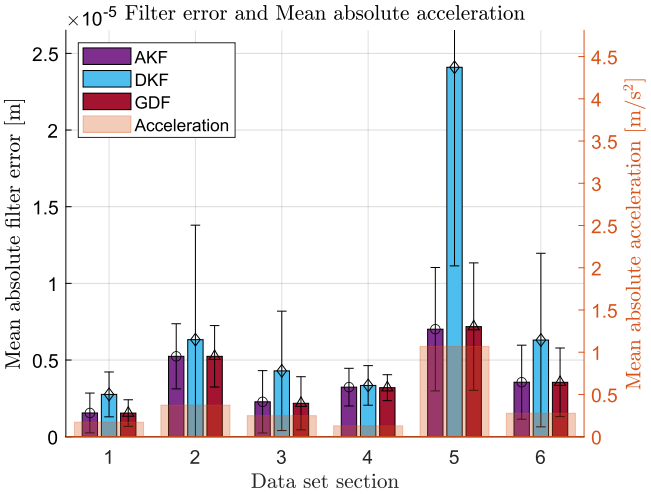

Fig. 7. Mean absolute filter tip position estimation error for all 6 data set sections with an error-bar of one standard deviation. A second y-axis presents the mean absolute acceleration measured.

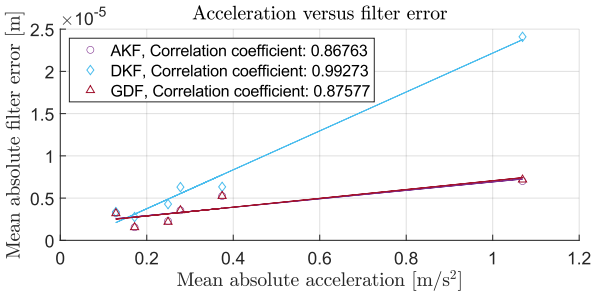

Fig. 8. Mean absolute filter error versus Mean absolute acceleration for all 6 data set sections. The AKF and GDF closely overlap.

7. DISCUSSION

The results presented in the previous section sketch a clear view on the RBFs performance. There are however significant remarks to be made about the implementation and validation process used.

The first significant remark is filter tuning. This process severely impacts the performance of these algorithms, and can therefore influence the comparison between different

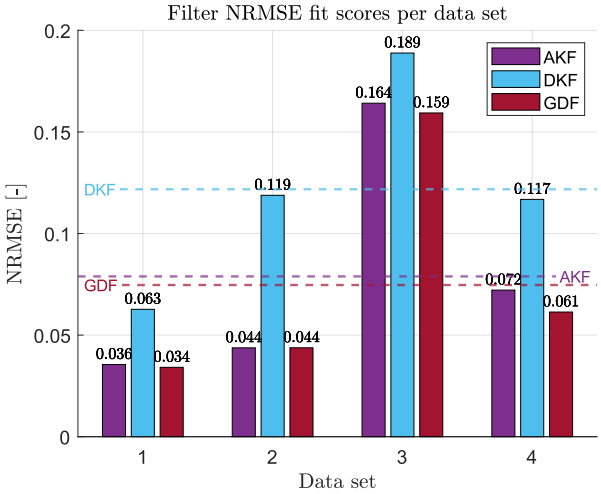

Fig. 9. Overall NRMSE fit performance between the estimated and measured tip position. The dashed line representing the mean filter performance on all data sets.

filters as they can be tuned sub-optimally. In this work, an attempt is made to remedy this by tuning all filters using the same optimisation algorithm and training data set.

The second significant remark to note is the validation process used for these filters. As they are all validated based on the flexure tip position, no hard conclusions can be drawn about the modal amplitude estimation performance as the true value for these signals is not known. In this work however, this is addressed through establishing a link between tip estimation performance and state estimation in simulation.

The third and final remark is the limited amount of data used for filter acceleration dependence. To address this problem, a variety of scenarios representing realistic working conditions of a compliant motion system were included in the data sets used in this work. More operating points could however strengthen this analysis.

It is noteworthy however, that these remarks limit but do not invalidate conclusions made about the results.

8. CONCLUSIONS & RECOMMENDATIONS

This work evaluates Recursive Bayesian Filtering solutions initially introduced for applications in SHM in civil engineering, for estimating modal contribution states of high-tech compliant mechanisms. Specifically, three filters are evaluated, in simulation and through an experimental setup, on acceleration dependence and overall fit performance. All considered filters are able to reconstruct modal contributions. Their performance, however, differs.

From the results on acceleration dependence, it can be concluded the DKF performs poorly on high-acceleration systems whereas the AKF and GDF both perform well, with the GDF showing the lowest increase in estimation error with increased acceleration. This is in line with results obtained by Tatsis and Lourens (2017).

On overall fit performance, a similar trend is observed, with the DKF performing relatively poorly by consistently under-estimating the flexure tip location. The AKF and GDF perform very comparably when looking at NRMSE fit score. It is however noted that the AKF transmits more noise into the estimated quantities as can be seen by a larger error band on the mean absolute filter error. The GDF thus performs overall best on filter performance.

Based on the acceleration dependence, and overall fit performance, it can thus be concluded the GDF is the most viable RBF algorithm for implementation on high-tech compliant mechanisms. This conclusion is somewhat weakened by the fact that tuning significantly impacts the performance of these filters, and validation is done by evaluating the estimated tip location versus the measured tip location. For this some recommendations are made.

To strengthen conclusions about these filter's performance for estimating modal contributions, an additional measurement could be used for validation. Since the modal contributions can not directly be measured, this measurement could be chosen as a position measurement halfway up the flexure. Here, the influence of the second mode is much larger, and a good estimate of this position would provide a better idea of the estimation performance of the second modal amplitude.

Alternatively, an operational modal analysis could be done to compare the estimated to the measured dynamics. Thus further evaluating filter performance to strenghten conclusions.

As for extension of this work, the use of the obtained estimated modal contribution in a full IMSC scheme can be evaluated.

In conclusion, the implementation of RBF algorithms already developed for civil engineering into high-tech compliant motion stages to estimate modal contributions is proven possible, and does offer promising prospects for the field of IMSC in AVC.

REFERENCES

Aktas, K.G. and Esen, I. (2020). State-Space Modeling and Active Vibration Control of Smart Flexible Cantilever Beam with the Use of Finite Element Method. *Engineering, Technology & Applied Science Research*, 10(6), 6549–6556. doi:10.48084/etasr.3949.

Balas, M.J. (1978). Feedback Control of Flexible Systems. *IEEE Transactions on Automatic Control*, 23(4), 673–679. doi:10.1109/TAC.1978.1101798.

Cook, R., Malkus, D., Plesha, M., and Witt, R. (2001). *Concepts and Applications of Finite Element Analysis*. Wiley. URL `https://books.google.nl/books?id=b8seAQAAIAAJ`.

Eftekhar Azam, S., Chatzi, E., and Papadimitriou, C. (2015). A dual Kalman filter approach for state estimation via output-only acceleration measurements. *Mechanical Systems and Signal Processing*, 60, 866–886. doi:10.1016/j.ymssp.2015.02.001. URL `http://dx.doi.org/10.1016/j.ymssp.2015.02.001`.

Gillijns, S. and De Moor, B. (2007a). Unbiased minimum-variance input and state estimation for linear discrete-time systems. *Automatica*, 43(1), 111–116. doi:10.1016/j.automatica.2006.08.002.

Gillijns, S. and De Moor, B. (2007b). Unbiased minimum-variance input and state estimation for linear discrete-time systems with direct feedthrough. *Automatica*, 43(5), 934–937. doi:10.1016/j.automatica.2006.11.016.

Kalman, R.E. (1960). A New Approach to Linear Filtering and Prediction Problems 1. Technical report. URL `http://fluidsengineering.asmedigitalcollection.asme.org/`.

Kitanidis, P.K. (1987). Unbiased minimum-variance linear state estimation. *Automatica*, 23(6), 775–778. doi:10.1016/0005-1098(87)90037-9.

Lourens, E., Papadimitriou, C., Gillijns, S., Reynders, E., Roeck, G.D., and Lombaert, G. (2012a). Joint input-response estimation for structural systems based on reduced-order models and vibration data from a limited number of sensors. *Mechanical Systems and Signal Processing*, 29, 310–327. doi:10.1016/j.ymssp.2012.01.011. URL `http://dx.doi.org/10.1016/j.ymssp.2012.01.011`.

Lourens, E., Reynders, E., Roeck, G.D., Degrande, G., and Lombaert, G. (2012b). An augmented Kalman filter for force identification in structural dynamics. *Mechanical Systems and Signal Processing*, 27, 446–460. doi:10.1016/j.ymssp.2011.09.025. URL `http://dx.doi.org/10.1016/j.ymssp.2011.09.025`.

Meirovitch, L. and Baruh, H. (1985). The implementation of modal filters for control of structures. *Journal of Guidance, Control, and Dynamics*, 8(6), 707–716. doi:10.2514/3.20045.

Meirovitch, L. and Oz, H. (1979). COMPUTATIONAL ASPECTS OF THE CONTROL OF LARGE FLEXIBLE STRUCTURES. In *Proceedings of the IEEE Conference on Decision and Control*, volume 1, 220–229. IEEE. doi:10.1109/cdc.1979.270167.

Moradi, S., Eftekhar Azam, S., and Mofid, M. (2021). On Bayesian active vibration control of structures subjected to moving inertial loads. *Engineering Structures*, 239(March), 112313. doi:10.1016/j.engstruct.2021.112313. URL `https://doi.org/10.1016/j.engstruct.2021.112313`.

Naets, F., Croes, J., and Desmet, W. (2015a). An online coupled state/input/parameter estimation approach for structural dynamics. *Computer Methods in Applied Mechanics and Engineering*, 283, 1167–1188. doi:10.

1016/j.cma.2014.08.010. URL http://dx.doi.org/10.1016/j.cma.2014.08.010.

Naets, F., Cuadrado, J., and Desmet, W. (2015b). Stable force identification in structural dynamics using Kalman filtering and dummy-measurements. *Mechanical Systems and Signal Processing*, 50-51, 235–248. doi:10.1016/j.ymssp.2014.05.042. URL http://dx.doi.org/10.1016/j.ymssp.2014.05.042.

Petersen, W., Øiseth, O., and Lourens, E.M. (2019). The use of inverse methods for response estimation of long-span suspension bridges with uncertain wind loading conditions: Practical implementation and results for the Hardanger Bridge. *Journal of Civil Structural Health Monitoring*, 9(1), 21–36. doi:10.1007/s13349-018-0319-y.

Preumont, A. (1999). Vibration Control of Active Structures: An Introduction. doi:10.1023/A:1004398914135. URL https://www.researchgate.net/publication/229058034.

Preumont, A., François, A., De Man, P., and Piefort, V. (2003). Spatial filters in structural control. *Journal of Sound and Vibration*, 265(1), 61–79. doi:10.1016/S0022-460X(02)01440-2.

Pusch, M. (2018). Aeroelastic mode control using H2-optimal blends for inputs and outputs. *AIAA Guidance, Navigation, and Control Conference, 2018*, (210039). doi:10.2514/6.2018-0618.

Pusch, M. and Ossmann, D. (2019). Blending of inputs and outputs for modal velocity feedback. *27th Mediterranean Conference on Control and Automation, MED 2019 - Proceedings*, 530–535. doi:10.1109/MED.2019.8798491.

Sedehi, O., Papadimitriou, C., Teymouri, D., and Katafygiotis, L.S. (2019). Sequential Bayesian estimation of state and input in dynamical systems using output-only measurements. *Mechanical Systems and Signal Processing*, 131, 659–688. doi:10.1016/j.ymssp.2019.06.007. URL https://doi.org/10.1016/j.ymssp.2019.06.007.

Tatsis, K. and Lourens, E. (2017). A comparison of two Kalman-type filters for robust extrapolation of offshore wind turbine support structure response. In *Life-Cycle of Engineering Systems: Emphasis on Sustainable Civil Infrastructure - 5th International Symposium on Life-Cycle Engineering, IALCCE 2016*, 209–216. CRC Press/Balkema. doi:10.1201/9781315375175-25.

Verhaegen, M. and Verdult, V. (2007). *Filtering and System Identification: A Least Squares Approach*. Cambridge University Press. URL https://books.google.nl/books?id=6Ne76uYOlVwC.

Chapter 3

Input and state estimation

As mentioned before, the novelty of this work is the evaluation of input and state estimation RBFs on the compliant guidance flexures for high-tech motion stages. To do so, the methods for input and state estimation need to be introduced and elaborated on first, which is done in this chapter.

All methods used require a reasonably accurate system model. This model is obtained by approximating the compliant flexure using a finite element (FE) assumption which will be presented in section 3-1. Here, in addition to the dynamical system, also the measurement models are presented as these are required to model the sensors used.

Once a model is set up, the actual input and state estimation algorithms are presented in section 3-2. This is done by first introducing the general Kalman Filtering framework. Even though this theory is far from novel, it is necessary to be able to introduce the three input and state estimation algorithms in the subsequent sections and is thus still presented.

3-1 Modelling

To introduce notation, and develop a system model used for RBF implementation, this chapter first sets up the dynamics equation in subsection 3-1-1 whereafter the measurement equation is set up in subsection 3-1-2. Thus resulting in a full linear state space model of a compliant motion stage flexure and almost fulfilling the second research objective as presented in section 1-3.

3-1-1 Dynamics

The objective of the dynamics model is to capture all relevant dynamics such that the system states can be propagated, and a guess can be made about how the system is going to behave. To do so, the system itself and its states need to be introduced first. To define the system to be modelled, three important high-level assumptions are made:

Assumption 1. *The stage is significantly more rigid than the compliant guidance flexures.*

Assumption 2. *The stage assembly is symmetric.*

Assumption 3. *All motion and deformation is significantly small such that geometrical linearity's are negligible.*

Even though these assumptions can feel trivial, they do allow for significant modelling choices.

Through assumption 1 the rotation of the tip of the flexures can be assumed fixed, and the dynamics of the stage itself is assumed negligible. Combining this with assumption 2 allows for the evaluation of only one flexure at a time since the movement of the stage is assumed the same for all flexures. Even more powerful is the fact that the system boundary can then be drawn at the interface between the stage and the compliant guidance flexure. This can be done with the simple boundary conditions that the rotation of the tip of the flexure is fixed, and an interaction force exists between the stage and the flexure. This system is also graphically represented in Figure 3-1 where the base of the flexure is fixed to the world, the top is fixed in rotation to the motion stage body, and an interaction force f is defined between the stage and the flexure in horizontal direction.

To actually model the dynamics of the compliant flexure with its previously defined system boundary, a finite element (FE) analysis is used. The objective of this approach is to approximate a continuous field quantity (like position) by a set of values at discrete locations (nodes). This approach is far from new, and a very active area of research. The interested reader is referred to [19] or any of the many other textbooks in this area for more details. Only the basic concepts are recalled here for completeness and introduction of concepts and notation.

Figure 3-1 presents the described system already discretised into two finite elements. As shortly mentioned before, the dynamics of the compliant flexures is modelled using 1D Euler-Bernoulli beam elements of which the base will eventually be fixed, and the tip will be locked in rotation. Important to note, is the fact that assumption 3 allows for a purely linear system model, since geometrical and material non-linearities can be disregarded.

The discretisation presented in Figure 3-1 requires 2 elements, and 3 nodes. Where each node has a translational and rotational degree of freedom (d and ϕ respectively). It is important to note that the entire continuous displacement field for element i, $d(y_i)$, can be described by relating these discrete DOFs of the nodes to the continuous field using the appropriate shape functions. The shape function for one single element i using a cubic interpolation $N(y_i)$ is taken as [19]:

$$\begin{aligned} d(y_i) &= \underbrace{\begin{bmatrix} 1 & y_i & y_i^2 & y_i^3 \end{bmatrix}}_{X(y)} \underbrace{\begin{bmatrix} 1 & 0 & 0 & 0 \\ 0 & 1 & 0 & 0 \\ 1 & L & L^2 & L^3 \\ 0 & 1 & 2L & 3L^2 \end{bmatrix}^{-1}}_{F^{-1}} \begin{bmatrix} d_i \\ \phi_i \\ d_{i+1} \\ \phi_{i+1} \end{bmatrix} \\ &= \underbrace{X(y_i)F^{-1}}_{N(y_i)} \bar{\Phi}_i, \end{aligned} \tag{3-1}$$

where L represents the element length and y_i the natural coordinate along this element. The field quantity at the nodal locations $\bar{\Phi}_i$ of element i can represent any field quantity (like temperature or charge) if the correct shape function is used. In Eq. 3-1, the field quantities

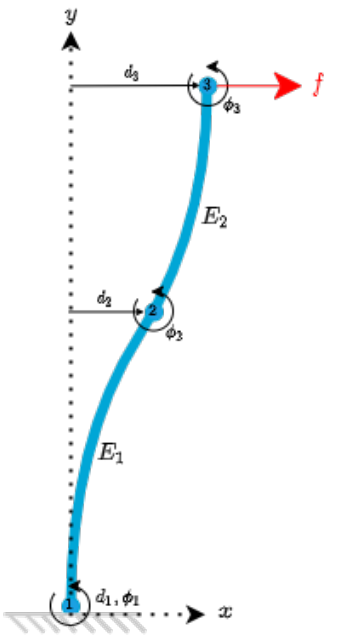

Figure 3-1: Euler-Bernoulli finite element approximation of a compliant guidance flexure using two elements and 3 nodes. Each node containing a rotational degree of freedom (ϕ) and translational degree of freedom (d).

used is the displacement of the beam in horizontal displacement. This shape function thus maps the displacement and rotation at the nodal locations of element i to the horizontal displacement at any location along the element, $d(y_i)$, through the shape function $N(y_i)$. The natural coordinate y_i runs from 0 (at the beginning of the element) to L, at the end of the element.

This can be done for any element, allowing for interpolation of the discrete field quantities $\bar{\Phi}_i$ (at the nodes) to a continuous displacement field $d(y_i)$ (in between the nodes) thus describing the deformation of the beam at any location y_i based on the nodes. Since the shape function only maps the displacement and rotation at the nodal locations of one element to the displacement along this single element, the entire displacement field can be described using a vector containing all shape functions from all elements used. For completeness, this shape function vector is also presented as:

$$\bar{N}(y) = \begin{bmatrix} N(y_1) & N(y_2) & \dots & N(y_n) \end{bmatrix}, \tag{3-2}$$

with the natural coordinate of every respective element $y_1 \dots y_n$.

The evolution of the nodal DOFs and their interconnection are then determined using the equations of motion (EOMs). For the finite element system, the equations of motion are generally presented by the second order differential equation [19]

$$M\ddot{\bar{x}} + C'\dot{\bar{x}} + K\bar{x} = B'f, \tag{3-3}$$

where M, C' and K are the mass, damping and stiffness matrices of the system respectively. The input force f represents the interaction force between the stage and the flexure where B'

selects the location of this force. The state $\bar{x}$ is defined as the collection of nodal DOFs for a discretisation of n nodes as:

$$\bar{x} = \begin{bmatrix} d_1 \\ \phi_1 \\ \vdots \\ d_n \\ \phi_n \end{bmatrix}, \tag{3-4}$$

with $\dot{\bar{x}}$ and $\ddot{\bar{x}}$ denoting its first and second time derivative. This state $\bar{x}$ thus equals the nodal field quantity vector $\bar{\Phi}_i$ as introduced in the previous section, collected for all nodes in the system. For clarity, a displacement at any location could then be extracted through the shape function vector as $d(y) = \bar{N}(y)\bar{x}$.

The elemental Mass and Stiffness matrices for the 1D Euler-Bernoulli elements are then given as [19]:

$$K_i = \int_0^L U^T E U dy = \frac{EI}{L^3} \begin{bmatrix} 12 & 6L & -12 & 6L \\ 6L & 4L^2 & -6L & 2L^2 \\ -12 & -6L & 12 & -6L \\ 6L & 2L^2 & -6L & 4L^2 \end{bmatrix} \tag{3-5}$$

$$M_i = \int_0^L N(y_i)^T N(y_i) \rho A dy = \frac{\rho AL}{420} \begin{bmatrix} 156 & 22L & 54 & -13L \\ 22L & 4L^2 & 13L & -3L^2 \\ 54 & 13L & 156 & -22L \\ -13L & -3L^2 & -22L & 4L^2 \end{bmatrix} \tag{3-6}$$

with $U = \frac{d^2}{dy^2} N(y_i)$ and $N(y_i)$ denoting the shape function introduced in Eq. 3-1. Here, the material E-modulus E, surface moment of inertia I, density of the material ρ and the area of the cross-section A model the beam's geometric and material properties. The subscript $_i$ denotes the fact that this matrix merely describes the evolution of the states of one element, i and thus only its two nodes.

From these elemental matrices, the system K and M matrices can be constructed as described in [19]. These system K and M matrices correspond to the matrices introduced in Eq. 3-3, describing the dynamics of the entire structure through the EOMs. It is important to note that at this point, the appropriate boundary conditions need to be introduced to keep the K and M matrices from staying singular. For the flexure in Figure 3-1, both degrees of freedom of the first node are removed to simulate a fixed base. Also, the rotational DOF of the top node is removed to simulate a sliding constraint. Since this fully constrains the structure in space, and only allows for movement through deformation, the system K and M matrices will have full rank.

For the system damping matrix C', modal damping is used, which will be introduced after the modal decomposition is discussed.

It is now possible to describe the system using a second order ordinary differential equation. Often however, it is preferred to decouple this into two first order differential equations, and cast them into a linear state space formulation. This is done by defining a new state vector

$$\bar{d} = \begin{bmatrix} \bar{x} \\ \dot{\bar{x}} \end{bmatrix}, \tag{3-7}$$

where it is important to distinguish $\bar{d}$ from $d(y_i)$ and d_i. The newly introduced $\bar{d}$ denotes the full state vector with all nodal states and their velocities, whereas $d(y_i)$ and d_i denote the horizontal displacement of the continuous field and the nodes of element i respectively.

Using this state vector and Eq. 3-3, the system can be massaged into a linear time invariant state space system as:

$$\begin{aligned}\dot{\bar{d}} &= \underbrace{\begin{bmatrix} 0 & I \\ -M^{-1}K & -M^{-1}C' \end{bmatrix}}_{A_c} \bar{d} + \underbrace{\begin{bmatrix} 0 \\ -M^{-1}B' \end{bmatrix}}_{B_c} f \\ &= A_c\bar{d} + B_c f \end{aligned} \tag{3-8}$$

Where $A_c \in \mathbb{R}^{4n\times 4n}$ and $B_c \in \mathbb{R}^{4n\times 1}$ are the dynamics and input matrices respectively. Here, with n representing the amount of nodes in the system. To differentiate between these matrices and their discrete time counterparts, subscript $_c$ is introduced to emphasise these continuous time matrices.

The system dynamics can thus be represented as a linear time invariant (LTI) state space dynamical equation in 'nodal' space (using nodal coordinates). It can however be seen that the state of this system $\bar{d} \in \mathbb{R}^{4n\times 1}$ scales with four times the amount of nodes (two DOF's per node, with the DOF and their velocities). Since complex structures require many nodes, this scaling is undesired since it increases the complexity of the dynamical system rapidly. This can become problematic for large or complex systems requiring many nodes, or systems that need to be evaluated at high sampling rates like high-tech and fast positioning systems discussed in this work. These systems often have important dynamics in the range of 100 Hz or higher. To be able to accurately reconstruct both amplitude and phase, it is thus important to sample at least 10 times as fast, thus quickly resulting in a sampling frequency of 1Khz [20] becoming infeasable for large system state definitions. In addition, the filters introduced in this work aim at estimating the modal contributions, which are not yet represented in the state vector.

To resolve this, a model reduction can be applied by modal decomposition and truncation. Here, the system state is reduced to only interesting dynamics, and the desired modal contribution is introduced into the state vector.

This modal decomposition is based on the assumption that any (both forced and unforced) vibration in the physical domain can be decomposed in an infinite set of eigenmode vibrations [19]. Here, it is important to introduce amount of eigenmodes modelled N, which is different from the shape function $N(y)$ introduced in Eq. 3-1.

These eigenmodes are found by solving the undamped eigenvalue problem

$$(K - \omega^2 M)\bar{v} = 0, \tag{3-9}$$

where ω represents the eigenfrequency, and $\bar{v}$ its corresponding eigenvector which physically interprets to an eigenmode. Here the following assumption is implicitly made:

Assumption 4. *The system natural damping is sufficiently low,*

which allows for the imaginary parts of this eigenvalue problem to be neglected since they will not significantly impact the frequency or shape of the modes. The decomposition can

then be expressed as:

$$\begin{aligned}\bar{x} &= \eta_1\bar{v}_1 + \eta_2\bar{v}_2 + \eta_3\bar{v}_3 + \dots \eta_N\bar{v}_N \\ &= \underbrace{\begin{bmatrix}\bar{v}_1 & \bar{v}_2 & \bar{v}_3 & \dots & \bar{v}_N\end{bmatrix}}_{\Phi} \underbrace{\begin{bmatrix}\eta_1 \\ \eta_2 \\ \eta_3 \\ \vdots \\ \eta_N\end{bmatrix}}_{\bar{z}} \\ &= \Phi\bar{z}, \end{aligned} \tag{3-10}$$

where η represents the desired modal contribution. This is a scaling of how much the corresponding eigenmode is 'participating' in the current state or vibration of the system. The matrix Φ now contains all eigenvectors, and the vector $\bar{z}$ the modal participations. Eq. 3-10 can now be interpreted as a coordinate change of the state variable $\bar{x}$ (the original state vector of the EOMs as introduced in Eq. 3-3) to $\bar{z}$ (The state vector in modal space). Applying this to Eq. 3-3, and pre-multiplying with Φ^T evaluates to:

$$\Phi^T M\Phi\ddot{\bar{z}} + \Phi^T C'\Phi\dot{\bar{z}} + \Phi^T K\Phi\bar{z} = \Phi^T B' f. \tag{3-11}$$

To simplify this, $\Phi^T M\Phi = I$ can be defined by mass-normalising Φ. This is permitted since the eigenvectors $\bar{v}_k$ for $k = 1 : N$ have arbitrary scaling. It can also be noted that this results in $\Phi^T K\Phi = \Omega^2$ where $\Omega^2 = \text{diag}\begin{bmatrix}\omega_1^2 & \omega_2^2 & \dots & \omega_N^2\end{bmatrix}$. Which reduces Eq. 3-11 to:

$$\ddot{\bar{z}} + \Phi^T C'\Phi\dot{\bar{z}} + \Omega^2\bar{z} = \Phi^T B' f. \tag{3-12}$$

Again, this represents a second order differential equation, which can be decoupled into two first order equations as done in Eq. 3-8 by defining $\bar{q} = \begin{bmatrix}\bar{z} \\ \dot{\bar{z}}\end{bmatrix}$ and constructing the state space dynamics equation:

$$\dot{\bar{q}} = \underbrace{\begin{bmatrix}0 & I \\ -\Omega^2 & -\Phi^T C'\Phi\end{bmatrix}}_{A_{cm}}\bar{q} + \underbrace{\begin{bmatrix}0 \\ \Phi^T B'\end{bmatrix}}_{B_{cm}} f. \tag{3-13}$$

In this notation, the subscript $[]_{cm}$ denotes the continuous time modal matrix. Also, $A_{cm} \in \mathbb{R}^{2N\times 2N}$ and $B_{cm} \in \mathbb{R}^{2N\times 1}$ now scale with the amount of modelled modes, which is independent of the amount of nodes used in the discretisation. In addition, the desired modal contributions η are introduced into the state vector.

So far, a pre-determined damping matrix C' has been assumed. As mentioned before, this matrix will be determined using modal damping, where the damping is assumed proportional to the k^{th} modal frequency as $2\xi_k\omega_k$. The damping matrix is then defined as:

$$\Phi^T C'\Phi = \underbrace{\text{diag}(\begin{bmatrix}2\xi_1\omega_1 & \dots 2\xi_N\omega_N\end{bmatrix})}_{C_m}, \tag{3-14}$$

where ξ_k is the modal damping coefficient which can be determined using an operational modal analysis. Here C_m is also introduced as the modal counterpart of the damping matrix used in the standard EoM in Eq. 3-3.

Comparing equation Eq. 3-3 to Eq. 3-12, it is important to notice the same dynamical system is represented. The state of the system has only changed from the displacement and the rotations (and their velocities) of the nodes, to the modal contributions and the modal velocities. From here on, this dual space is called 'modal space' compared to regular 'nodal space' introduced before. In a spatially continuous domain, the response can be perfectly captured by an infinite amount of vibrational modes. This however is not the goal of this model reduction since we would like to reduce the dimensionality to a tractable problem. Most dynamical responses can be represented by a finite set of modes. This gives rise to the truncated model, where only the lowest N modes are taken into account in modelling. Thus reducing the dimensionality of the problem from a $4n$ state vector in the LTI system, to a $2N$ state vector with $N << n$. With N also independent of the amount of nodes and elements the structure is modelled with. This thus allows for the structure to scale arbitrarily, or the meshing to be sized appropriately without impacting the final state space system and potentially reducing real-time capabilities of the methods introduced later in this work. In reality, the true model contains infinite modes, and the truncated model can be chosen up to modes of a frequency where the structure is not exited anymore. Or where the magnitude of the modes has decreased sufficiently to not influence the important dynamics anymore.

For the compliant motion stage, a total of 2 modes is used as a modal reduction.

The dynamics of the system can thus be captured by Eq. 3-13 in modal space. To complete the LTI state space system however, the measurement equations also have to be set up. This will be done in the next section.

3-1-2 Measurements

For the measurement models, three types of measurement will be used. The first and foremost will be a horizontal position measurement of the tip of the beam. The second type of measurement will be acceleration measurement, and the third will be a strain measurement. For this section, the modelling of each type of measurement will be introduced followed by the final measurement equation to conclude the full system model.

Position measurement

The first measurement to model is the position measurement since this is directly represented in the state vector of the system in nodal space. Also, the measurement can be done on the stage when assumption 1 holds.

Since the position is already represented in the state in nodal space, the measurement equation for a position measurement merely transforms the state back from modal to nodal coordinates, and selects the appropriate measurement location as:

$$y_{\mathrm{p}} = \begin{bmatrix} S_{\mathrm{p}}\Phi & 0 \end{bmatrix} \bar{q} \tag{3-15}$$

Where S_p contains the shape function vector $\bar{N}(y)$ introduced in Eq. 3-2 evaulated at the measurement location to interpolate the nodal values. In this case, since the position measurement is located at the tip of the beam (directly at a node), C_p contains only a 1 at the d_n location (displacement of the n^{th} node) since only $y_n = 1$ with all other $y's$ equal zero. This results in $C_p = \begin{bmatrix} 1 & 0 & \dots & 0 \end{bmatrix}$. It is important to recall however that through the use

of the shape function vector, the position at any location along the flexure can be extracted in this way. Not limited to nodal locations.

Acceleration measurement

The next type of measurement to obtain is the acceleration measurement. Since the acceleration of the system is not represented in the state vector, it requires a different approach then the previous position measurement. To still obtain the acceleration, the expression for the acceleration in Eq. 3-12 is re-used and pre-multiplied by $S_a\Phi$ to obtain

$$y_{\mathrm{a}} = \begin{bmatrix} -S_a\Phi\Omega^2 & -S_a\Phi C_m \end{bmatrix} \bar{q} + S_a\Phi\Phi^T B' f. \tag{3-16}$$

Here, Φ again transforms back to nodal coordinates, and S_a again contains the interpolation function vector $\bar{N}(y)$ evaluated for the appropriate measurement location as introduced before.

It is noteworthy that only the acceleration in the lateral direction (direction of deformation) is extracted. The linear model used can not produce any information about acceleration in the axial direction since the model only allows for deformation in lateral direction. Axial deformation would introduce geometrical non-linearities and thus require non-linear techniques. This thus also prescribes the sensor orientation that is required.

Strain measurement

In addition to position and acceleration measurements, strain measurements are also required. For this, the models mentioned in [21] and [8] will be used. Here, the strain over the gauge is computed as:

$$\epsilon = \underbrace{h \int_0^{L_p} \frac{d^2}{dy^2} \bar{N}(y) dy}_{S_s} \bar{d}, \tag{3-17}$$

where h is the distance of the patch from the neutral axis of the beam, L_p the total length of the strain gauge, $\bar{N}(y)$ again the shape function vector and $\bar{d}$ the nodal state vector. Evaluating this expression just results in the difference of the rotation at the ends of the patch times the distance from the neutral axis which is a well-known result. The resulting measurement equation can thus be formulated as:

$$y_s = \begin{bmatrix} S_s\Phi & 0 \end{bmatrix} \bar{q}. \tag{3-18}$$

In addition to this measurement equation, the mass and stiffness of the strain gauge are also added to the beam by extending the surface moment of inertia in a standard way. This will not be elaborated on further, but can be found in the code in [22] since it follows a similar procedure as the general dynamics modelling.

To conclude the measurement model, and find the outputs of the system, Eq. 3-15, Eq. 3-16 and Eq. 3-18 can be combined in the preferred configuration. This configuration depends on the location and amount of sensors used. The complete measurement equation for the case

where all three measurements are used once is still presented for completeness as:

$$\bar{y} = \underbrace{\begin{bmatrix} S_p\Phi & 0 \\ -S_a\Phi\Omega^2 & -S_a\Phi C_m \\ S_s\Phi & 0 \end{bmatrix}}_{C_{cm}} \bar{q} + \underbrace{\begin{bmatrix} 0 \\ S_a\Phi\Phi^T B' \\ 0 \end{bmatrix}}_{D_{cm}} f. \tag{3-19}$$

Thus together with the dynamics equation in Eq. 3-13 completing the linear state space formulation for the compliant guidance flexure with position, acceleration and strain measurements in continuous time modal space. The model will be validated after the algorithms and the experimental setup is introduced.

For completeness however, the continuous time model needs to be discretised. This is generally done using the Zero Order Hold (ZOH) assumption [23]. Applying this to Eq. 3-13 and Eq. 3-19, the full discrete model can be introduced as:

$$\begin{aligned} \bar{q}_{k+1} &= A\bar{q}_k + Bf_k \\ \bar{y}_k &= C\bar{q}_k + Df_k \end{aligned} \tag{3-20}$$

Which summarises the state space model formulation in discrete space.

3-2 Algorithms

Using the model developed in the previous section, simultaneous input and state estimation can be discussed. For this, the algorithms that are evaluated from SHM in civil engineering for use in compliant motion stage guidance flexures. Here, it is important to note that classical observer based schemes are not possible for such systems since they generally require information about the inputs to the system. Recall that section 3-1 drew the system boundary around the flexure, with merely a horizontal interaction force at the tip of the flexure representing the presence of the stage itself. This force acts as an input to our system and can not be measured in any way. It is thus assumed unknown.

To circumvent this issue, three input and state estimation algorithms will be introduced, which, in conjunction the the state of the system also estimate the input. Since these three algorithms all follow the recursive Bayesian framework, the general Kalman filter is still introduced first in subsection 3-2-1 to show general notation and assumptions. This can then later easily be extended to the augmented Kalman filter (AKF) in subsection 3-2-2, Dual Kalman filter in subsection 3-2-3 and Gilijns de Moor Filter (GDF) in subsection 3-2-4.

3-2-1 General Kalman Filter

One disadvantage of more traditional observers like the Luenberger observer is the assumption of a deterministic system model. Through this assumption, the system is assumed fully deterministic, and stochastic effects like measurement or even process noise can not be taken into account. Noise thus has a significant impact on the performance. To take noise into account, a stochastic state estimator can be developed through the assumption of Bayes rule. The most prominent result of these class of filters is the Kalman filter, which assumes the process and measurement noise as stochastic processes [24; 25; 26]. The input force f_k is assumed known in this subsection for the purpose of introducing the general Kalman filter.

In reality however, this is not the case, as will be addressed in subsequent sections.

To do this, the Linear Time Invariant state space model formulation introduced in Eq. 3-20 is modified to:

$$\begin{aligned} \bar{q}_{k+1} &= A\bar{q}_k + Bf_k + \bar{w}_k \\ \bar{y}_k &= C\bar{q}_k + Df_k + \bar{v}_k \end{aligned} \tag{3-21}$$

Here, $\bar{w}_k$ represents the process- and $\bar{v}_k$ measurement noise and are assumed to be Gaussian distributed with zero mean and covariance matrix Q and R respectively:

$$\bar{w}_k \sim \mathcal{N}(0, Q) \tag{3-22}$$

$$\bar{v}_k \sim \mathcal{N}(0, R) \tag{3-23}$$

As they are assumed random Gaussian, they are also assumed to be wide-sense stationary. In addition to this, they are assumed uncorrelated with the estimation error.

Since most methods introduced in the next sections rely on some sort of Kalman filtering framework, this will be introduced here very shortly. From its introduction in 1960 [25][24] by R.E. Kalman, this eponymous filter has been widely studied and implemented in a surplus of systems and applications. Because of this, only the resulting equations will be given here, as the derivation can be found in almost any textbook [27; 28; 29].

The main idea behind the filter, is a two-step process where first, a prediction is made about the next state, and in the next filtering step this prediction is improved based on a new measurement.

The first step is referred to as the time update. Here, the state space system model is used to make a prediction about the state of the system at the current time step based on the estimated state at the previous time step:

$$\hat{\bar{q}}_{k|k-1} = A\hat{\bar{q}}_{k-1|k-1} + Bf_{k-1}. \tag{3-24}$$

It is important to note that this prediction requires information about the input to the system at the previous time step. The subscript $_{k|k-1}$ denotes the value at the current time step k, conditioned on the previous time step $k-1$.

In addition to the next state, the time update also predicts the covariance of the error of the next state defined as $P_{k|k-1} = E[(\bar{q}_k - \hat{\bar{q}}_{k|k-1})(\bar{q}_k - \hat{\bar{q}}_{k|k-1})^T]$ which evaluates to:

$$P_{k|k-1} = AP_{k-1|k-1}A^T + Q \tag{3-25}$$

The second step is referred to as the measurement update, where, upon arrival of a new measurement of the system $\bar{y}_k$, the prediction done in the time update of the previous time step is 'corrected'. This is done by a minimum variance unbiased estimate of the current state, based on the measurement and a prior (the time update). The measurement update for both the state and covariance matrix are given as:

$$\hat{\bar{q}}_{k|k} = \hat{\bar{q}}_{k|k-1} + K_k(y_k - C\hat{\bar{q}}_{k|k-1}) \tag{3-26}$$

$$P_{k|k} = P_{k|k-1} - K_kCP_{k|k-1} \tag{3-27}$$

With the Kalman gain at the current time step K_k given by:

$$K_k = P_{k|k-1}C^T(CP_{k|k-1}C^T + R)^{-1} \tag{3-28}$$

It is important to note that the Kalman filter can be represented in multiple ways for different applications like one step ahead prediction. As the purpose here is to estimate the state of a linear time invariant system at the current time step, the most general filtering representation is chosen. For innovation, one step ahead prediction, smoothing representations or in-depth derivations the reader is referred to [28].

The main advantage of the Kalman filter is that it makes an LQ- optimal trade-off between the model prediction, and the measurement based on the process and measurement noise covariance matrices Q and R, which results in the minimum variance unbiased estimate of the state. For LTI systems, the Kalman gain K_k will converge to the steady-state value defined by the solution to the Discrete Algebraic Riccati Equation (DARE).

This also introduces the a significant disadvantage, which is the tuning of the Q and R matrices. Tuning can be used to set the covariance of the process noise $\bar{w}_k$ and the measurement noise $\bar{v}_k$ respectively. The Q matrix allows for tuning of the 'confidence' in the model prediction as the $\bar{w}_k$ also embodies modelling errors. Larger Q will result in the filter 'relying' more on the measurements instead of the time update. The R matrix on the other hand gives an interval of uncertainty for the measurements as $\bar{v}_k$ embodies measurement noise. A larger R will thus result in the filter 'relying' more on its own model prediction then the available measurements.

As the amount of modelling error, or the amount of noise is not exactly known in the implementation of this work, these matrices require tuning which can be tedious and impact performance significantly.

It is worth mentioning again that this filtering scheme requires information about the input of the system f_k which is not known for the current system as this is merely an interaction force between the flexure and stage. To resolve this issue, the next three sections introduce output-only filters which simultaneously estimate the input and the state of the system.

3-2-2 Augmented Kalman Filter (AKF)

The first method introduced here is one of the most straight-forward extensions of the Kalman Filter algorithm introduced in subsection 3-2-1. The main working principle is based on an augmented state formulation of the system dynamics which can directly be plugged into the regular Kalman Filter framework.

Although the augmented Kalman filter formulation has been around for a while [28; 30] (often referred to as the output-only formulation of the Kalman filter), its introduction in structural mechanics was done by E.Lourens in 2012 [17]. The filter relies on a relatively simple augmented state formulation of the system model which is derived by first recalling the linear time invariant state space model for the system dynamics introduced in Eq. 3-21. To be able to formulate an autonomous system from this equation, some process equation needs to be assumed for the discrete time propagation of the input. For general inputs, a zeroth order random walk model is often used as:

$$f_{k+1} = f_k + z_k \tag{3-29}$$

Where f_k represents the input to the system at time step k. z_k Represents a stochastic variable modelling the derivative of f as varying in a random fashion. The assumption is made that this variable varies along a zero mean normal distribution. For more specific

system inputs, more specific application-tailored input models can be used like sinusoidal [28] or non-white noise sequences [31]. For this work however, the generic Martingale process equation as introduced in Eq. 3-29 is assumed as a general-purpose input model since there is no information about the shape of the actual interaction force available.

Using this, and the process equation with assumed noise terms in Eq. 3-21, the augmented autonomous system can be constructed as:

$$\begin{aligned}\begin{bmatrix}\bar{q}_{k+1}\\ f_{k+1}\end{bmatrix} &= \begin{bmatrix}A & B\\ 0 & I\end{bmatrix}\begin{bmatrix}\bar{q}_k\\ f_k\end{bmatrix} + \begin{bmatrix}\bar{w}_k\\ z_k\end{bmatrix}\\ \bar{y} &= \begin{bmatrix}C & D\end{bmatrix}\begin{bmatrix}\bar{q}_k\\ f_k\end{bmatrix} + \bar{v}_k\end{aligned} \tag{3-30}$$

This can be summarised in the new system formulation as:

$$\begin{aligned}\bar{q}^a_{k+1} &= A^a\bar{q}^a_k + \bar{\zeta}_k\\ \bar{y}_k &= C^a\bar{q}^a_k + \bar{v}_k\end{aligned} \tag{3-31}$$

Where the superscript ^{a} denotes the augmented formulation of the process matrix A, the measurement matrix C and the state vector $\bar{q}$. The new process noise vector $\bar{\zeta}_k$ is again assumed zero mean Gaussian with an augmented covariance matrix:

$$Q_\zeta = \begin{bmatrix}Q & 0\\ 0 & Q_f\end{bmatrix} \tag{3-32}$$

which consists of the process noise $\bar{w}_k$ covariance Q augmented by the input variation covariance matrix Q_f. Eventhough f in this case remains scalar, and thus also its covariance matrix, it is still noted down as matrix to allow for extension to multi input systems.

It is important to note that the system dynamics are now formulated in an autonomous way, where there is no need for the system input signal when estimating the state. This system formulation can easily be input into a regular Kalman filtering framework as introduced in subsection 3-2-1 which then recursively estimates the augmented state vector. Thus also making an estimate of the system input f along with the original state vector $\bar{q}$.

As straightforward as this method may seem, it does have some significant drawbacks [32]. The first major drawback is the necessity for tuning of the covariance matrices Q, R and Q_f. These first two are inherited from the regular Kalman filter framework as mentioned in subsection 3-2-1 but do require offline tuning. The last covariance matrix (Q_f) however, represents a significant problem for real world applications. This is due to the fact that the input variation covariance matrix Q_f defines an interval on which the derivative of the input is expected to vary along a Gaussian distribution. In most applications however, the amount of variation in the derivative of the input is as unknown as the input itself, which makes the process of finding an appropriate value or even order of magnitude non-trivial [32]. M. Verhaegen [28] presents a illustrative example of this problem by applying the AKF to estimate the wind excitation for a large wind turbine. Here, the influence of this tuning parameter is well illustrated by comparing the estimated input to the true value for different tuning parameters. In real world systems however, the true input signal is unknown, which complicates this tuning process and raises the need for regularization methods like L-curve tuning [17].

For this implementation however, it is shown the system formulation becomes inherently unstable when only acceleration measurements are used, resulting in drift in the estimation [13]. This is a majour drawback for the use in civil structures, where acceleration measurements are much easier to obtain then strain measurements. For high-tech compliant motion stages however, this instability can be circumvented by applying strain or position measurements.

The addition of the input to the state vector as done in this AKF formulation is not the only way to circumvent the lack of knowledge about the input however. A second school of thought aims at estimating the input in a separate Kalman filtering step opposed to one big one as in the AKF. This will be introduced in the next section.

3-2-3 Dual Kalman Filter (DKF)

To circumvent the numerical instability issues present in the AKF formulation when using acceleration-only measurements, Papadimitriou et al. have proposed a dual formulation of the Kalman filter referred to as the Dual Kalman Filter (DKF) in [14]. In this formulation, the same assumptions on the input process equation are made, but solved in two sequential Kalman filtering steps instead of one large step as in the AKF.

This starts by again assuming the process equation for the input as a random walk model as in Eq. 3-29:

$$f_{k+1} = f_k + z_k \tag{3-33}$$

To set up the first step of the dual Kalman filtering scheme, this random walk model for the input is assumed as process equation, where the system measurement equation from Eq. 3-21 is taken as output measurement equation:

$$\begin{aligned} f_{k+1} &= f_k + z_k \\ \bar{y}_k &= C\bar{q}_k + Df_k + \bar{v}_k \end{aligned} \tag{3-34}$$

Assuming this model for the first Kalman filtering step, the time and measurement updates can be set up as introduced in subsection 3-2-1. This then evaluates to the first kalman filtering step estimating the input based on the previous estimate of the input and the previous state.

Input time update:

$$\begin{aligned} \hat{f}_{k|k-1} &= \hat{f}_{k-1|k-1} \\ P^f_{k|k-1} &= P^f_{k-1|k-1} + Q_f \end{aligned}$$

Input measurement update:

$$\begin{aligned} K^f_k &= P^f_{k|k-1}D^T(DP^f_{k|k-1}D^T + R)^{-1} \\ \hat{f}_{k|k} &= \hat{f}_{k|k-1} + K^f_k(\bar{y}_k - C\hat{\bar{q}}_{k-1|k-1} - D\hat{f}_{k|k-1}) \\ P^f_{k|k} &= P^f_{k|k-1} - K^f_k DP^f_{k|k-1} \end{aligned} \tag{3-35}$$

It can be seen here, that the sought-for state estimate $\hat{\bar{q}}$ plays the role of the unknown input. As this state is also not known, the state vector as estimated in the previous time step is used for the input estimation at the current time step.

After the input estimation step, the state is estimated using the previously estimated input.

For this, the conventional model from Eq. 3-21 is assumed, and plugged into the regular Kalman filtering framework. The time and measurement update then equate to:

State time update:

$$\hat{\bar{q}}_{k|k-1} = A\hat{\bar{q}}_{k-1|k-1} + B\hat{f}_{k|k}$$
$$P^q_{k|k-1} = AP^q_{k|k-1}A^T + Q$$

State measurement update

$$K_k = P^q_{k|k-1}C^T(CP^q_{k|k-1}C^T + R)^{-1}$$
$$\hat{\bar{q}}_{k|k} = \hat{\bar{q}}_{k|k-1} + K_k(\bar{y}_k - C\hat{\bar{q}}_{k|k-1} - D\hat{f}_{k|k})$$
$$P^q_{k|k} = P^q_{k|k-1} - K_kCP^q_{k|k-1}$$

This second step thus evaluates to a Kalman filtering step where the unknown input is replaced by the optimal estimate made by the first Kalman filtering step. For a more detailed filter evaluation, the reader is referred to [14]. It is noted that the uncertainty of the input estimate is not represented in the state covariance time update. This however is not mentioned in the original work, and is not added here as augmenting these filters is outside the scope of this work.

In the aforementioned work, the stability of the filter is shown using numerical simulations and a real-world example [32]. Here, the numerical issues arising with the AKF are shown to be circumvented due to the fact that the matrices are not augmented in the same way, and thus do not grow singular. This is however only shown in simulation and through experimentation, and not mathematically substantiated. The remaining drawback to this filter thus remains the necessity of tuning of the Q, R and Q_f matrices. The authors do show that an experts guess on the input variation covariance matrix does yield a good starting point, but tuning can still be tedious.

To try and circumvent this last issue, the third filter has been introduced where the first Kalman filtering step in the DKF is substituted for a general recursive weighted least squares estimate. This filter will be introduced in the following section.

3-2-4 Gilijns de Moor Filter (GDF)

From the previous sections, it is clear the AKF and DKF require information about the input to tune the input covariance Q_f. This limitation reduces real-life applicability as often no information about this input is available [32]. To combat this, a proposition of a filter for minimum variance, unbiased, simultaneous input and state estimation of linear systems without direct feedthrough was first proposed by Kitanidis in 1987 [33]. This filter did not make any a-priori assumptions about the system input sequence which circumvents the necessity of tuning. This filter however was not globally optimal in a mean-square-error sense[14]. Kitanidis's result was extended by Darouach and Zasadzinski [34] with stability and convergence conditions. After Hsieh establishes the connection between Kitanidis's filter and two-stage filters in [35], this filter is further developed by Gillijns and de Moor in 2007 in [36] where they propose a new minimum variance unbiased filter formulation which can be re-formulated in the filter proposed by Kitanidis, and produces the same input estimate as the filter proposed by Hsieh thus retaining both optimality properties. The proposed filter in [36] however only

holds for systems without direct feedthrough. The filter is later reformulated to also support these types of systems in [37]. For clarity, this filter formulation is presented here.

For a full and detailed derivation of the filter equations, the reader is referred to [36], with the presentation of the filter equations for direct-feedthrough systems in [37].

These filter equations consist of three general parts:

- Time update
- Input estimate
- Measurement update

The first step is the time update of the filter, where, analogous to the Kalman Filter, a prediction is done about the current state based on the previous one:

Time update:

$$\hat{\bar{q}}_{k|k-1} = A\hat{\bar{q}}_{k-1|k-1} + B\hat{f}_{k-1}$$
$$P^q_{k|k-1} = \begin{bmatrix} A & B \end{bmatrix} \begin{bmatrix} P^q_{k-1|k-1} & P^{qf}_{k-1} \\ P^{fq}_{k-1} & P^f_{k-1} \end{bmatrix} \begin{bmatrix} A^T \\ B^T \end{bmatrix} + Q$$

The second step is the input estimation. For this, a general linear estimator for the system defined in Eq. 3-21 is assumed in [36]. After enforcing minimum variance and unbiasedness, this linear estimate $\hat{f}$ and its covariance matrix P^f evaluate to:

Input estimate:

$$\tilde{R}_k = CP^q_{k|k-1}C^T + R$$
$$M_k = (D^T\tilde{R}_k^{-1}D)^{-1}D^T\tilde{R}_k^{-1}$$
$$\hat{f}_k = M_k(\bar{y}_k - C\hat{\bar{q}}_{k|k-1}) \tag{3-36}$$
$$P^f_k = (D^T\tilde{R}_k^{-1}D)^{-1} \tag{3-37}$$

It can be seen in Eq. 3-36 that this resembles the solution to weighted least squares problem with weighting matrix L and $(LL^T)^{-1} = \tilde{R}_k^{-1}$. The unbiased and minimum variance properties are proven in [36] along with a detailed derivation and will not be repeated here.

The third step is the measurement update, where analogous to the Kalman filter the estimates of the state and its covariance are updated using the new measurement. With this update, also the cross covariance of the input and the state is estimated.

Measurement update:

$$K_k = P^q_{k|k-1}C^T\tilde{R}_k^{-1}$$
$$\hat{\bar{q}}_{k|k} = \hat{\bar{q}}_{k|k-1} + K_k(\bar{y}_k - C\hat{\bar{q}}_{k|k-1} - D\hat{f}_k) \tag{3-38}$$
$$P^q_{k|k} = P^q_{k|k-1} - K_k(\tilde{R}_k - DP^f_kD^T)K_k^T \tag{3-39}$$
$$P^{qf}_k = (P^{fq}_k)^T = -K_kDP^f_k \tag{3-40}$$

It is important to note here that the measurement and time update are analogous to the original Kalman filter as introduced in subsection 3-2-1 with the only exception that the input is replaced by the optimal estimate from Eq. 3-36. The equations thus reduce to the regular Kalman filter when $B = D = 0$.

The GDF has its roots in regular system theory, but was introduced in structural dynamic by E. Lourens in [18] where the formulation was also extended to circumvent the numerical instabilities occurring when more sensors than modelled system states are used. This is often the case for real-life systems where a modally decomposed model is implemented. More work has been done on this filter by for example extending to the case where the process and measurement noise are correlated in [38]. This however is outside the scope of this work.

A significant advantage of the GDF formulation is the optimal estimate of the input which doesn't assume any process equation through the use of the Weighted Least-Squares estimate. This eliminates the need for apriori information about the input sequence and tuning of a possible Q_f matrix.

One disadvantage of this filter however is the fact that the MVU estimate of the input relies heavily on the direct feedthrough matrix D. As shown in the measurement model that will be used in Eq. 3-19, this matrix contains zeros for the position and strain measurements, and only exists for the acceleration measurement. It is thus not possible to evaluate this filter when only position or strain measurements are used. Acceleration measurements are required to ensure the existence of the MVU estimate of the input in Eq. 3-36.

Chapter 4

Simulations

To show validity of the algorithms introduced in the previous section, they are implemented in simulation. This section first describes the setup process shortly in section 4-1 whereafter the simulation results are presented in section 4-2. It is important to note here no conclusions can be drawn about the actual performance of the filters since they have to be implemented in the true system for this. This section is however used to show validity, and a relation between the state estimate and the estimate of the tip location, which allows for simplification of the true setup since it's then not required to measure the true states of the system for validation. Only a tip location measurement for validation suffices.

4-1 Setup

For simulation, the model introduced in section 3-1 is set up and simulated in a similar manner to the true system as introduced later in Chapter 5. All system parameters are kept the same to be able to compare simulation to the true system response. The full simulation setup will not be discussed here. For more details on the parameters and method used, the reader is referred to Appendix A.

For this section however, it is important to note the model that is simulated is the model closest to the 'true' system as introduced in Chapter 5 without the addition of any modelling errors. The signals however are augmented with normally distributed noise with similar covariance as measured from the actual setup. The system is perturbed by a step on the force input at the tip of the beam from 0.5s to 1.5s and allowed to dampen out. The resulting simulated signals for the complete time response are presented in Appendix A.

As for the filters, the same tuning parameters are used as later presented in subsection 5-3-2 for the true system to be able to draw conclusions about the filters that are implemented on the actual system. The model used for the filters however is corrupted with modelling errors as described in Appendix A to simulate an erroneous system model. The initial states of the filters are also offset from the true initial states since the these are assumed unknown.

It is important to note here that the filters are only allowed to use the acceleration at the

tip of the flexure measurement as well as the strain measurement at the base. This is due to limitations on the implementation of acceleration and position measurements in the true system, and also assumed here. In addition, no stage is simulated here as this is not included within the system boundary. Only the flexure with an input force at the tip, acceleration and position measurement at the tip, and strain measurement at the base at the same location as the true system.

4-2 Results

For the simulation results, interesting sections of the system and filter response are plotted in Figure 4-1. Here, the left figure provides a general overview of the interesting sequence where the right figure provides a zoomed in view of the area enclosed by the green dashed lines. The AKF, DKF and GDF are simulated, and their position estimation is plotted in the first row. The estimated first and second modal participation states are plotted in the second and third rows, and the input estimate is plotted in the last row. In addition to the filter response, the true values are also plotted in black for every signal. This allows for comparison between the filter estimate and the simulated value.

It can be seen in Figure 4-1 that all filters approximate the true response quite well. It is clear however the DKF systematically under estimates the signals, and the AKF passes through quite a bit of noise. The GDF performs the most consistent by coinciding with the AKF but not passing through any noise. To actually be able to evaluate their performance overall however, the Normalised Root-Mean-Squared error between the true value and filter estimate for all 4 signals are presented in Figure 4-2.

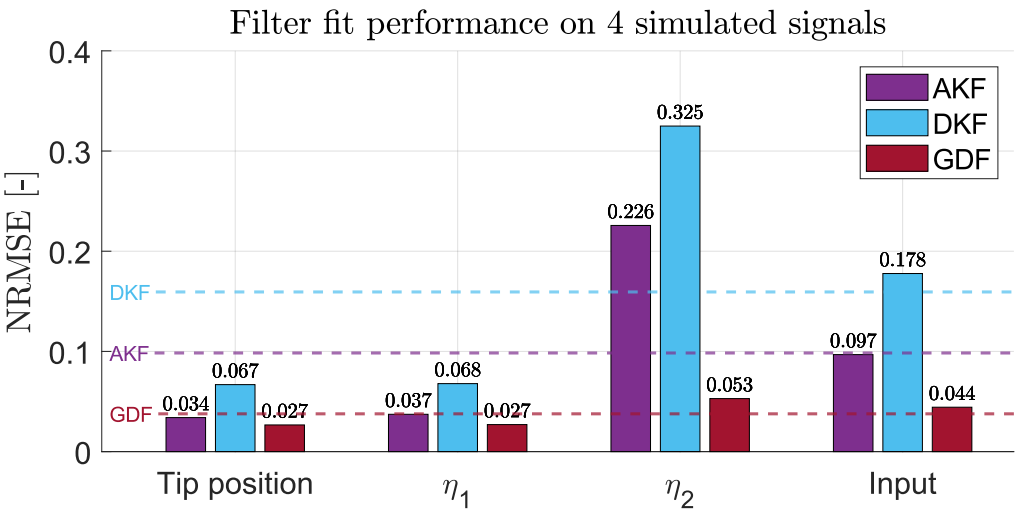

Figure 4-2: NRMSE fit scores for three input and state estimation algorithms on the simulated flexure tip location, first and second modal contribution and input.

Here, the observations from Figure 4-1 are also clearly represented, with the GDF performing the best over all estimated quantities. The evaluation of performance is however unimportant at this point. What is important is the observation that the states of the simulated model are estimated quite accurately by the GDF, whereas the AKF introduces a significant amount of

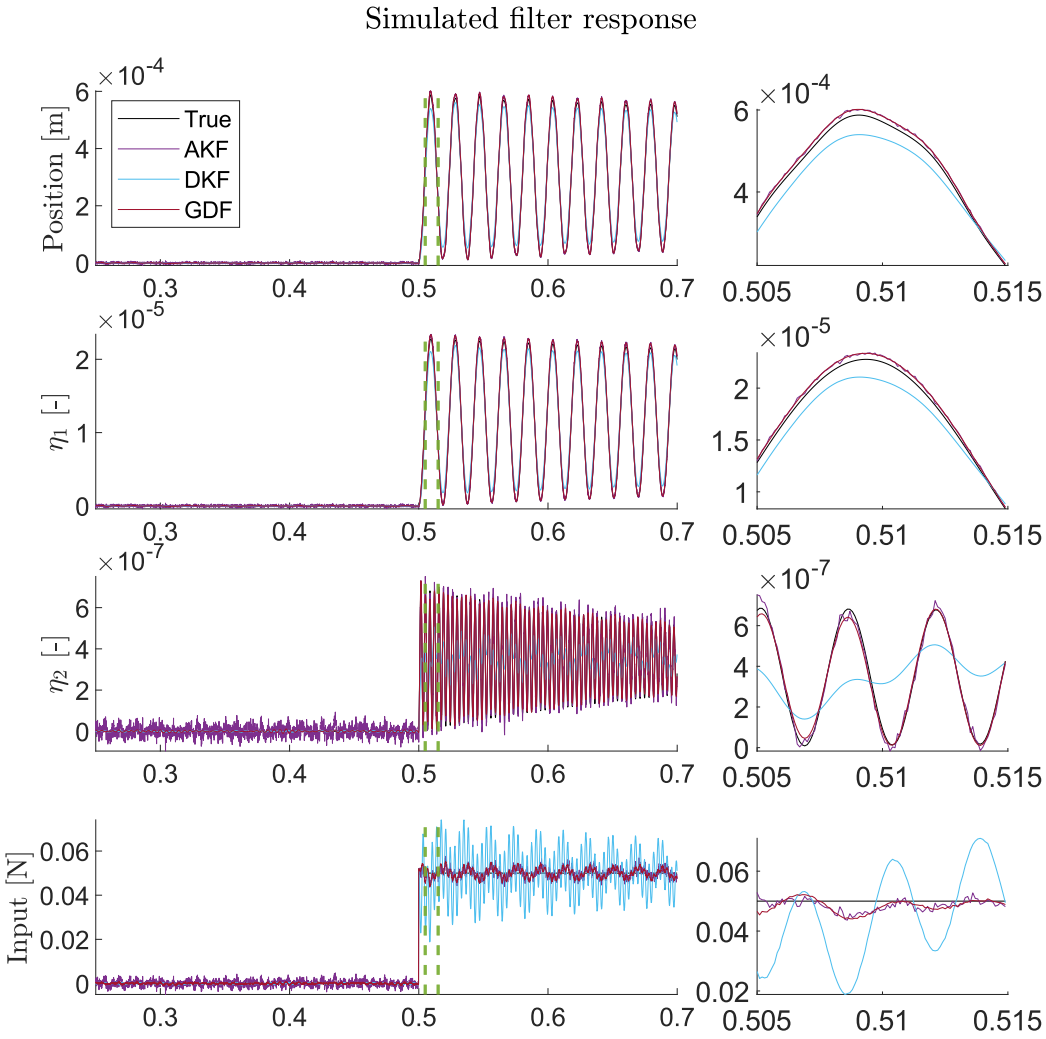

Figure 4-1: Simulated filter response for the AKF, DKF and GDF using noise strain and acceleration measurements and an erroneous model.

noise and the DKF seems to not be able to deal with these high frequencies. In Chapter 5, the implementation on the true system is presented. Here, it will become obvious the true states of the system are not measurable since only a measurement of the tip location, acceleration of the tip location and a strain measurement are feasable. The performance of the filters with respect to the true state estimation can thus not be evaluated. Since these filters are intended for full state estimation as stated by the research question introduced in section 1-3, it is important to still be able to draw conclusions about the capability of the filters to reconstruct the state.

This is also where this simulation is important. In Figure 4-2, it is shown the tip location is estimated quite accurately by all filters with similar performance the state estimate. Even

more importantly, since the tip location is dominated by the first mode, the fit score for this signal represents the fit score for the first mode quite well with a proportional relation being present for the second modal state. For the remainder of this work, the performance of the filters on the estimation of the tip location is thus assumed proportional to the state estimation performance.

Using this reasoning, conclusions about the state estimation quality of the filters can be drawn for the actual system without being able to measure the true states.

Conclusions about the performance of the filters can only be drawn when implemented in an actual system as presented in Chapter 5.

Chapter 5

Implementation

To be able to properly evaluate performance of the previously introduced algorithms, they are implemented on an experimental compliant motion stage setup. This setup resembles a 'fine stage' setup possibly used in a fine and course stage motion system using compliant flexures to position the stage accurately over a relatively small range of motion. The larger range of motion would be taken care of by the course stage which is not represented in this work.

For completeness, the setup is shortly introduced in section 5-1. For a more detailed overview of the hardware, software and design considerations made during manufacturing, the reader is referred to Appendix B where more elaboration is provided. Since the implementation of the filters presented in Chapter 3 is mainly a modelling problem, the identified plant is presented in section 5-2 to check validity of the previously constructed model. This model is then used in the implementation of the filters in section 5-3.

Also presented in this chapter is the design of experiments for filter validation in section 5-4. This concludes all methods used for result generation in the subsequent chapter.

5-1 Setup

In this section, the mechanical design is shortly presented. To do this, an overview of the final setup is first provided by Figure 5-1. Again, an in-depth overview is provided in Appendix B. As a general overview, Figure 5-1a presents the main components of setup for perspective. Figure 5-1b presents a close-up of the mechanical motion stage.

For the actual stage setup as can be seen in Figure 5-1b, a previously built setup is used which only required minor modifications. As this setup was already fitted with increased length flexures, and a race coil actuator it provides the perfect test platform for the evaluation of the dynamics of these compliant flexures. For this project however, new flexures are manufactured to increase observability of their second vibrational mode shape. The characteristics of these flexures are summarised in Table 5-1. The selection process is presented in section B-1.

The setup is controlled by an f28379d TI-Launchpad. The main purposes of this board are closed loop position control and data acquisition which is done in collaboration with a

Material	AISI 1095 Spring Steel
Length	100 mm
Width	12.7 mm
Height	0.4 mm

Table 5-1: Dimension and material of motion stage guiding flexures

connected PC. The board itself however runs completely stand-alone since all code is booted and run from flash, and the board is not powered from the PC. For data acquisition, the board sends over the signals of interest to the PC where they are logged.

For actuation, the TI-OPA548 opamp is embedded in a current amplifier. Dual DAC modules from the TI-Launchpad generate a differential voltage which is used as input voltage for the current amplifier. This voltage is proportional to the applied current in the race coil actuator, and thus to the force applied. The principles of race coil or Lorenz actuation are not recalled here as this is outside the scope of this work. It is important to mention however that current controlling this race coil allows for force control of the stage. The force generated is mainly used for closed loop position control together with a stage position measurement to reduce unwanted vibrations in the system. In addition to this, the closed loop position control is also used for reference tracking and disturbance generation.

For measurement, position, acceleration and strain sensors are implemented. The position measurement is handled by an RLE10 interferometer with its body mounted off to the side, but the laser head mounted close to the stage as can be seen in Figure 5-1b. The interferometer provides a relative position measurement in digital quadrature form to the IT-Launchpad which is read out by the dedicated eQEP module.

The acceleration measurement is done by the ADXL-356EVAL board mounted on top of the stage. This accelerometer is powered and directly read out by the TI-Launchpad and provides an acceleration measurement in the motion direction of the stage. Since the signal obtained by this accelerometer has been corrupted by significant amounts of noise as can be seen in Appendix B, the signal is additionally lowpass filtered using a 1Khz cutoff frequency to ensure all dynamics is untouched.

The last measurement that is implemented is the strain measurement, which is done by 2 HBM 10/120LY41 strain gauges mounted at the bottom of one of the flexures. This strain measurement is conditioned by the SCAIME CPJ module from which a voltage proportional to the strain can be read out by the TI-Launchpad. Since the strain gauges are mounted in a full Wheatstone bridge configuration, two dummy gauges are also mounted on a stationary and non-deforming piece of flexure material.

The setup can be programmed through a Simulink interface, which is also used for data acquisition and real-time monitoring. For a more detailed overview of the code running on this board, and calibration of the sensors and actuator presented, the reader is again referred to Appendix B.

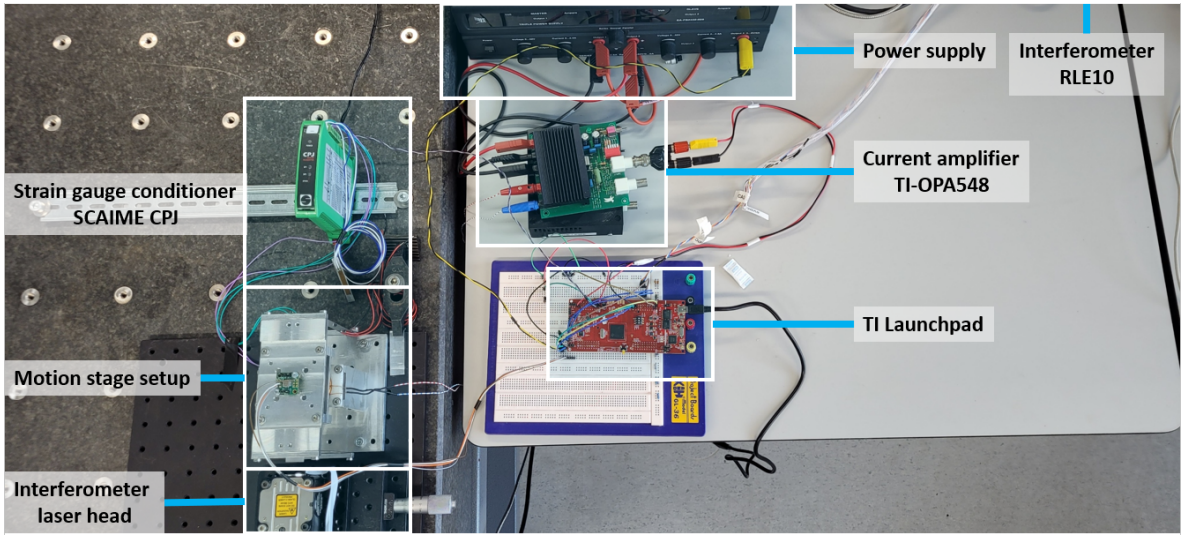

(a) Full setup overview

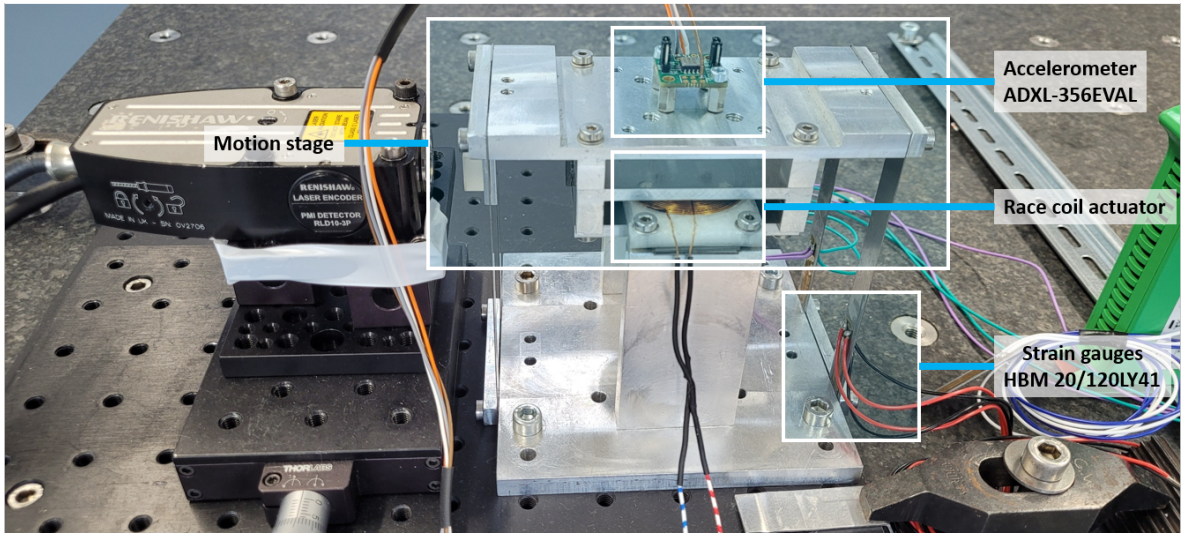

(b) Stage close-up

Figure 5-1: Setup and stage overview

5-2 Identification

To evaluate whether the model introduced in section 3-1 corresponds to the actual setup, the system is identified. The purpose of this is thus not to obtain an actually identified dynamical model, but merely to check validity of the first principles model derived in section 3-1. For this, it suffices to identify the interesting dynamics frequencies using short sine sweeps. This is done to be able to identify parts of the dynamics using different actuation gains which is necessary to prevent the large resonance peak at 6.6Hz from yielding too large of a displacement. This region is thus identified using 1% of the maximum actuation force, whereas the area around the second resonance peak is identified using 100% of the available actuation force. The resulting magnitude and phase responses are presented in Figure 5-2 where the expected dynamics derived from the model in section 3-1 is also presented.

It is important to mention here that this phase and magnitude response plot represent the entire stage setup, which is assumed to be symmetrical such that each flexure takes up one fourth the total force. The system boundary however still includes the stage itself, as this is where the input force is applied. In the model, an additional mass is thus added to the top of the flexure corresponding to one fourth of the total assumed stage mass as also shortly mentioned in section 3-1. To shift the system boundary back to a single flexure without the stage, and the input force actually being the interaction force between the flexure and the stage (thus different form the input force from the race coil actuator), the mass at the tip of the flexure can be removed. For identification however, this is not done as there is no control over this interaction force, and thus can not be used as input.

For the identification runs, again a sine sweep is presented on the force input when the output position of the stage is measured. By doing this, the four flexure system is thus identified and the full dynamics should show up in the response. A disadvantage of this is the additional dynamics that is captured around the second vibrational mode as can be seen in Figure 5-2b. Here, three different resonance peaks at slightly different locations can be seen where only one resonance peak is expected. This is due to the model only modelling one flexure, and the identification actually measuring the response of all 4. Thus giving rise to redundant vibrational modes where multiple flexures can vibrate in or out of phase with each other. To validate this response actually represents dynamics instead of some erroneous signal, a second independent run for this region is presented as well. This run overlaps the first run almost perfectly showing the actual repeatable dynamics.

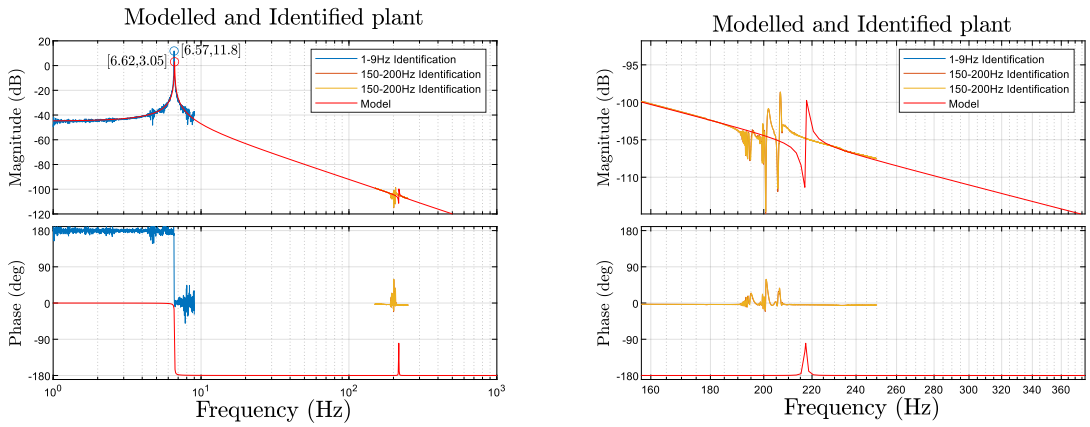

(a) Identified and modelled plant

(b) Second mode close up

Figure 5-2: Modelled versus actual response phase and magnitude plot from force input to position measurement.

Some parameters like the material damping or the actual mass of the stage are hard to determine, these are adjusted until the first resonance peak of the model corresponds to the measured peak. This thus results in somewhat of a manual parameter identification. Here again, it is not necessarily important these values represent the true values, as long as the model response corresponds to the system response. This is an important distinction as this can make these parameters embody different modelling errors in order to obtain a better model and system accordance, thereby losing some physical interpretation. For the filters however, only the model and system accordance is of importance as physical interpretation

does not matter. As mentioned in section 3-1, the relation between the control input and the actual force is assumed linear with a matching gain. This gain is also adjusted in order to obtain model and system correspondence. The final modal damping coefficient, assumed stage mass for a single flexure and matching gain are summarised in Table 5-2.

ζ	0.002	-
Stage mass	100	g
Matching gain	48.6	db

Table 5-2: Tuned parameters for the final model

As can be seen in Figure 5-2a, the first resonance mode nicely overlaps with the expected dynamics after this tuning, and the second even though slightly shifted can also be found in somewhat the same location and amplitude. It is therefore assumed the model obtained in section 3-1 models the relevant dynamics sufficiently well for any discrepancies to be regarded as modelling errors and will not be further addressed here.

5-3 Filtering

After the construction and assembly of all components as described in the previous section, data can actually be obtained and the relevant filters implemented. This section shortly introduces the implementation of the filters presented in Chapter 3. Since the offline implementation of these filters is rather straightforward, this will not be discussed in detail. The main focus will be put on the process of tuning and initialisation as this can significantly impact the filter's performance.

For all filters, the model introduced in section 3-1 is used. Here, the acceleration measurement of the tip location is used in combination with the strain measurement from the strain gauges. All filters are allowed to use only these two signals for estimation. The position measurement at the tip is not used for estimation, but only for validation.

5-3-1 Initialisation

Since all filters have internal dynamics, their states $\bar{q}$ need to be initialised together with their covariance matrices P. Since it is not possible to hold the stage stationary due to a lot of external vibrations, no zero initial state can be achieved. In addition, remnant internal stresses in the stage flexures might also shift the true initial state even when zero strain is expected. Because of this, it is assumed no information is available on the initial state, and all states $\bar{q}_0$ are initialised on zero. Due to the converging properties of the filters, they should converge to a value relatively close to the true state within a short period of time.

For the initial covariance matrices P_0, also no information is available on the relative covariance of all initial state estimates. Therefore, all initial covariance matrices are initialised as $P_0 = p_{\text{init}}\mathcal{I}$ with p_{init} chosen relatively large at 10^3. Observation of the estimated state values during simulation expects a maximum value around 10^{-5} for the first state for the training data set, which confirms an initial covariance of 10^3 is fairly large. This reflects the lack of knowledge and confidence in the initial state guess, and should reduce as the estimate becomes more certain.

5-3-2 Tuning

For the filter tuning, a training data set is selected where the stage is in closed loop control following a set trajectory. Since no information about the true states of the system is available, the position measurement at the tip of the flexure is used as validation and removed for the filters themselves. The filters thus only use the strain and acceleration measurement for estimation. Through the simulation results presented in Chapter 4, it can be argued however that the tip location estimate does represent the state estimate accuracy, and can thus be used as performance metric.

Since all filters contain an LQ optimal linear estimator of some sort, they all require the tuning of the process and noise covariance matrices Q and R. In addition to this, the AKF and DKF require the tuning of the input covariance Q_u. Full tuning of these matrices would result in a large parameter space which can become tedious and very non-intuitive. To better standardise and reduce complexity of the tuning process, the parameter space is reduced. This is done by measuring noise covariance characteristics for all sensors as presented in Appendix B. These covariances are repeated here in Table 5-3.

cov_{acc}	0.0587	m^2/s^4
$\text{cov}_{\text{strain}}$	$1.095 \cdot 10^{-16}$	m^2/m^2

Table 5-3: Measured sensor noise characteristics

These values are a decent initial guess as they should approximate the relative covariances between the measurements quite well resulting in an initial R matrix

$$R_{\text{init}} = \begin{bmatrix} \text{cov}_{\text{acc}} & 0 \\ 0 & \text{cov}_{\text{strain}} \end{bmatrix}. \tag{5-1}$$

The process covariance matrix Q is initially chosen as $Q_{\text{init}} = \mathcal{I}$ of appropriate size since no information is available on the relative accuracy of the different states.

To capture the relative importance of the time update versus the measurement update and reduce the parameter space, both matrices are multiplied by scalar q_{tune} and r_{tune} such that $Q = q_{\text{tune}} Q_{\text{init}}$ and $R = r_{\text{tune}} R_{\text{init}}$. Only varying these scalars thus reduces the problem to two tuning parameters.

The last important tuning parameter for the AKF and DKF is the input covariance matrix Q_u as introduced in subsection 3-2-2 and subsection 3-2-3. The GDF does not assume a random walk process for the input, and thus does not require this input covariance to be tuned. Since only one input is defined in the model, the input covariance reduces down to a scalar, which results in the third tuning parameter.

For the actual tuning, the earlier introduced tip position is used as reference from which a fit score can be obtained in the form of a Normalised Root-Mean-Squared Error (NRMSE) between the estimated tip location and the reference. The first two parameters (q_{tune} and r_{tune}) are then empirically tuned to obtain an initial guess, which is input into a Nelder-Mead simplex algorithm for further fine-tuning. The resulting convergence plots can be seen in Figure 5-3a, Figure 5-3b and Figure 5-3c for the AKF, DKF and GDF respectively.

The third tuning parameter (the input covariance Q_u) is subsequently tuned using an L-curve regularisation technique, where the previously introduced fit score is plotted for a wide range

of values. The L-curve for the AKF and DKF are also presented in Figure 5-3d where a sharp drop in fit score can be observed whereafter no real improvement is made. The input covariance is thus chosen shortly after this sharp decline.

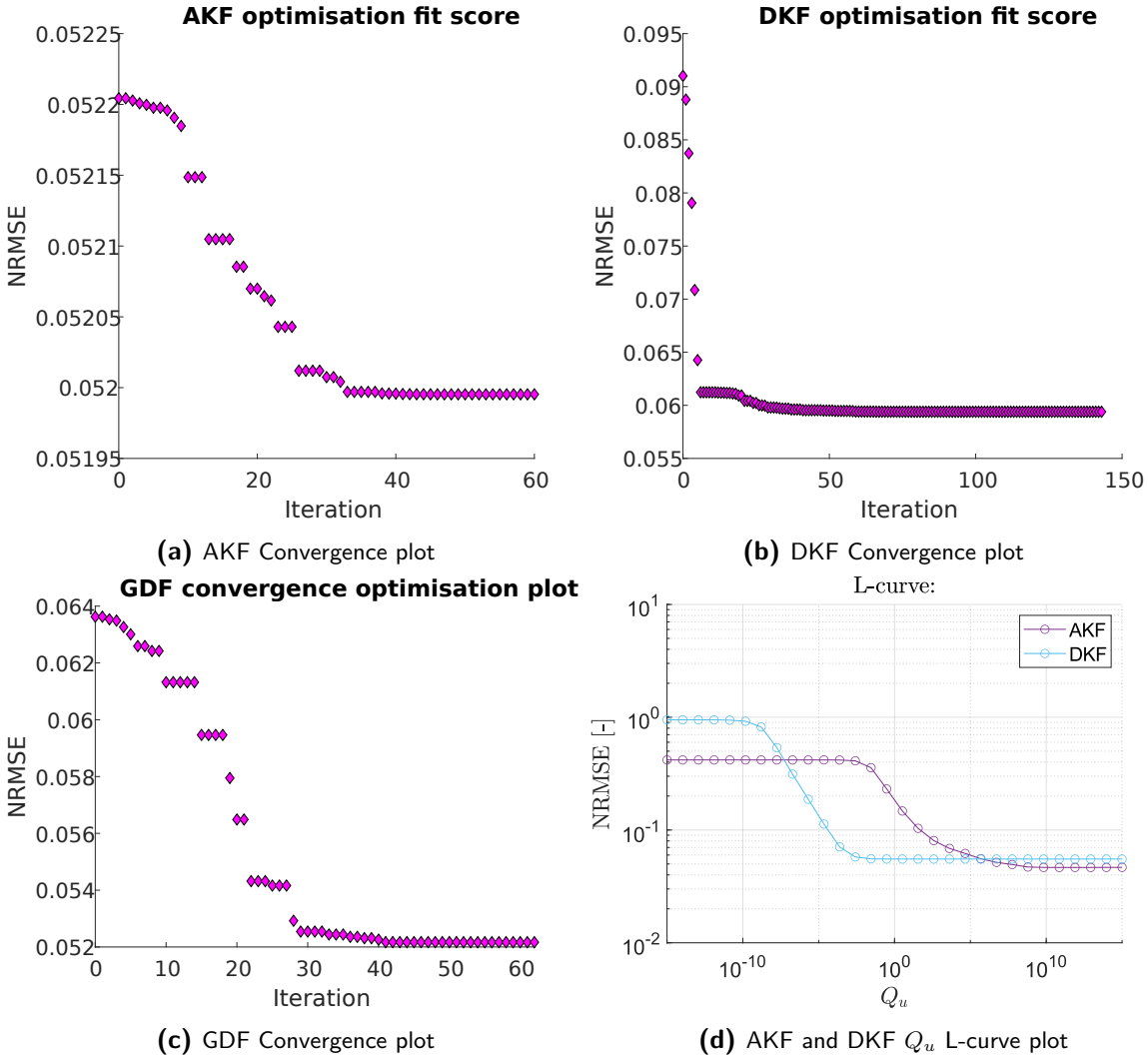

(a) AKF Convergence plot

(b) DKF Convergence plot

(c) GDF Convergence plot

(d) AKF and DKF Q_u L-curve plot

Figure 5-3: Tuning process results for the AKF, DKF and GDF

Since the input value of the chosen input covariance matrix has some influence on q_{tune} and r_{tune} the process is iterated some times untill convergence of the parameters is obtained. The final tuning parameters for the filters are presented in Table 5-4.

	AKF	DKF	GDF
q_{tune}	$1.86{\cdot}10^{-9}$	$3.03{\cdot}10^{-13}$	$2.24{\cdot}10^{-5}$
r_{tune}	$2.26{\cdot}10^{4}$	$1.11{\cdot}10^{4}$	$2.29{\cdot}10^{14}$
Q_u	$1{\cdot}10^{10}$	$1 \cdot 10^{1}$	-

Table 5-4: Tuned filter parameters

It is important to note this way of tuning is still sensitive to local minima. It is therefore

not guaranteed the performance obtained is the best performance possible, and therefore only locally optimal. Figure 5-3 does however show all filters converge to a local minimum. After many tuning attempts, covering a wide range of the parameter space using grid searches, these parameters were however selected as best performing and most stable.

Another issue with this approach is over-fitting on the tuning data. It is however argued that only the relative performance between the filters is of significant importance given the research question to be answered. Since all filters are tuned in a similar manner, and all optimised using the same algorithms and on the same data sets, their absolute performance is of less importance. Their performance can still be compared, making over-fitting less of a problem. ch:Results also shows that over-fitting is not actually a problem since performance seems consistent over other data sets after training.

5-4 Design of Experiments

To properly evaluate performance of these filters to answer the proposed research question:

"**Which of the selected existing Bayesian simultaneous input and state estimation techniques is most viable for implementation on high precision compliant motion stage flexures?**",

performance criteria need to be set up on which these filters can be evaluated. These can be evaluated for all filters separately, which allows for a fair comparison. For these performance criteria, data sets are then be gathered which will be used for final evaluation. The two main interesting filter aspects that are evaluated are Sensor dependency and overall fit score.

- **Sensor dependency**
  The first performance metric of these filters that will be investigated is sensor dependency. During setup, simulation and tuning, it has been noticed different filters require different types of measurements. While the AKF is consistent all configurations, the DKF and GDF rely heavily on the direct feedthrough term in the system model as can be seen in the K^f matrix for the DKF in Eq. 3-35 and M for the GDF in Eq. 3-36. These matrices are both fundamental for the input estimate, and could thus influence performance significantly. Using the methods as described in section 3-1, it is shown that this direct feedthrough term is only nonzero for the acceleration measurement as can be seen in Eq. 3-19. Non sufficient excitation of the acceleration measurement could thus reduce filter accuracy which could lead to specific accuracies for different operating ranges (depending on the acceleration measured). In high-tech systems like precision motion stages, it is not always possible to obtain proper acceleration measurements. Investigating filter dependency on this measurement is thus of importance for the implementation on systems like this.

  To evaluate this, the first two data sets gathered employ closed loop control to obtain relatively high accelerations for a short period of time, and reduce accelerations by allowing the stage to dampen out in open loop later on. Therefore containing relatively exciting and less exciting acceleration regions. For the first closed loop section, a block signal is used as reference, whereas the second closed loop experiment requires the tracking of a 10Hz sine wave. For completeness, these data sets are appended in Appendix C where these first two are presented in subsection C-2-1 and subsection C-2-2.

- **Overall fit score**
  Since the overall performance of the filters is regarded as the most important performance metric. The fit score of the estimated and measured tip location is evaluated. To be able to evaluate different operating ranges, the two data sets introduced for sensor dependency are used in addition to two new sets. In these new sets, the stage is excited by an impulse in open loop whereafter it is allowed to dampen out. Evaluating an impulse response should allow for the evaluation response time and input estimation. In addition, the combination with the first two data sets should evaluate the filters on sufficient operating conditions to draw conclusions about their performance.

Chapter 6

Results

In this chapter, the main results for the implemented filters are presented. To do so, they are sub-divided based on the performance criteria proposed in section 5-4. In section 6-1, the results and figures for sensor dependency are presented and elaborated on whereafter section 6-2 presents the resulting overall fit scores for the filters on all data sets. For reference, all signals for these data sets are appended in Appendix C.

It is important to recall here that all filters are allowed to use only the tip acceleration measurement and strain gauge measurement for estimation. The position measurement at the tip is not used for estimation, but only for validation.

In addition to the tip location, all filters also provide an estimate on the input force on the system. Since this is chosen to be the interaction force between the stage and the flexure as presented in section 3-1, there is no way to verify performance on this as the true signal is not known. It is however argued that an input estimate is not of importance to this work as the state estimate is only of interest. Input estimation performance is thus only presented shortly.

The filter performance with respect to the actual state reconstruction can also not be evaluated directly. For this however section 4-2 presents a link between the tip location estimate and the state estimate. Through this link in simulation, it is assumed the tip location estimate also represents the state reconstruction performance of the filters, which can thus be evaluated indirectly.

6-1 Sensor dependency

To evaluate sensor dependency, the filters are evaluated over the first two data sets. Each data set is sub-divided into two non-control regions and one closed loop control region. For each region, the mean absolute acceleration signal is computed. The mean absolute error of the filter's tip location estimation compared to the true tip location is also computed for all three sections, for every filter. This is done for both data sets and presented in subsection 6-1-1 and subsection 6-1-2. It must be noted that taking the mean absolute value is noise sensitive

since absolute noise is additive. It is however assumed noise is constant over both data sets since they are recorded within a short period of time, and thus does not influence a relative evaluation.

6-1-1 First data set

The results for the first data set are presented in Figure 6-1. Here, the three selected sections are separated by the red dashed lines for which the mean absolute acceleration signal and error values can be computed. The results for these sections separately are also presented in Figure 6-2 where the mean absolute filter error is graphed together with an error bar of one standard deviation. The mean absolute acceleration value is also shown on the second y axis.

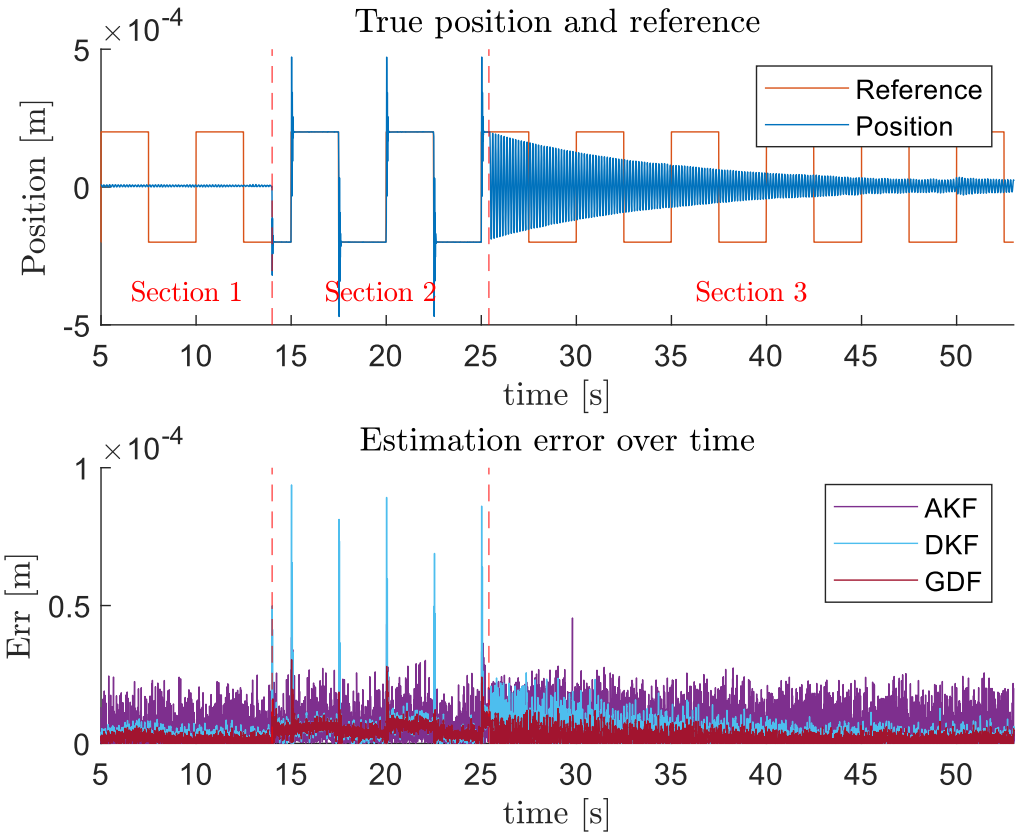

Figure 6-1: Absolute estimation error values and true position for the first data set.

When looking at Figure 6-2, it can be seen the average absolute acceleration measurement is relatively low for sections 1 and 3, and high for section 2 as expected. For the mean average filter error values, it is clear to see they all follow similar patterns to the acceleration measurement where the first and last sections have comparable errors, and a higher error is observed in the second section (the controlled section).

This observation is also supported by Figure 6-1, where the trend sketched by Figure 6-2 can also be seen. It is however noted the mean absolute filter error metric used in Figure 6-2 does

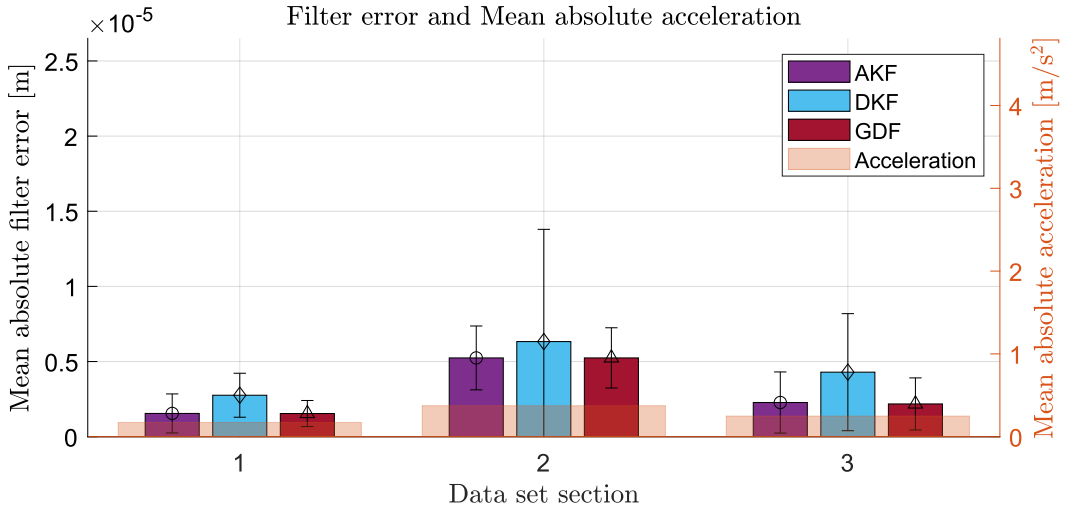

Figure 6-2: Mean absolute acceleration measurement and filter error values for the first data set with one standard deviation error bar.

not completely capture the source of error of these filters, for which the error bars provide some more insight. Here, it can be seen the GDF and AKF differ only in the absolute filter error standard deviation showing larger noise transmission of the AKF compared to the GDF.

To obtain more data however, the second data set is also presented in subsection 6-1-2.

6-1-2 Second data set

For this set, the same procedure is followed as the set presented before. In the closed loop control section however, the reference signal is altered to a 10Hz Sine wave. The resulting position and absolute error plot is presented in Figure 6-3. This set is also sub-divided into three sections labeled in the figure. The resulting mean absolute acceleration and mean absolute error values are subsequently presented in Figure 6-4.

Here again, a relation between acceleration signal and filter error can be perceived similar to the results obtained for the first data set in subsection C-2-1. To be able to evaluate any correlation between acceleration signal and filter error however, the Pearson correlation coefficient can be calculated. To provide some visual reference for this, the mean absolute filter errors for every section of both the first and second data sets are plotted against its mean absolute acceleration value in Figure 6-5 whereafter the Pearson correlation coefficients are presented in Table 6-1.

	Correlation Coefficient
AKF	0.8676
DKF	0.9927
GDF	0.8758

Table 6-1: Correlation coefficients between mean absolute acceleration and mean absolute filter error. Here, 2 data sets are sub-divided into 6 regions for which the mean absolute values are calculated resulting in 6 data points for each filter from which the correlation coefficient is evaluated.

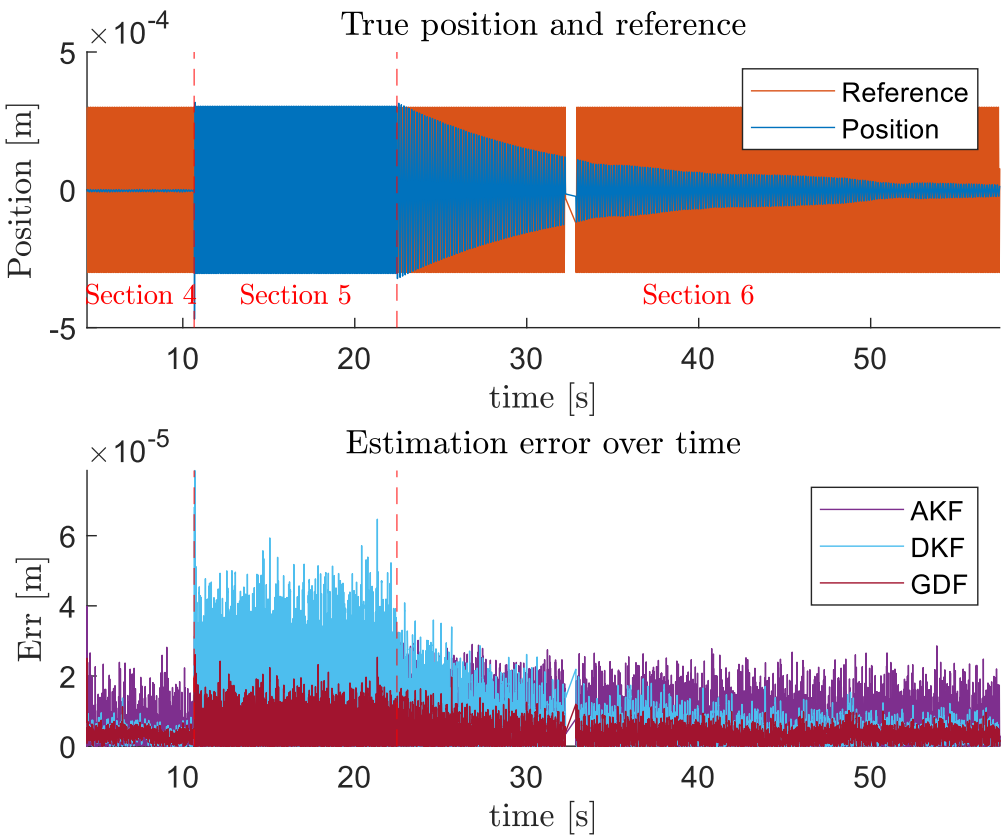

Figure 6-3: Absolute estimation error values and true position for the second data set.

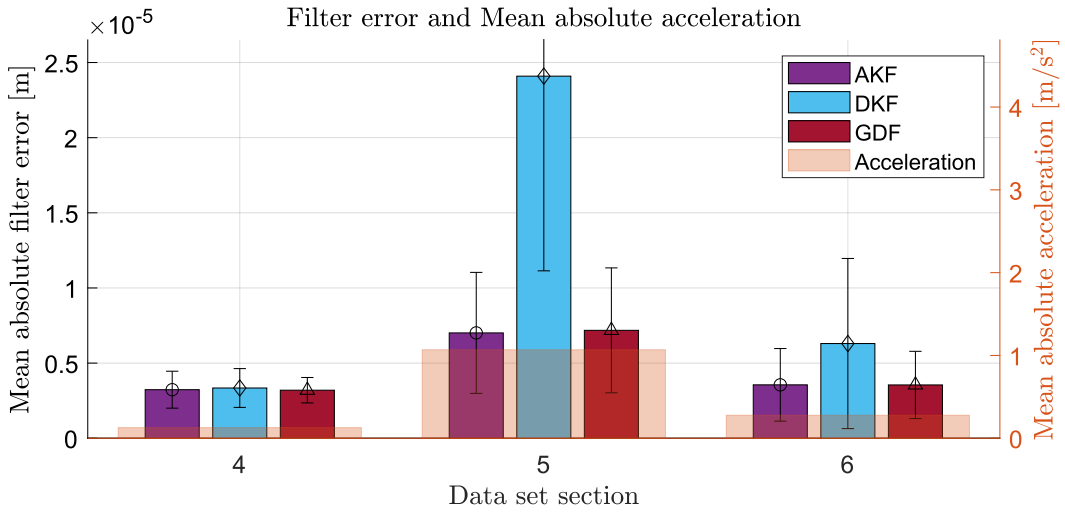

Figure 6-4: Mean absolute acceleration measurement and filter error values for data set 2.

Here, it can be seen that a strong positive correlation is present between the filter error and acceleration value. It is argued that this is due to the speed of the system, which increases with

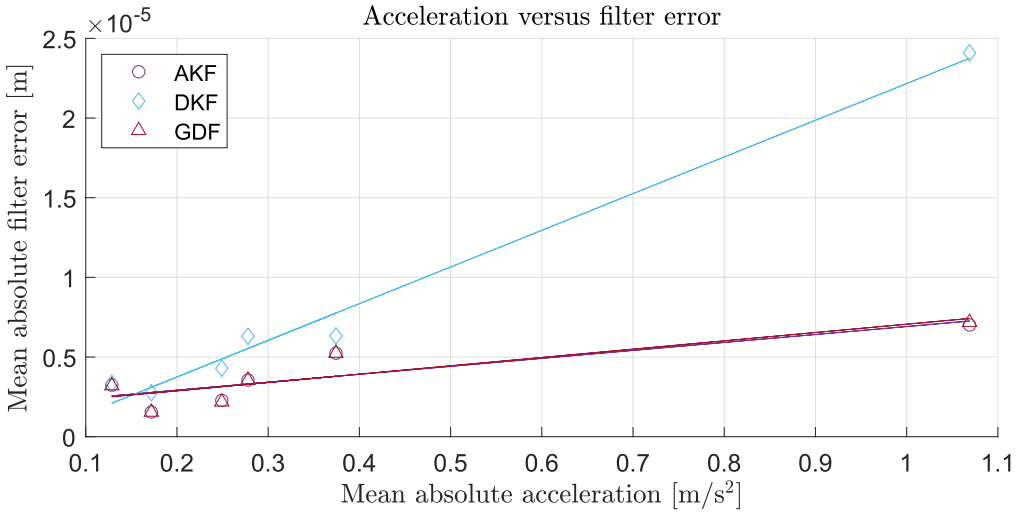

Figure 6-5: Mean absolute acceleration value versus mean absolute filter error for 6 data-set sections.

increasing acceleration, requiring a faster filter to maintain a constant error. This positive correlation could thus be attributed to the inherent finite pole locations of these filters. What is not represented however, is a negative correlation due to increasing acceleration signal as was expected. Since direct feedthrough dependency is only present in the DKF and GDF filters, if this effect would be present, they should behave in similar manner with decreased correlation coefficients compared to the AKF. Even though only careful conclusions can be drawn from this data, it can not be said these filters show similar negative correlations.

A careful observation that could be made is the fact that the DKF decreases performance significantly with increased acceleration. This can be seen from the relatively large correlation coefficient compared to the AKF and GDF in Table 6-1. Decreasing performance with increasing acceleration could thus limit the DKF applicability on high-speed, high-acceleration systems such as precision motion stages. This is a significant result for the evaluation of these RBFs from SHM into high-tech compliant motion stages.

6-2 Overall fit score

Since state estimation is the primary objective of these filters, they also need to be evaluated on fit performance. Here again, the estimated tip location is compared to the stage measurement for all 4 data sets. The complete data sets can be found in Appendix C. As a reminder however, the first data set employs closed loop control using a block reference signal. The second attempts to follow a 10Hz sine wave. The third and fourth data sets apply a 100% control effort impulse at 10s whereafter the stage is allowed to dampen out.

In addition to the tip position estimate, the input estimate is also evaluated shortly in subsection 6-2-1. Even though this is not significant for state reconstruction, an accurate input estimate could also provide useful information which is why it is still evaluated here.

6-2-1 Tip position estimate

For illustrative purposes, Figure 6-6 presents some interesting sections of the 4 data sets introduced before where the left side presents an overview of selected regions, with the green-dashed section presented on the right. Here, the filter's estimate is also plotted.

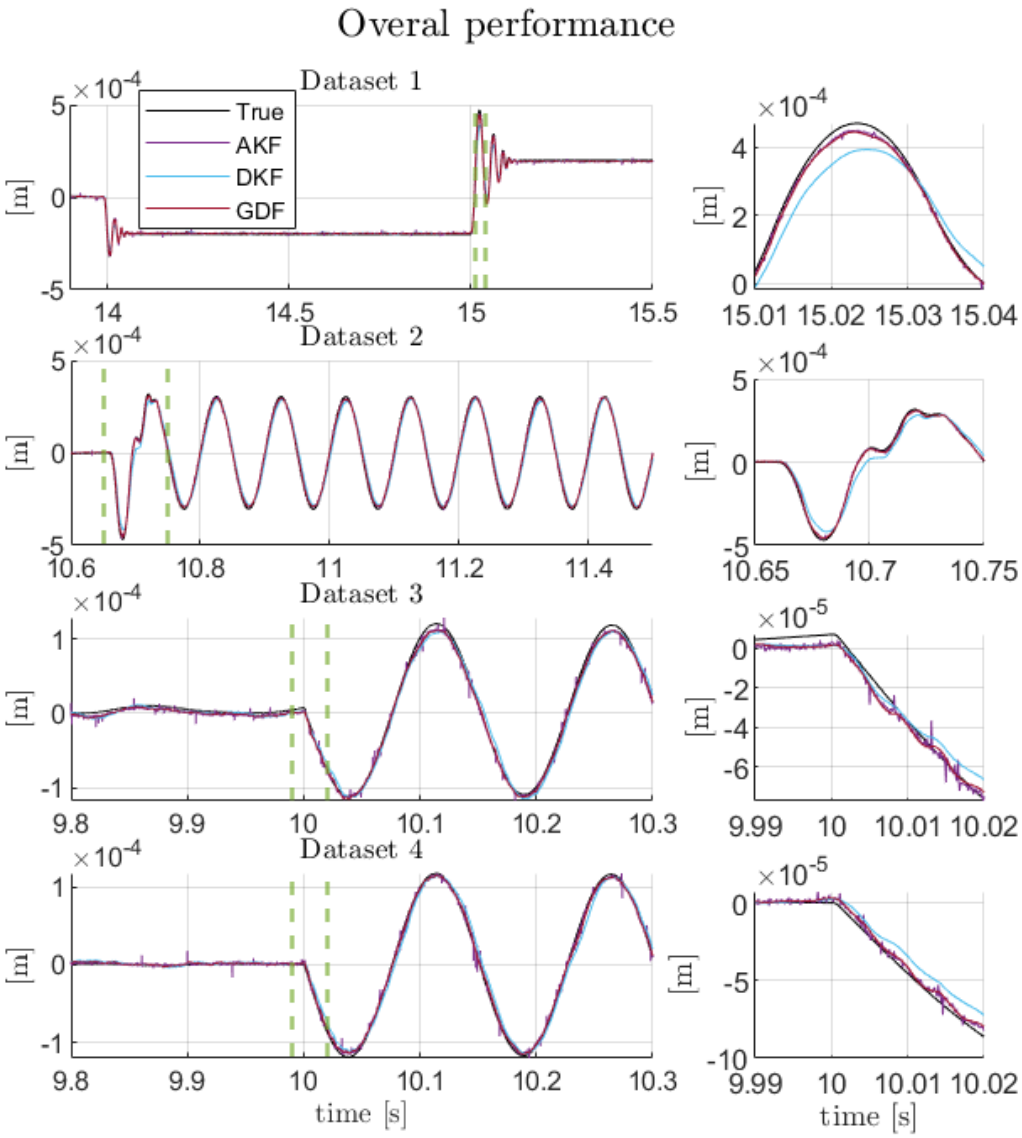

Figure 6-6: Overall filter response plotted for interesting sections of the data sets. The right figures provide zoomed in results of the green-dashed sections in the left figure.

As can be seen in this figure on all data sets, the DKF clearly and structurally under estimates the tip position. This is also represented in the fit scores on all datasets which is shown in Figure 6-7. Here, the DKF has the highest NRMSE for all data sets.

A second and clear observation has to do with the AKF, which seems to pass through signif-

icant amounts of noise compared to the other two filters. This noise propagation can also be seen in the state estimate which is not plotted here. It is however clear the AKF does agree with the GDF quite well, even though the additional noise on the estimate deteriorates performance slightly. This behaviour is consistent with the simulations in section 4-2 suggesting this is not due to the noise realisation.

The GDF seems to agree with the AKF, and not build up a systematic under-estimation while also providing a low-noise estimate.

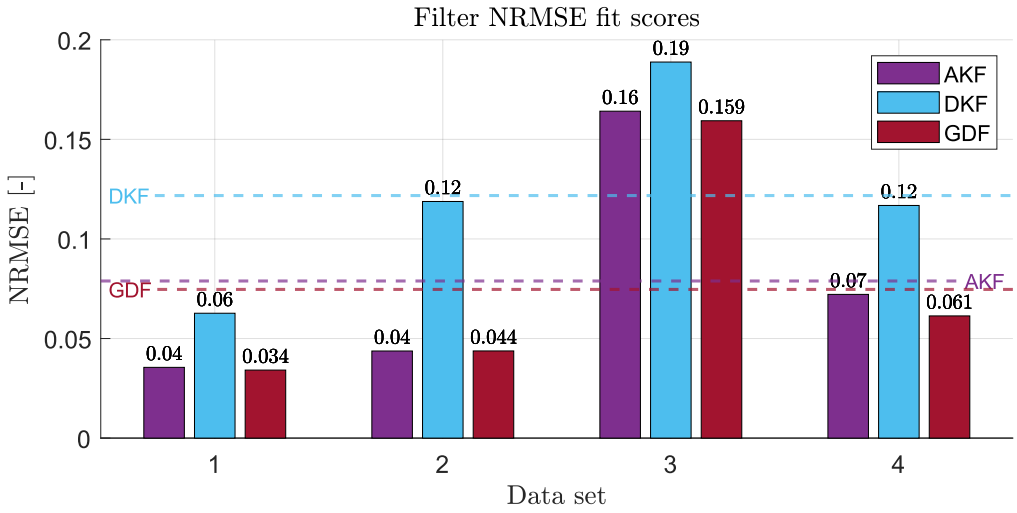

Figure 6-7: NRMSE fit scores for three input and state estimation algorithms on 4 independent data sets. Horizontal dashed lines represent the average performance over all 4 data sets.

A last important note to be made here is the bias developed for the third data set as can clearly be seen in Figure 6-6. This steady state error persists throughout the data set, and is not present in the fourth. The third and fourth data set both use the same input sequence, and record the same signals. This could however be explained by looking at the full data sets in Appendix C. Here, it can be seen data set 3 is initiated with slightly higher remnant vibrations. This could cause the position measurement to be initiated at a position slightly off of 0 since this is a relative measurement thus introducing a bias in the position measurement which can also be observed when actually evaluating the full position measurement for the third data set. Here, the oscillations do not center around 0. It is thus argued this bias is not an estimation error, but rather an initialisation error of the validation signal in the data set.

6-2-2 Input estimation

For the input estimation, no true value is known since the input is an interaction force between the stage and the flexure. It is however interesting to still present the filter's resulting estimate as this could provide useful information about the disturbance force the flexure is exerting on the stage. The estimation results for the third and fourth dataset are presented in Figure 6-8, as these are the most intuitive.

As can be seen, the estimated input force varies on the orders of tens of mili newtons, which could be feasable. The most interesting observation that can be made is the filter's agreement on the main resonance frequency which is followed by all three similarly. The second resonance

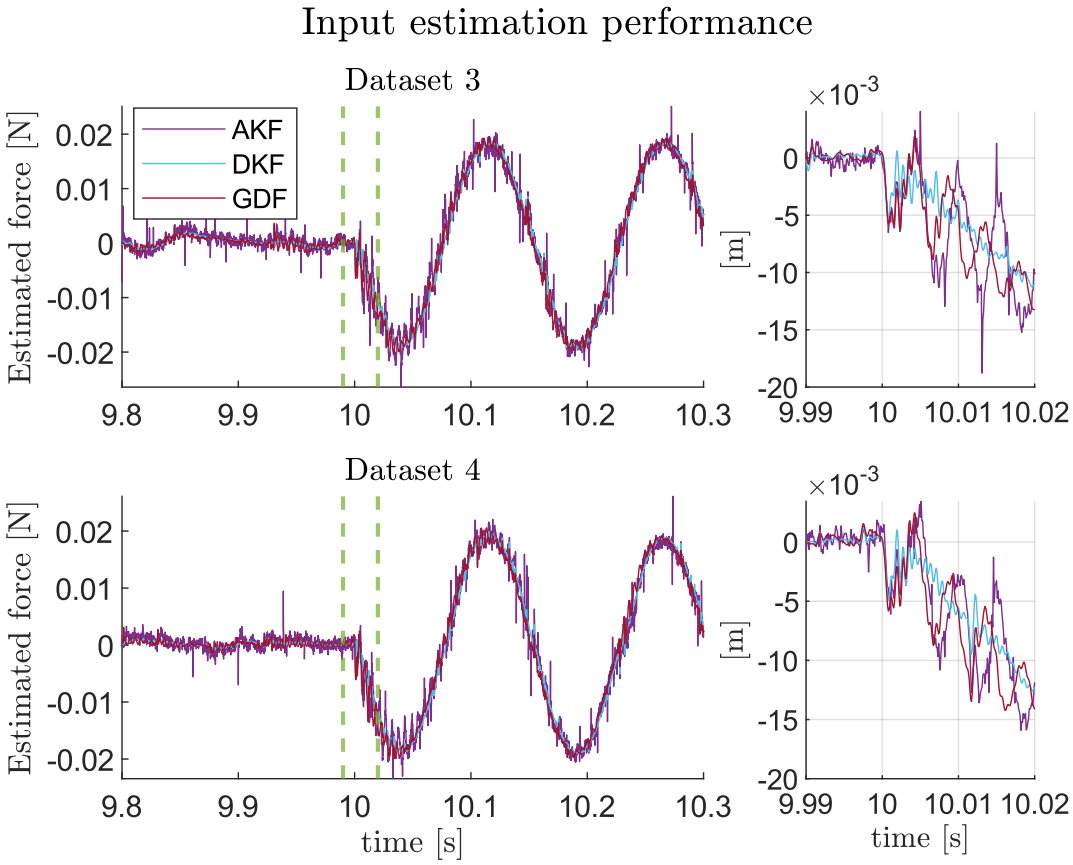

Figure 6-8: Resulting estimated input force f

frequency however as can be seen in the right figure causes some disagreement, which could indicate different second state estimates. This can also be seen in simulation in Figure 4-1. Important to note however is the fact that this input estimate is not necessarily of importance to the current work, as only the state estimate is required.

Chapter 7

Discussion

After evaluating the results in the previous chapter, limited conclusions can actually be drawn. This is due to some limitations in the filter implementation and the validation process. Before evaluating the results, these are presented to be able to keep in mind for the conclusions.

- **Filter implementation**
  One problem with the filter implementation and modelling is off course filter tuning. The filter's performance is only as good as it's tuning, and it can not be guaranteed a global optimum is reached. This weakens any conclusion made about the filter performance since there could be a set of tuning parameters that makes the filter behave differently. Comparisons between filters are also undermined since one filter could be tuned worse than the others. In this work, an attempt to addressed this problem is made through an extensive tuning procedure and subsequent optimisation. Hereby reducing the leverage this tuning fallacy has on the results to what can reasonably be expected from this work. This is however also a fundamental problem to any work that implements these types of filters, and can not be solved completely.
- **Validation process**
  One significant limitation of the approach taken for validation in this work however is the validation process as used to evaluate the filter performance in Chapter 6. Here, most results are drawn from a comparison between the estimated and the measured tip location. This however introduces an 'unfair' advantage for the filters since they have a collocated acceleration measurement available. The tip location is thus likely to be estimated most accurately and could result in slightly biased results. Addressing this would require an additional position measurement at a different location along the beam, preferably at a large displacement location for the second mode, and comparing measurement with estimation there. This would take away the collocation advantage, and evaluate the filter's state reconstruction much better since this response would be dominated by the second vibrational mode. Due to time limitations however, this is not implemented in this work. Instead, a link was presented between the state estimate and the tip location estimate through simulation in section 4-2 to patch this shortcoming slightly. Nevertheless, this validation fallacy does limit validity of the results and has

to be taken into account.

These problems both lay at the foundation of this work, and do limit the conclusion's validity. It is however still possible to evaluate the results obtained in the previous section, keeping earlier established limitations in mind.

For this, the two performance criteria can be evaluated using the results presented in Chapter 6. Since the research question to be answered only requires a qualitative comparison between the filters, the performance criteria are not weighted and scored, but merely discussed.

For the first performance criterion, the results as presented in section 6-1 did not show a clear negative correlation between mean absolute acceleration measurement and filter performance. This could thus indicate the filters are not influenced by the absolute signal values as was suggested by the large dependence on direct feedthrough for the DKF and GDF. It is however noted here that there are only 6 points computed from 2 data sets used to evaluate this. More data containing more significantly different levels of acceleration could thus improve the analysis, and strengthen this result. The observation made from Figure 6-5 that the DKF performs relatively poorly with increased system acceleration also suffers from this small number of data points. Nevertheless, this result is still assumed valid for the purposes of this work thus resulting in the conclusion that the AKF and GDF behave similarly with increased acceleration, and the DKF relatively poorly.

The second criterion is the overall fit score. Here, the validation fallacy introduced before needs to be taken into account when evaluating absolute filter performance. For relative performance however, this is of less importance since all filters are effected in a similar manner. The results presented in Figure 6-7 can thus be used for relative filter evaluation. Doing this, it is observed the GDF and AKF perform similarly with the GDF having a slightly better fit score over all data sets. The DKF performs poorly overall by systematically under estimating the actual tip location. This could be due to slow filter response where high frequency dynamics are not captured thus introducing steady state error. When comparing the AKF and GDF however, Figure 6-6 introduces a big advantage of the GDF over the AKF, which is the lack of noise transmission. This also matches with the earlier established simulation results in Figure 4-1 and gives the GDF the upper hand in overall estimation.

As for the input estimation, no conclusions can be drawn about performance since the true value is unknown. It is however again noteworthy the GDF provides a low noise estimate, whereas the AKF again transmits noise into this estimate. The observation that the AKF and DKF do seem to agree in general does suggest they both estimate something close to the truth. This can however not be substantiated further due to lack of validation.

Chapter 8

Conclusions & Recommendations

8-1 Conclusions

In this work, the research question to be answered is repeated as:

"**Which of the selected existing Bayesian simultaneous input and state estimation techniques is most viable for implementation on high precision compliant motion stage flexures?**".

This is done by completing the intermediate objectives as introduced in section 1-3, and actually implementing three existing Bayesian simultaneous input and state estimation techniques on a real compliant motion stage flexure, and evaluating the filters off-line.

The resulting filter performance is determined based on the estimation accuracy of the tip location and filter response for higher acceleration scenario's. Important to mention again is the assumption that the tip location estimate performance is assumed proportional to the state estimation performance as proposed in simulations in section 4-2.

For both the estimation accuracy of the tip location and filter response to higher acceleration scenario's, a clear order in filter performance is observed where the DKF performs poorly and the AKF and GDF similarly well. The AKF however transmits significant amounts of noise into its estimate whereas the GDF does not, which puts the GDF on top.

The conclusion to the posed research question can thus be drawn as the filter proposed by S. Gillijns and B.De Moor (The GDF), which performed consistently better then the AKF and DKF on this system configuration. It is noted this does not necessarily coincide with literature results like [11; 12] [16]. These works however evaluate performance based on acceleration-only measurements for SHM. The addition of a strain measurement provides a significantly different operational environment.

To solidify this conclusion however, more research is required which will be elaborated on in the next section.

8-2 Recommendations

Since no research is ever complete, recommendations are made for further look in this section. To do this, recommendations are sub-divided into improvement of the current work, extension of the current work, and future research steps.

8-2-1 Improvement of current work

To improve on the results in the current work, it is off course paramount to gather more data as well as more specific data sets. Here, a more extensive Design of Experiments could yield more specific input sequences and scenario's better for evaluating specific filter aspects. Different levels of acceleration could for instance be achieved by evaluating closed loop control on different frequency sinusoidal signals severely strengthening the results for the sensor and system speed dependency section.

The same could be done for the tip location estimation data sets, where an input sequence exciting mainly the second vibrational mode could yield better performance evaluation of these filters.

Another improvement that off course has to be mentioned is filter tuning, which could also always use more time. Even more fine-meshed grid searches and longer and more exciting training data sets could yield a better filter configuration, or improve tuning for a specific filter, therefore making for an even more fair comparison.

8-2-2 Extension of current work

Instead of improving the current work, the evaluation of these filters for input and state estimation on compliant motion stages could be extended. The first and foremost extension that can be made here is more involved evaluation by an additional position measurement somewhere along the beam. This would allow for the validation of the estimate of the second state estimate, and severely improve conclusions drawn about state estimation performance of these filters.

The same could be done for input estimation, where a system to evaluate the true input force would allow for evaluation of input estimation performance. A system like this could incorporate a load cell in the stage design, which would not necessarily change the filter design, or implementation as this is outside the system boundary. This would however allow for the measurement of an interaction force possibly yielding interesting conclusions about the input estimate to be able to use this in position control for the stage as a known disturbance.

The main extension of this work would however be the implementation of these filters in real-time, to be able to evaluate real-time performance and computational burden. Steps have been made in the code in [22] for this implementation in Simulink. Due to time constraints however, this is not completed yet but would be very interesting to implement.

8-2-3 Future research steps

For a future research step, not necessarily extending the current work, it is clear actually implementing these filters together with control and actuation into a full Active Vibration Control structure would be very interesting. This could be done for compliant motion stages,

or any other flexible system that requires active vibration control since the math is the same. This would however require extending the current work into real-time and designing, evaluating, and comparing proper control algorithms like LQR, IMSC or even PID. Following the relatively positive results in this work however, this would be an interesting next step in research.

Bibliography

[1] C. D. Johnson, "Design of Passive Damping Systems," *Journal of Vibration and Acoustics*, vol. 117, no. B, pp. 171–176, 6 1995. [Online]. Available: https://asmedigitalcollection.asme.org/vibrationacoustics/article/117/B/171/439026/Design-of-Passive-Damping-Systems

[2] C. M. Casado, I. M. Díaz, J. De Sebastián, A. V. Poncela, and A. Lorenzana, "Implementation of passive and active vibration control on an in-service footbridge," *Structural Control and Health Monitoring*, vol. 20, no. 1, pp. 70–87, 1 2013. [Online]. Available: https://onlinelibrary.wiley.com/doi/full/10.1002/stc.471https://onlinelibrary.wiley.com/doi/abs/10.1002/stc.471https://onlinelibrary.wiley.com/doi/10.1002/stc.471

[3] M. Pusch, J. Theis, and D. Ossmann, "Partial pole placement using static output feedback," *IFAC-PapersOnLine*, vol. 53, no. 2, pp. 4527–4533, 2020. [Online]. Available: https://doi.org/10.1016/j.ifacol.2020.12.470

[4] M. Pusch, "Aeroelastic mode control using H2-optimal blends for inputs and outputs," *AIAA Guidance, Navigation, and Control Conference, 2018*, no. 210039, 2018.

[5] ——, "Blending of Inputs and Outputs for Modal Control of Aeroelastic Systems," 2020.

[6] J. L. Fanson and T. K. Caughey, "Positive Position Feedback Control for Large Space Structures," Tech. Rep. 4, 1990.

[7] M. J. Balas, "Direct Velocity Feedback Control of Large Space Structures," *J. Guidance and Control*, vol. 2, no. 3, pp. 252–253, 1979.

[8] A. Preumont, "Vibration Control of Active Structures: An Introduction," 1999. [Online]. Available: https://www.researchgate.net/publication/229058034

[9] L. Meirovitch and H. Baruh, "The implementation of modal filters for control of structures," *Journal of Guidance, Control, and Dynamics*, vol. 8, no. 6, pp. 707–716, 1985.

[10] L. Meirovitch and H. Oz, "COMPUTATIONAL ASPECTS OF THE CONTROL OF LARGE FLEXIBLE STRUCTURES." in *Proceedings of the IEEE Conference on Decision and Control*, vol. 1. IEEE, 1979, pp. 220–229.

[11] K. Tatsis and E. Lourens, "A comparison of two Kalman-type filters for robust extrapolation of offshore wind turbine support structure response," in *Life-Cycle of Engineering Systems: Emphasis on Sustainable Civil Infrastructure - 5th International Symposium on Life-Cycle Engineering, IALCCE 2016*. CRC Press/Balkema, 2017, pp. 209–216.

[12] S. Moradi, S. Eftekhar Azam, and M. Mofid, "On Bayesian active vibration control of structures subjected to moving inertial loads," *Engineering Structures*, vol. 239, no. March, p. 112313, 2021. [Online]. Available: https://doi.org/10.1016/j.engstruct.2021.112313

[13] F. Naets, J. Cuadrado, and W. Desmet, "Stable force identification in structural dynamics using Kalman filtering and dummy-measurements," *Mechanical Systems and Signal Processing*, vol. 50-51, pp. 235–248, 2015. [Online]. Available: http://dx.doi.org/10.1016/j.ymssp.2014.05.042

[14] S. Eftekhar Azam, E. Chatzi, and C. Papadimitriou, "A dual Kalman filter approach for state estimation via output-only acceleration measurements," *Mechanical Systems and Signal Processing*, vol. 60, pp. 866–886, 2015. [Online]. Available: http://dx.doi.org/10.1016/j.ymssp.2015.02.001

[15] F. Naets, J. Croes, and W. Desmet, "An online coupled state/input/parameter estimation approach for structural dynamics," *Computer Methods in Applied Mechanics and Engineering*, vol. 283, pp. 1167–1188, 2015. [Online]. Available: http://dx.doi.org/10.1016/j.cma.2014.08.010

[16] O. Sedehi, C. Papadimitriou, D. Teymouri, and L. S. Katafygiotis, "Sequential Bayesian estimation of state and input in dynamical systems using output-only measurements," *Mechanical Systems and Signal Processing*, vol. 131, pp. 659–688, 2019. [Online]. Available: https://doi.org/10.1016/j.ymssp.2019.06.007

[17] E. Lourens, E. Reynders, G. D. Roeck, G. Degrande, and G. Lombaert, "An augmented Kalman filter for force identification in structural dynamics," *Mechanical Systems and Signal Processing*, vol. 27, pp. 446–460, 2012. [Online]. Available: http://dx.doi.org/10.1016/j.ymssp.2011.09.025

[18] E. Lourens, C. Papadimitriou, S. Gillijns, E. Reynders, G. D. Roeck, and G. Lombaert, "Joint input-response estimation for structural systems based on reduced-order models and vibration data from a limited number of sensors," *Mechanical Systems and Signal Processing*, vol. 29, pp. 310–327, 2012. [Online]. Available: http://dx.doi.org/10.1016/j.ymssp.2012.01.011

[19] R. Cook, D. Malkus, M. Plesha, and R. Witt, *Concepts and Applications of Finite Element Analysis*. Wiley, 2001. [Online]. Available: https://books.google.nl/books?id=b8seAQAAIAAJ

[20] Munnig and R. Schmidt, "The Design of High Performance Mechatronics," Tech. Rep., 2014. [Online]. Available: http://ebookcentral.proquest.com/lib/delft/deta

[21] K. G. Aktas and I. Esen, "State-Space Modeling and Active Vibration Control of Smart Flexible Cantilever Beam with the Use of Finite Element Method," *Engineering, Technology & Applied Science Research*, vol. 10, no. 6, pp. 6549–6556, 2020.

[22] P. de Bruin, "Thesis code." [Online]. Available: https://github.com/Pedebruin/Thesis_

Code

[23] L. Meirovitch and H. Öz, "Digital stochastic control of distributed-parameter systems," *Journal of Optimization Theory and Applications*, vol. 43, no. 2, pp. 307–325, 1984.

[24] R. E. Kalman, "A New Approach to Linear Filtering and Prediction Problems 1," Tech. Rep., 1960. [Online]. Available: http://fluidsengineering.asmedigitalcollection.asme.org/

[25] ——, "Contributions to the Theory of Optimal Control," Tech. Rep., 1960.

[26] R. Kalman, "Contributions to the theory of time-optimal control," *Journal of the Franklin Institute*, vol. 275, no. 4, pp. 314–344, 1960.

[27] K. J. Astrom and B. Wittenmark, *Computer Controlled Systems: Theory and Design*. Dover Publications Inc., 2012, vol. 23, no. 3.

[28] M. Verhaegen and V. Verdult, *Filtering and System Identification: A Least Squares Approach*. Cambridge University Press, 2007. [Online]. Available: https://books.google.nl/books?id=6Ne76uYOlVwC

[29] F. Gustafsson, *Statistical Sensor Fusion*. Professional Publishing House, 2012. [Online]. Available: https://books.google.nl/books?id=JSsruwAACAAJ

[30] B. Friedland, "Treatment of Bias in Recursive Filtering," 1969.

[31] A. A. Meera and M. Wisse, "Dynamic expectation maximization algorithm for estimation of linear systems with colored noise," *Entropy*, vol. 23, no. 10, 10 2021.

[32] S. E. Azam, E. Chatzi, C. Papadimitriou, and A. Smyth, "Experimental validation of the Kalman-type filters for online and real-time state and input estimation," *JVC/Journal of Vibration and Control*, vol. 23, no. 15, pp. 2494–2519, 2017.

[33] P. K. Kitanidis, "Unbiased minimum-variance linear state estimation," *Automatica*, vol. 23, no. 6, pp. 775–778, 1987.

[34] M. Darouach and M. Zasadzinski, "Unbiased minimum variance estimation for systems with unknown exogenous inputs," *Automatica*, vol. 33, no. 4, pp. 717–719, 1997.

[35] C. S. Hsieh, "Robust two-stage Kalman filters for systems with unknown inputs," *IEEE Transactions on Automatic Control*, vol. 45, no. 12, pp. 2374–2378, 12 2000.

[36] S. Gillijns and B. De Moor, "Unbiased minimum-variance input and state estimation for linear discrete-time systems," *Automatica*, vol. 43, no. 1, pp. 111–116, 2007.

[37] ——, "Unbiased minimum-variance input and state estimation for linear discrete-time systems with direct feedthrough," *Automatica*, vol. 43, no. 5, pp. 934–937, 2007.

[38] K. Maes, A. W. Smyth, G. De Roeck, and G. Lombaert, "Joint input-state estimation in structural dynamics," *Mechanical Systems and Signal Processing*, vol. 70-71, pp. 445–466, 2016. [Online]. Available: http://dx.doi.org/10.1016/j.ymssp.2015.07.025

[39] "Launchxl-f28379d." [Online]. Available: https://www.ti.com/tool/LAUNCHXL-F28379D

Appendix A

Simulation Details

To demonstrate the feasibility of implementing the methods introduced before on high-precision motion stage flexures, a preliminary simulation is set up. The code for this simulation can be found in a GITHUB repository [22] for the interested reader.

This simulation also serves the purpose of linking the estimated tip location to the state estimation accuracy. This is done to be able to draw conclusions about the state estimate without being able to measure the states in the actual setup.

A-1 Simulation setup

The full simulation attempts to simulate a compliant motion flexure with the base fixed, and rotation fixed at the free end. For this, the simulated model is first set up as shown in subsection A-1-1. Hereafter, the filter setup is presented in subsection A-1-2.

A-1-1 Simulation model

In this simulation, the flexure model as derived in section 3-1 is simulated to be able to test the implementation of the filters. For this, a 'true' model is set up in addition to an erroneous model provided for the filters. The setup of the 'true' model is presented in this section.

For the flexure model, the material and geometrical properties presented in Table B-1 are assumed and implemented according to the modelling procedure introduced in section 3-1. The properties coincide with the actual final implemented system.

This beam model is then modally decomposed in its vibrational modes. For the simulated model, the first 2 vibrational modes are taken into account as truncation. These mode shapes are shown in Figure A-1. Here, also the 12 finite elements, the location of the strain gauge, and the locations of the accelerometer are introduced.

For the strain and acceleration measurement, the modelling procedure described in subsection 3-1-2 is used with mechanical properties as described in Table B-3. These properties match the dimensions and material of the finally implemented measurement strain gauges.

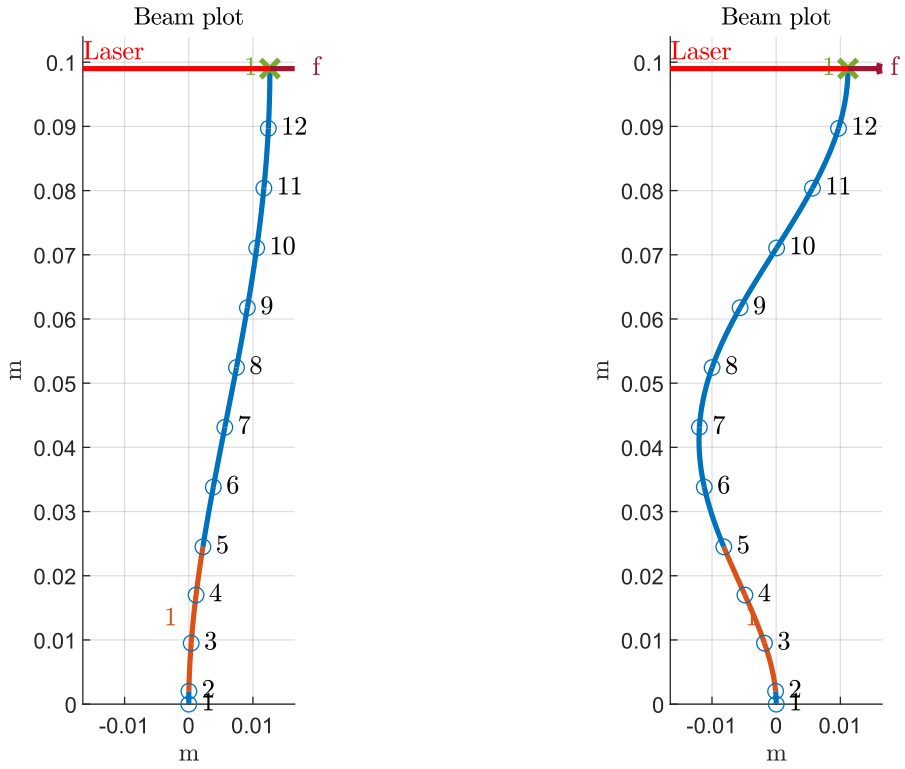

(a) 1st system eigenmode at 52.9 Hz

(b) 2nd system eigenmode at 286 Hz

Figure A-1: Eigenmode plot of the first two eigenmodes. The red patch represents the location and size of the strain gauge, where the green cross represents the location of the accelerometer. The position measurement is done at the laser height, and the input force f is assumed to act here as well.

The system simulation is done using the equations of motion presented in Eq. 3-11 in modal space discretised using the zero order hold assumption with a sampling time of $T_s = 1 \cdot 10^{-4}$s.

This last step results in a system model with a force input at the tip location and outputs for all measurement strain gauges and accelerometers. In addition to this, a reference position measurement is outputted representing a laser position measurement. This is later used as reference for the estimation algorithms.

To model measurement noise $\bar{v}$, a random signal with a Gaussian distribution is added to the output signals of the simulated model, with a pre-specified covariance matrix. This is also done for the process noise $\bar{w}$. The covariance for this noise however is set to 0 for now, as the process noise is modelled in the form of modelling error as introduced in subsection A-1-2. The measurement noise covariance matrices are slected based on real-world noise samples as shown in Appendix B and are summarised in Table 5-3.

A-1-2 Filter setup

Since the filters can not use all information that is simulated, the model that is provided to them only uses the strain and accelerometer outputs similar to the actual implemented setup. In addition to this, the models are altered to incorporate modelling errors. The structural modelling errors are summarised in Table A-1 which are assumed to be worst-case, and thus just statically added to their respective parameters.

Quantity	Amount of error	Unit
Beam density ρ	5	%
Accelerometer mass	5	%
Accelerometer position	1	mm

Table A-1: Model errors introduced

In addition to this model error, also an initial state offset of $1 \cdot 10^{-5}$ is introduced during simulation, since the true initial state is never exactly known.

Using these parameters, the filters and system are simulated. The system response is presented in Figure A-2

Using this model, the AKF, DKF and GDF are set up as introduced in section 5-3. It is worth noting that in the simulation available from [22], also a regular modal filter, a regular luenberger observer and a normal Kalman filter as introduced in can be simulated. These are however not discussed here as they can not be implemented on the actual system.

As for the tuning of the AKF, DKF and GDF, the procedure as described in subsection 5-3-2 coinciding with the actual filter implementation is used to be able to compare results easily. The same tuning parameters and results are used.

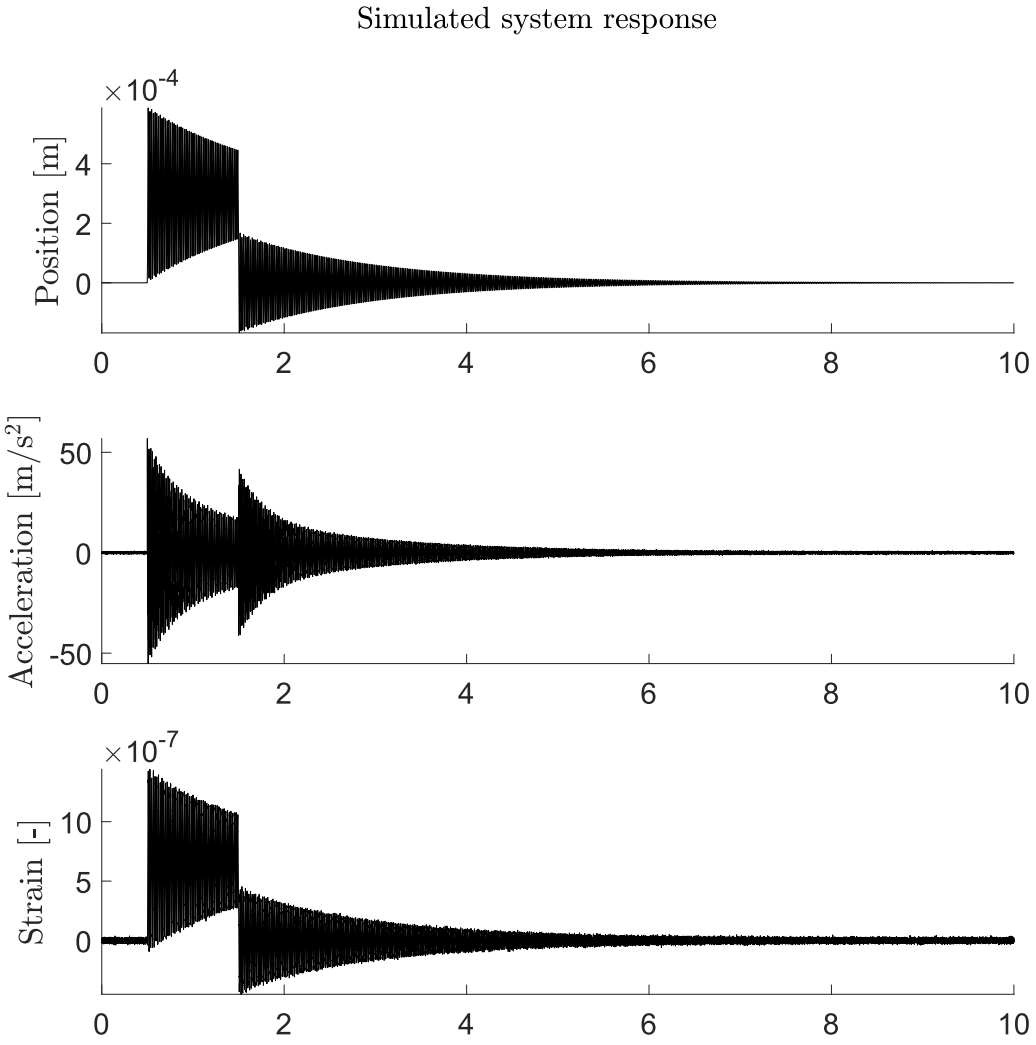

Figure A-2: Full simulated system response

Appendix B

Experimental setup

For the sake of repeatability, this appendix describes the experimental setup used for this work as well as some important design decisions. For this, the selection of the flexures is first elaborated on in section B-1. Hereafter, the race coil actuator is introduced in section B-2. This race coil is used to provide inputs and control effort to the system, and is currently the only way of actuation. To be able to close the loop in position control, and do state estimation, all sensing equipment is introduced in section B-3. For completeness, the micro controller used is described together with its software in section B-4. This completes the description of the physical setup and the software used to operate it.

For convenience, a figure presenting the entirety of the setup is presented in Figure B-1a. The actual final stage setup is also shown in Figure B-1b to be able to reference throughout this section.

B-1 Flexure selection

To show the design evaluations for the stage setup, this section presents the selection process of the current flexure dimensions and material. Thus consequently presenting the selection of the dynamic characteristics of the system. These dynamics are to be chosen relatively freely since the flexures of the stage can be swapped out quite easily. This allows for the choice of width, thickness, length and material of these flexures. To evaluate the influence of these parameters on the dynamics of the stage, the finite element model of a single flexure is used.

Since the goal is to estimate modal amplitudes or states, the observability of these modes needs to be optimised. In addition, physical design constraints need to be taken into account like maximum sampling frequency and nonlinear effects due to the weight of the stage on the flexures. To systematically consider the flexure design, the material is first determined whereafter the physical dimensions are considered.

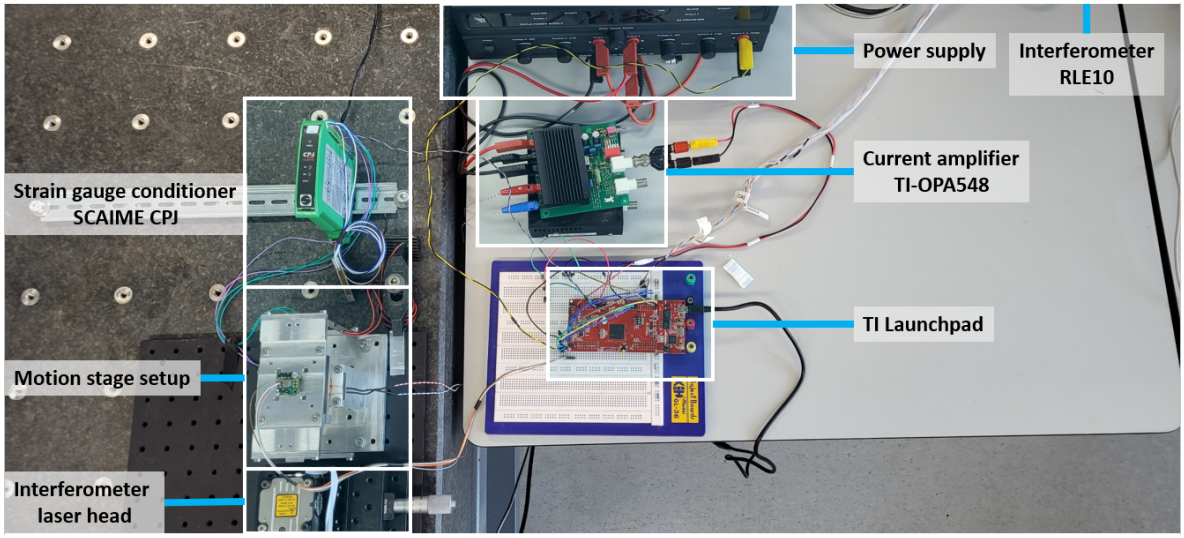

(a) Full setup overview

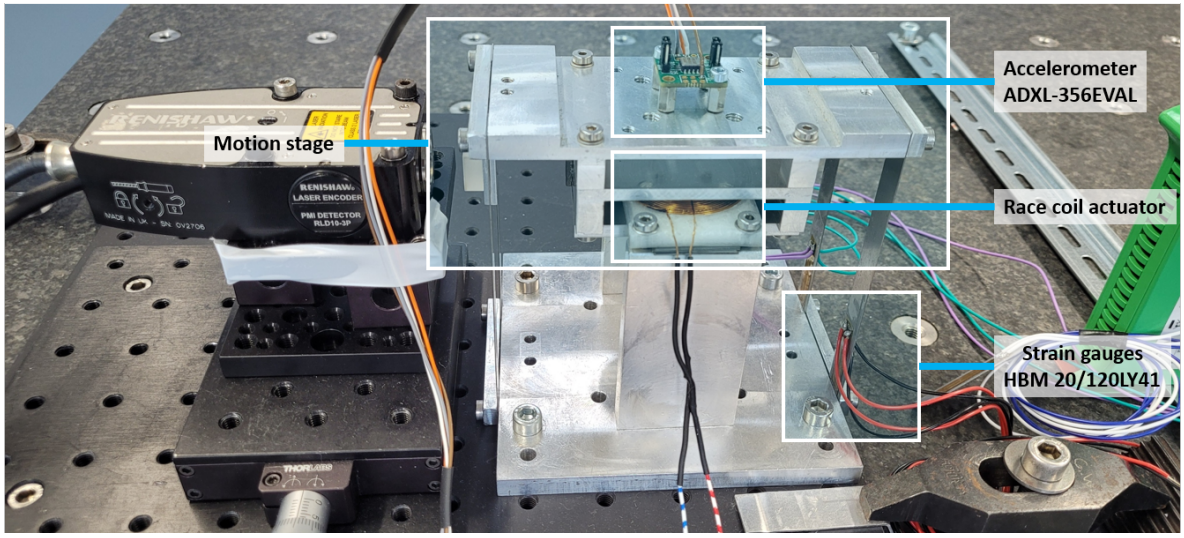

(b) Stage close-up

Figure B-1: Setup and stage overview

B-1-1 Material

Looking at the Euler-Bernoulli model as presented in section 3-1, it is clear only the material specific mass ρ and E-modulus E play a role in the dynamics of the beam. When selecting a material, these two parameters are thus taken into account.

To evaluate the effect of changes in these parameters, the Euler-Bernoulli beam model for one flexure as introduced in section 3-1 is used to sweep through different material properties. Since we would like to look at the observability and location of the modes, the result is shown using a bode diagram from the input force at the tip of the beam to the output strain at one patch located at the base of the beam. The patch location, patch size and other material properties are thus far not important and will merely be kept constant over all evaluations. The resulting bode plots are presented in Figure B-2. Both the E-modulus and specific mass

are varied between the values for aluminium and spring steel, where the constant material is kept at the value for spring steel.

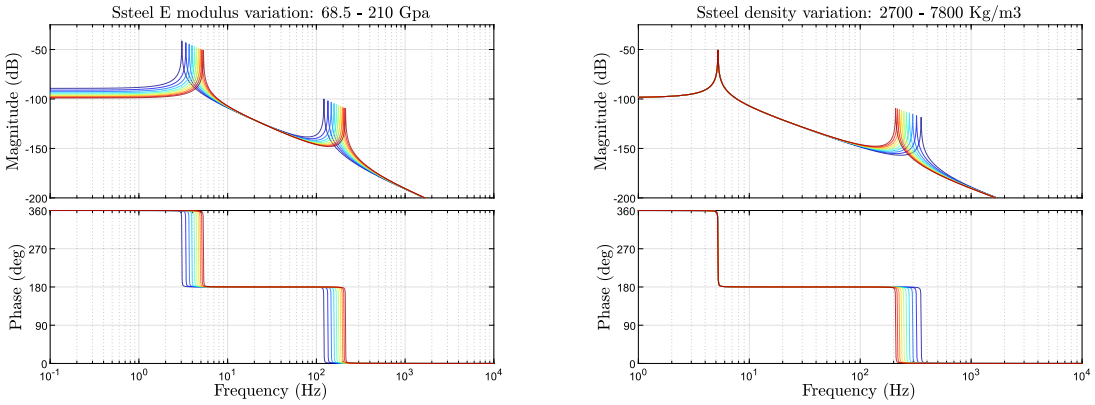

(a) Flexure E modulus variation

(b) Flexure specific mass variation

Figure B-2: Material property evaluation. Here, the red plots correspond to the highest value, while the blue plot correspond to the lowest value.

One interesting observation can be made looking at Figure B-2b. Here, it can be seen that the specific mass of the flexure material solely impacts the location of the second mode. This intuitively makes sense as the modal mass of this mode changes. The location of the first mode is dominated by the mass of the stage at the tip of the flexure, and is thus not influenced much by the change in specific mass. To increase the observability of the second mode or increase its magnitude in the output, a higher specific mass is thus preferred.

From Figure B-2a, It is clear the stiffness of the beam influences the entire dynamics similarly. To increase observability of the second mode a less stiff material is preferred as shown by both peaks increasing in amplitude and moving to lower frequencies. This however can also be achieved by tuning reducing the flexure thickness as presented in the next section. The choice is made to use spring steel for flexure construction due to the higher specific mass, and thus the improved location and amplitude of the second vibrational mode.

B-1-2 Dimensions

In addition to the material properties, the flexure dimensions also need to be selected. To do so, similar parameter sweeps are done over the flexure length in Figure B-3a, flexure width in Figure B-3b, flexure thickness in Figure B-3c and the mass of the stage in Figure B-3d.

Again aiming to increase the observability of the second mode, it can be seen that the width of the flexure presented in Figure B-3b does not have significant impact. The mass of the stage also influences only the location of the first mode, bot does not influence the location of the second mode at all. Here however, the amplitude of the second mode is impacted. It can be concluded that, to increase observability of this second mode, a lighter stage is preferred.

For the length of the flexures as shown in Figure B-3a, it is clear the location and amplitude of all dynamics is influenced similarly. From this point of view, longer flexures are thus preferred.

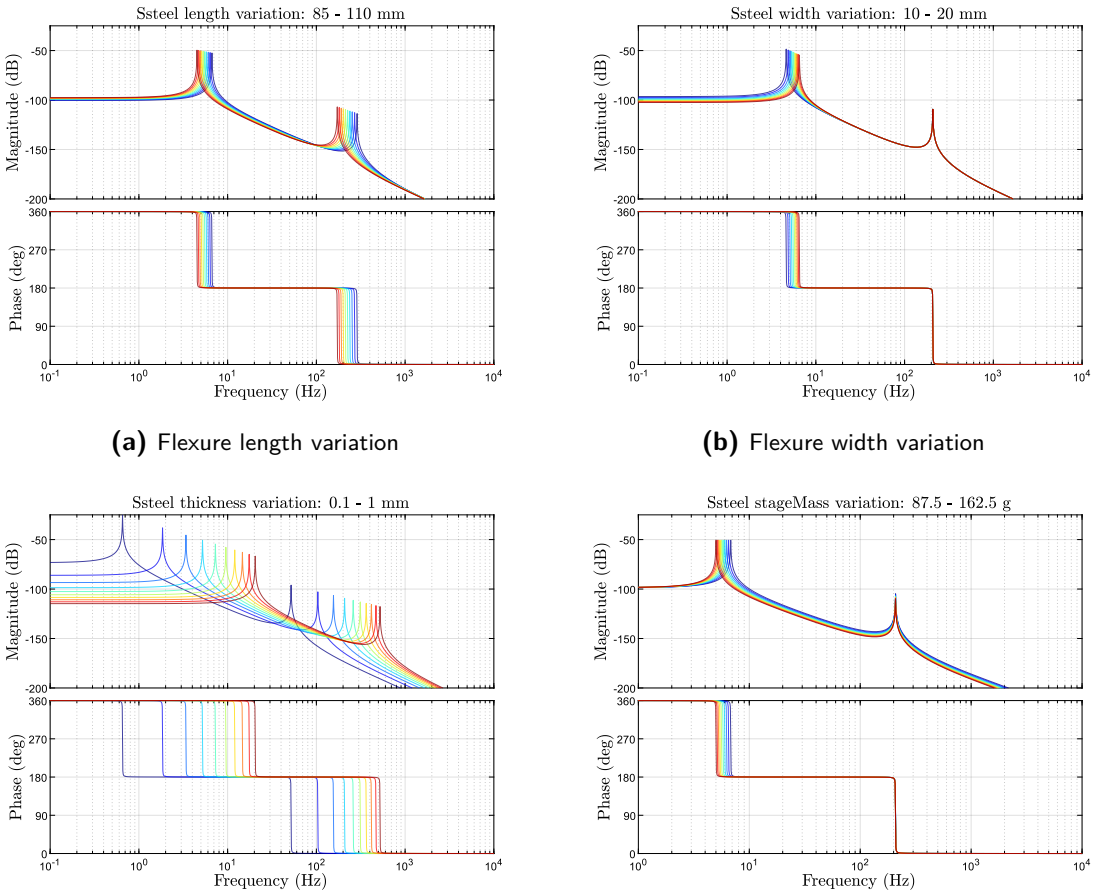

(a) Flexure length variation

(b) Flexure width variation

(c) Flexure thickness variation

(d) Stage mass variation

Figure B-3: Material property evaluation. Here, the red plots correspond to the highest value, while the blue plot correspond to the lowest value of the respective parameter.

As mentioned before, the thickness of the flexures as shown in Figure B-3c influences the location and amplitude of the dynamics significantly as this influences the total stiffness and modal mass of both modes. In general it can be concluded that thinner flexures are more beneficial for the observability of the mode shapes.

To determine the final dimensions, additional limitations in manufacturability and availability need to be taken into account. Since Width does not influence the location or amplitude of the modes, it is arbitrarily fixed. For the thickness of the flexures, thinner flexures are more beneficial for this setup as shown before. Here however, nonlinear effects like buckling or lateral stiffness loss could arise, which are not modelled in the Euler-Bernoulli beam model. A full analysis of the impact and magnitude of these effects has not been made, instead slightly thicker flexures have been chosen to reduce the risk of these effects introducing the accuracy of the linear model.

The final dimensions and material are summarised in Table B-1.

The mass of the stage is reduced to be as light as possible to around 300g which is carried by

Material	AISI 1095 Spring Steel
Length	100 mm
Width	12.7 mm
Height	0.4 mm

Table B-1: Final dimension and material choice of motion stage guiding flexures

4 flexures where each flexure is thus assumed to carry around 75g.

For manufacturing, a roll of *Jeveka Folieband FOBAND100400204* is used clipped to length and punched. Due to the steel being shipped on rolls, there are some remnant stresses which cause the flexures bend slightly when not mounted. This problem however is adressed by mounting the flexures in opposite orientation such that the deformations cancel each other overall. The residual stresses are assumed modelling errors as these can not be modelled correctly.

B-2 Actuation

To actuate the setup in the motion direction, a race coil lorenz actuator is used. This actuator was already implemented before the setup was used for this project, so no design choices were required. The coil is driven by a current amplifier with a TI-OPA548 high current operational amplifier at it's heart. A simplified schematic for the amplifier is shown in Figure B-4.

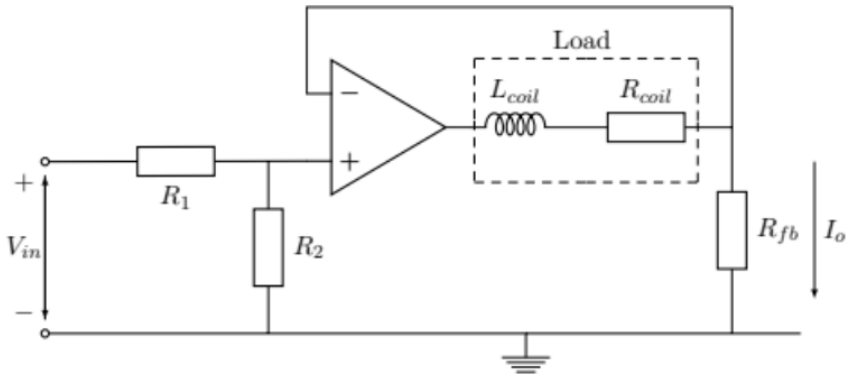

Figure B-4: Current amplifier simplified schematic

This amplifier together with the race coil can be seen in Figure B-1. The amplification factor for this setup can be found by evaluating

$$\frac{I_0}{V_{in}} = \frac{R_2}{(R_1 + R_2)R_{fb}}, \tag{B-1}$$

which computes to $\frac{I_0}{V_{in}} = 0.0625$ A/V for this setup.

The op-amp is powered by a dual $\pm 10V$ power supply limited to $2A$. The control signal used is generated by two analog outputs from the TI Launchpad as introduced in section B-4 and used as differential voltage to generate a $\pm 3.3V$ signal which ends up proportional to the

output current of the current amplifier at $10V$. The amplifier provides constant gain and 0 phase up until its cut-off frequency at around 10kHz, which is sufficient for the control of this system.

Since the amount of coil windings, and the strength of the magnetic field the coil is in is not exactly known, the control current can not directly be converted into a control force. The model does however assume a force input, instead of the current input. To overcome this, the coil and Lorenz force are assumed linear, and modelled by a static gain. The system is identified from the input current to the stage position, and compared to the expected model from the input force to stage position. The magnitude difference is assumed to correspond to this correcting gain, and is thus used as calibration for the input force. By assuming this, an input force can be provided that should correspond to the system model as introduced in section 3-1.

B-3 Sensing

As it is desired for the stage to have position control to be able to reject outside disturbance inputs and provide a trajectory to follow, a position measurement is required. This position measurement is elaborated on in subsection B-3-1. For the state estimation itself, acceleration and strain measurements along the beam are presented in subsection B-3-2 and subsection B-3-3.

B-3-1 Position

For position measurement, a RENISHAW RLE10 fibre optic laser encoder is used. This interferometer is paired with a RLD10-3P laser head located next to the stage setup as also presented in Figure B-1. The laser module and encoder itself is located off to the side but connected with a fiber optic and electronics cable. The laser head reflects off of a mirror mounted rigidly to the motion stage as presented in Figure B-5. The principles of interferometry will not be elaborated on here.

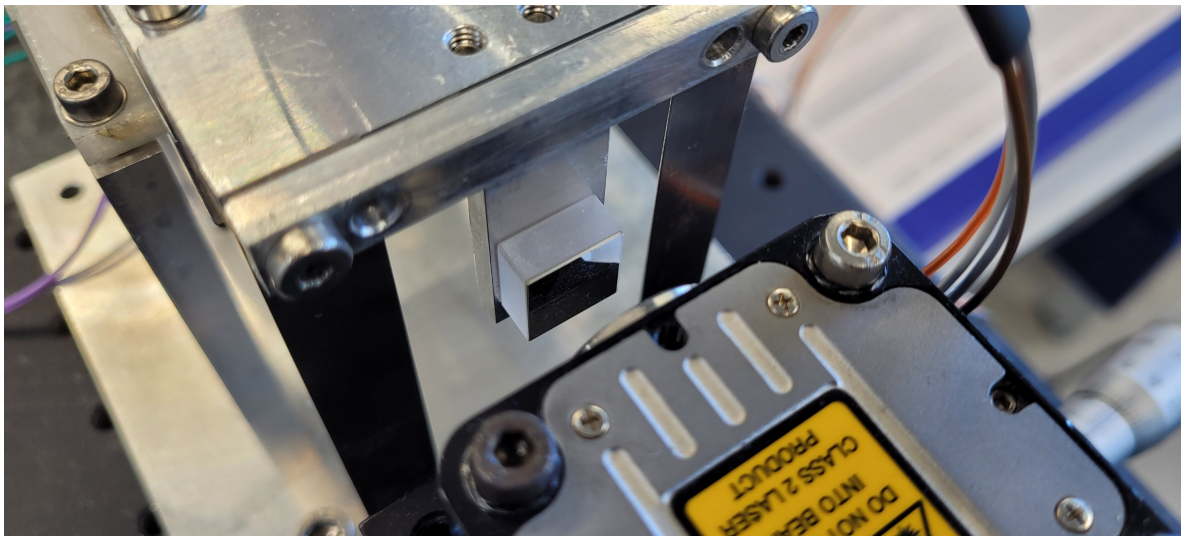

Figure B-5: Interferometer mirror and laser head mounting locations.

The interferometer itself is configured for its maximum update speed of 20Mhz. As the stage can move quite fast, and the resolution of the interferometer can be set fairly small. This reduces the risk of overspeed errors, where the stage is moving too fast for the update rate of the interferometer and steps are skipped. Instead, overspeed is detected in software at the control board which can then be dealt with appropriately without the interferometer itself providing errors and possibly destabilising the feedback system. For the position measurement, the resolution is set to 39.5nm which gave a good balance between accuracy and required control speed.

The output used to connect the interferometer to the TI Launchpad as introduced in section B-4 is set to a digital quadrature signal. Here, only the 'fine A quad', 'fine B quad' and '0V DC' lines are routed to the TI Launchpad as this is sufficient to reconstruct the encoder signal. This connection is also presented in section B-4. Error lines and Z pulses are not read out. These lines all communicate on an RS422/485 digital line transmission standard, and are read out by the dedicated eQEP module on the TI Launchpad [39]. No power or analog cables are shared between the two devices to reduce risk of ground looping or noise transfer.

To analyse noise characteristics for the position measurement, the stage is locked into place with respect to the laser module, and the entire setup is placed on an active vibration isolation table. This is done to eliminate any true signal that might be measured, leaving only measurement noise. Multiple measurements are done, which all result in a zero deviation from the initialised position. This thus results in a noise covariance of about

$$\sigma_{\text{pos}} \approx 0 \quad \text{m}^2, \tag{B-2}$$

which is also to be expected. Such a clean measurement could be due to the working principles of interferometry and the resolution the encoder is set to. For filter calibration however, the covariance is increased from zero to a numerically zero value to avoid rank deficient covariance matrices.

B-3-2 Acceleration

For the acceleration, the choice is made to place only one accelerometer at the tip of the flexure. This location is assumed to be rigidly connected to the stage, which allows for placing the accelerometer on top of the stage body. This allows for the use of a PCB mounting.

The choice of accelerometer relies mostly on range, noise level, measurement axis and bandwidth. For this choice, the possibility of mounting the accelerometers to the flexures themselves is taken into account. This is important since the center of the flexures will see much higher accelerations due to the second mode observability then the stage itself will. The range and bandwidth are thus selected based on the center of the flexures. It is also important for the accelerometer to be able to measure in Y direction (out of plane) for these possible flexure mounted measurements.

For this, simulation has shown a maximum acceleration of about 10g at large excitation. Since the ranges are only selectable at 1, 10 and 20g, 20g is chosen. Similarly, the dynamics of the second mode shape of the system will be at around 200Hz, requiring at least a 2Khz sampling rate, which thus also sets a lower limit on the bandwidth. The noise level is chosen as low as possible, but obedient to the previous two requirements. In addition to this, the possibility of measurement in the Y axis is also important.

As mentioned, the accelerometer used is the *Analog instruments ADXL356* with its main characteristics summarised in Table B-2.

Bandwidth	2.4	kHz
Range	20	g
Noise level	75	$\frac{\mu g}{\sqrt{\text{Hz}}}$

Table B-2: ADXL356 main characteristics

To mount the accelerometer rigidly to the stage, the EVAL version is used which is pre-mounted to a stiff PCB with additional connector options. The final mounting of the accelerometer is presented in Figure B-1. For the connections, Figure B-10 presents the required power and signal lines to the TI-Launchpad.

To evaluate the actual performance of the accelerometer in the setup, again the setup is fixed and placed on an active vibration isolation table. The resulting noise sequence and autocorrelation function are presented in Figure B-6.

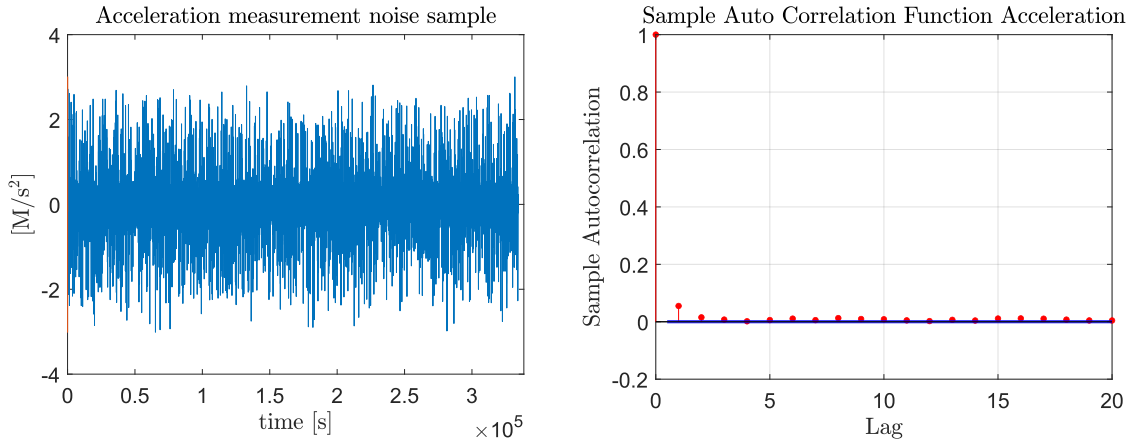

(a) Acceleration noise sequence

(b) Acceleration noise auto correlation

Figure B-6: Noise characteristics acceleration measurement

From this, it can be seen that the true covariance of the measurement is about

$$\sigma_{\text{acceleration}} \approx 0.05142 \quad \text{m/s}^2, \tag{B-3}$$

which is significantly higher then the manufacturers specification as provided in Table B-2. Due to time constraints, this problem has not been resolved, and the acceleration measurements could not be implemented. Instead, the measured position is derived twice and passed through a 2Khz low-pass filter in order to still simulate acceleration measurements.

B-3-3 Strain

For the strain measurements, resistive strain patches have been used. This is mainly done to avoid modelling complexities that are associated with modelling piezoelectric patches. Also the goal of this work is not actual actuation or active vibration control, but merely

state reconstruction. This relaxes the need for actuation, further substituting the choice for resistive strain gauges.

To find proper size and placement for the strain gauges, an objective function for optimisation is required. For this, the observability of the second mode shape through the strain gauge is used. This is done by evaluating the bode magnitude plot from the input force to the strain measured by a strain gauge. Varying the length and placement of the patch, the height of the resonance peak changes, which is proportional to the observability of the second mode through the patch. This 2D surface is presented in Figure B-7 where the magnitude of the second mode shape is plotted on the z axis, the length of the patch on the x axis, and the position of the bottom of the patch at the y axis.

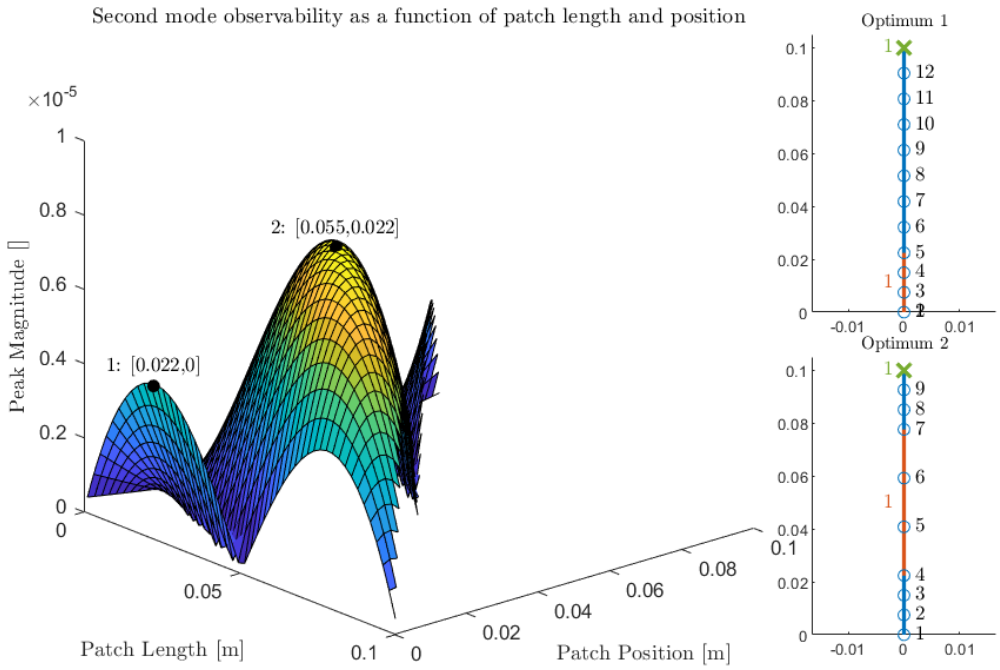

Figure B-7: Patch optimisation cost function and locally optimal configurations.

As the total flexure length is 100mm, configurations where the patch length plus the patch position exceed this length are not feasible, and are thus not plotted. To find the local optima, a Nelder-Mead nonlinear optimisation algorithm is used. From a plot of the objective function, it can be seen there are three local optima in total, of which two are annoted. On the right of Figure B-7 the physical configuration is also plotted.

As can be seen, the first optimum corresponds to a small patch at the bottom of the flexure. This optimum is offcourse mirrored to the top side corresponding to the third optimum (not plotted). The second optimum however corresponds to a large patch over the center of the flexure, and should correspond to exactly twice the peak height as the other two optima. From this plot, the second optimum seems the most desirable as this configuration has the largest observability of the second mode shape. The first optimum is however chosen. This is done to keep the option of acceleration measurements at the center of the beam open. This

would not be possible when a strain gauge is placed over the center of the flexure.

It is noteworthy however that a configuration using a large strain gauge in the center (at the second optimum), and two piezoelectric patches at the edges (at the first and third optimum) would provide a good compromise for a full active vibration control scheme, as this would allow for high observability, and controllability of the second mode shape. This however is future work as it is not explored here.

Staying close to the optimal dimensions chosen, the HBM 20/120 LY41 strain gauge is chosen with a length of 20 mm. The measurement core of the gauge is mounted about 2 mm above the base of the flexure due to space considerations. The final flexure placement is presented in Figure B-8.

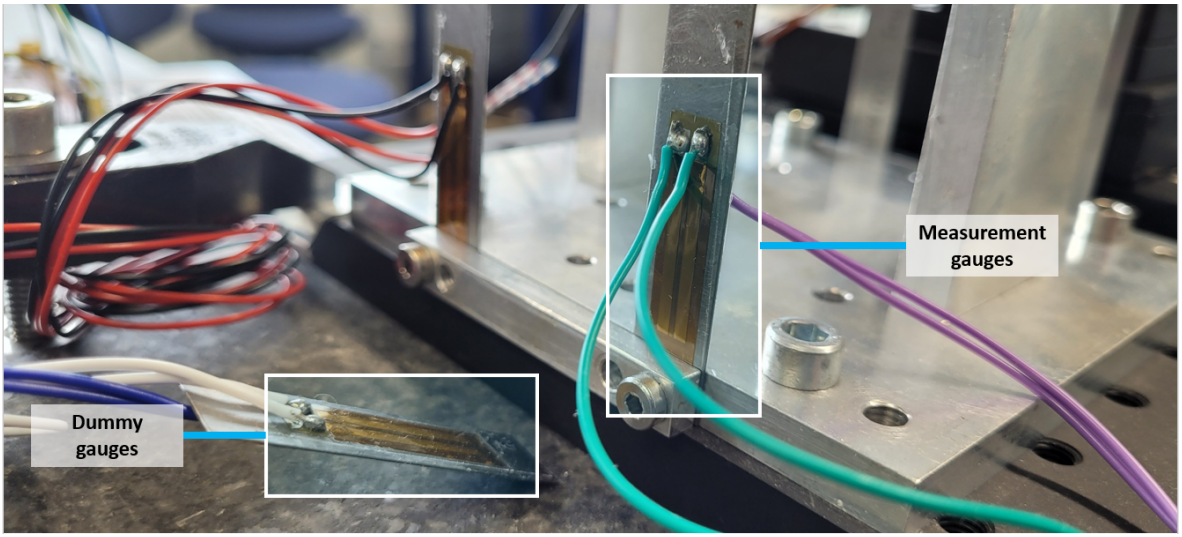

Figure B-8: Mounted strain gauges

To increase measurement signal, and decrease temperature dependency of the strain gauges, they are connected in a full Wheatstone bridge configuration, with half the bridge (2 gauges) placed on a dummy piece of flexure material annotated as 'dummy gauges' in Figure B-8. The other side (the other 2 gauges) is placed on the flexure itself, on either side to have the measured strain add up.These are referred to the 'measurement gauges' in Figure B-8. The bridge is powered, and the output voltage is measured by a SCAIME CPJ strain gauge conditioner. From the conditioner, the current output is passed over a resistor over which the voltage is measured by an analog input of the TI Launchpad as also shown in in section B-4 thus generating an output proportional to the strain measured by the flexures.

Since there is an arbitrary amplification factor between the true strain and the output voltage measured, calibration of the gauges is required. Here however, it is important to note that we are not interested in the true strain of the system, but merely in a quantity that is similar to the model output. This will ensure the model output coincides with the 'strain' measurement. Calibration is thus done by performing system identification from the input force to the quantity measured by thee strain gauges, and comparing this to the model. Multiplying the measurement by the appropriate gain then makes sure they both coincide. Assuming the model outputs true strain, the quantity measured by the strain gauges can then also be called the strain. This however is not strictly necessary.

For the noise characteristics, again the stage is fixed to avoid any true signal in the measurement. The stage is placed on an active vibration isolation table, and a constant signal is measured as shown in Figure B-9a. The covariance on this signal should correspond closely to the noise covariance of the setup which was evaluated to about

$$\sigma_{\text{strain}} \approx 1.095 \cdot 10^{-16} \quad \text{m}^2/\text{m}^2. \tag{B-4}$$

Since the strain measurement is supposed to provide lower noise levels, it is assumed most of this noise is originating from the control board or wired connections. To evaluate the noise slightly further, the autocorrelation for a 20 sample lag is shown in Figure B-9b.

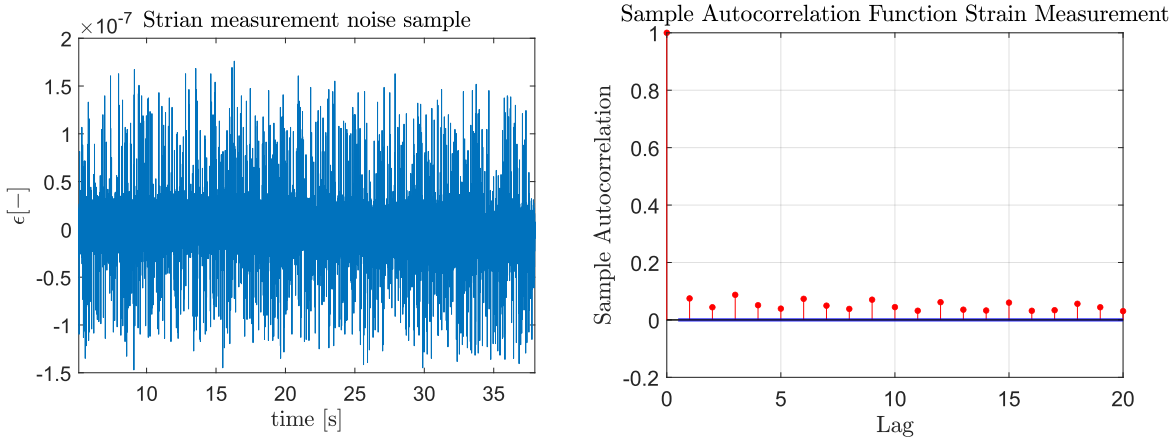

(a) Strain noise sequence

(b) strain noise auto correlation

Figure B-9: Noise characteristics strain measurement

Here, it can be seen that the signal does resemble white noise, but not entirely since the autocorrelation remains somewhat significantly above numerical zero. For this work however, the noise still assumed Gaussian distributed and wide sense stationary.

Since the strain gauges are also incorporated in the system model, their mechanical properties are summarised in Table B-3.

height	0.025	mm
width	12.7	mm
E modulus	10	pa
μ	0.334	-
ρ	1000	kg/m^3

Table B-3: Strain gauges mechanical properties

B-4 Micro controller board

For previous projects within the MSD group, an FPGA based NI compactRIO was often used. For this however, a steep learning curve in programming NI LABVIEW and high compilation times often unnecessarily elongated implementation times. To investigate whether this can be circumvented using non-FPGA based micro controller solutions, the TI TMS320F28379D

Launchpad XL as shown in Figure B-10 is used here. The board itself is oriented towards real-time closed loop control, and is developed as prototyping kit for the TI-C2000 real-time control chip.

In the context of this work, the board is mainly used for closed loop position control for the stage, and data acquisition of the additional sensors. The implementation is oriented towards the possibility to run closed loop active vibration control in addition to the already implemented position control. To elaborate on the current implementation this section first presents the hardware side and connections in subsection B-4-1. This section also presents the way all sensors and actuators presented in section B-3 and section B-2 are connected to the control board. The software side of the setup is then elaborated on shortly in subsection B-4-2. Here, the main purpose is repeatability, and presenting the software used for closed loop control and data acquisition.

B-4-1 Hardware

As shortly presented above, a F28793D TI-Launchpad XL is used here. A graphic representation of the board in general is shown in Figure B-10. The main features of the board and further documentation can be found in [39]. As mentioned, the board is oriented towards real-time control and prototyping using the TI-C2000 microprocessor. For this, the board offers multiple GPIO pins and configuration possibilities. Figure B-10 presents the connection and configuration diagram for the launchpad in the setup.

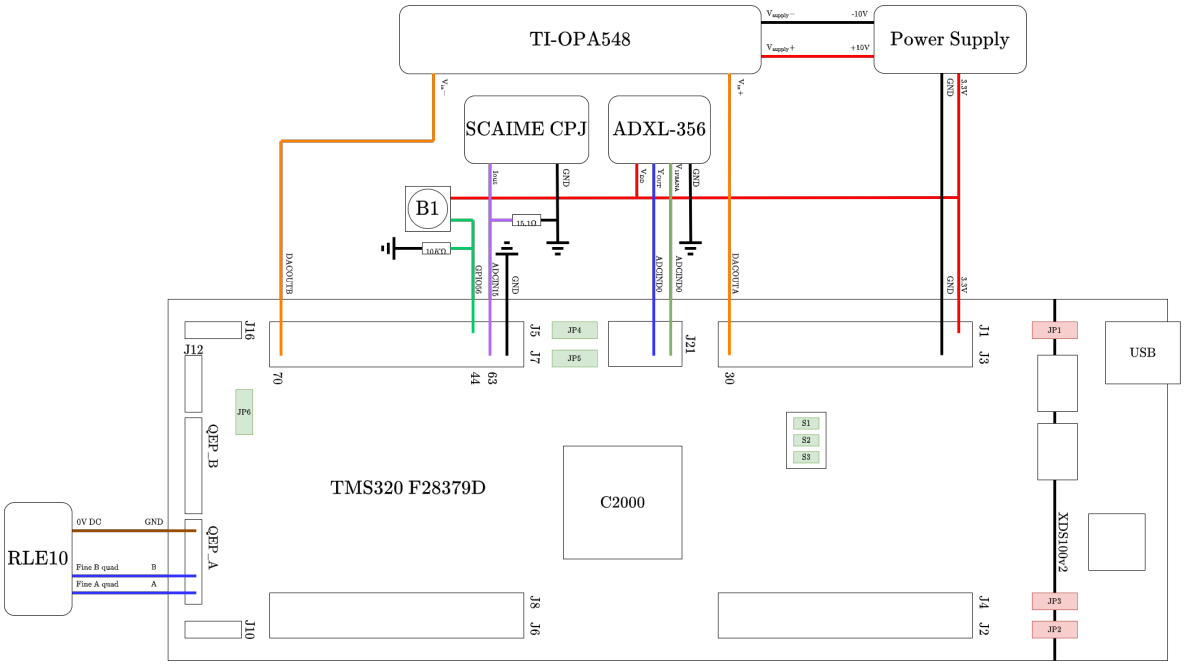

Figure B-10: Launchpad connections to peripheral hardware and configuration

Here, it can be seen the board is powered through the 3.3V output of the power supply, allowing for the decoupling of the power from USB. This reduces the effect of 50Hz noise through the USB power. For this, jumper JP1, JP2 and JP3 need to be disengaged. This

decouples the debugging probe power from the board itself. The probe is now purely optically decoupled and does not share any power with the board. A PC is still connected to the setup through the USB hub for data acquisition. This however does not provide any power to the board itself, only the debug probe. To be able to power the board from a 3.3V input, the on-board step-up converter needs to be enabled to also power the 5V rail from the 3.3V input. This is done by enabling jumper JP6 which is not enabled by default. JP4 and JP5 enable the 3.3V and 5V GPIO output pins, and thus also need to be enabled. The switches S1, S2 and S3 are left in their default position to always boot from flash.

The peripheral hardware connections are also shown in Figure B-10. Here, in addition to the earlier mentioned hardware, push button B1 is also connected to be able to interact with the software. This is eventually set up to turn on or off closed loop position control for the stage. The sensors and actuator connections in Figure B-10 show the connection location on the board's side and on the device side on the connection lines for clarity.

B-4-2 Software

To be able to reproduce the results presented in this work, the software side of the setup also needs to be elaborate don slightly. All code and simulink files can be found in the github repository on the master branch at [22]. The README should be sufficient to get started with the setup, additional information will be provided in this section.

As generously discussed previously, the setup utilises the TI C2000 real-time control chip implemented on a TI Launchpad development kit. This micro controller allows for dual core operation with two computational cores and two additional control law accelerators (CLA's). In this work, only one core will be used, but setup is made for the use of additional cores to run the filters and full active vibration control loop in real-time. The software used, as well as the scripts and files to get the system running will be elaborated on by first giving a general overview, then explaining the position control implemented whereafter the data acquisition process is elaborated on shortly.

General

The C2000 microprocessor family requires programming in the C or C++ language through the Texas Instruments IDE named Code Composer Studio (CCS). To simplify prototyping, and allow for programming through MATLAB, the embedded coder and simulink coder add-ons can be used in simulink to generate the C or C++ code from simulink models. This allows for programs to be designed in simulink, converted to C code by the simulink coder, and again converted to code for the embedded system by the embedded coder support package. This code is then exported through CCS to be compiled into machine code that can be run on the hardware itself. In addition to this workflow, TI and mathworks provide additional blocks in the embedded coder support package to enable and use features of the devopment kits through simulink, allowing for a full prototyping and developing experience in simulink. The main code will thus be presented as simulink files.

The main code that is run on core 1 (cpu1) of the C2000 processor serves several functions and is presented in Figure B-4.

The main goals this script achieves is closed loop reference tracking of the stage position and data acquisition of all additional sensors.

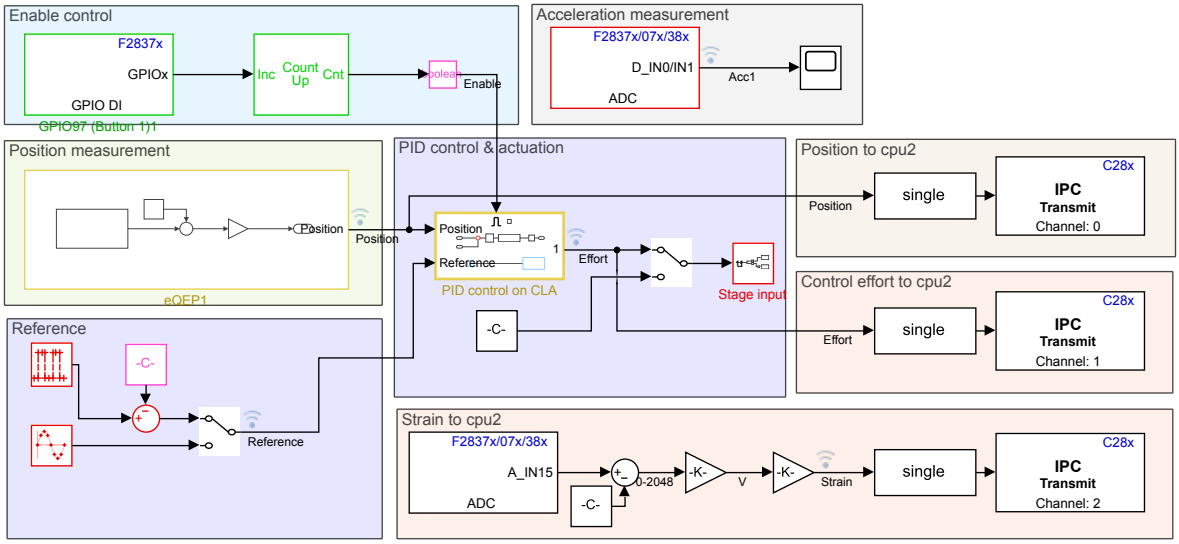

Figure B-11: Main control scheme for the launchpad

Position control

For position control, a relatively simple PID position controller is implemented in the center area in Figure B-11. The reference is generated in the lower left block, and can be selected as required. To actually provide inputs to the stage, the stage input subsystem is used. Here, polarity of the two DAC modules is switched based on the sign of the input signal since a differential signal is required. The actual PID control law is evaluated in the PID control subsystem which can be switched on or off by the enable control area. This area latches a push button to allow a user to interface with the code.

Data acquisition

In addition to position control, this file also handles data acquisition for the purpose of logging, and also real-time state estimation. For logging, the simulink data inspector is used, where interesting signals are selected for logging and recorded by the PC over an XPC on serial connection. For real-time state estimation, the signals required are also passed to the second CPU core through the IPC transmission blocks on the right of the file. Here, these signals are placed on local RAM locations, from where they can be picked up by the second CPU core. At this point, CPU2 does not run any real-time code as this was deemed outside the scope of this work.

Appendix C

Data sets

This chapter presents the data sets used for calibration and validation of the filters. The true data sets can be found in the GITHUB repository on [22]. This appendix merely provides a visual representation for completeness and clarity.

C-1 Training data set

For the training data set a 15s long closed loop sequence is chosen in which the stage is in closed loop control to ensure sufficient acceleration and strain excitement.

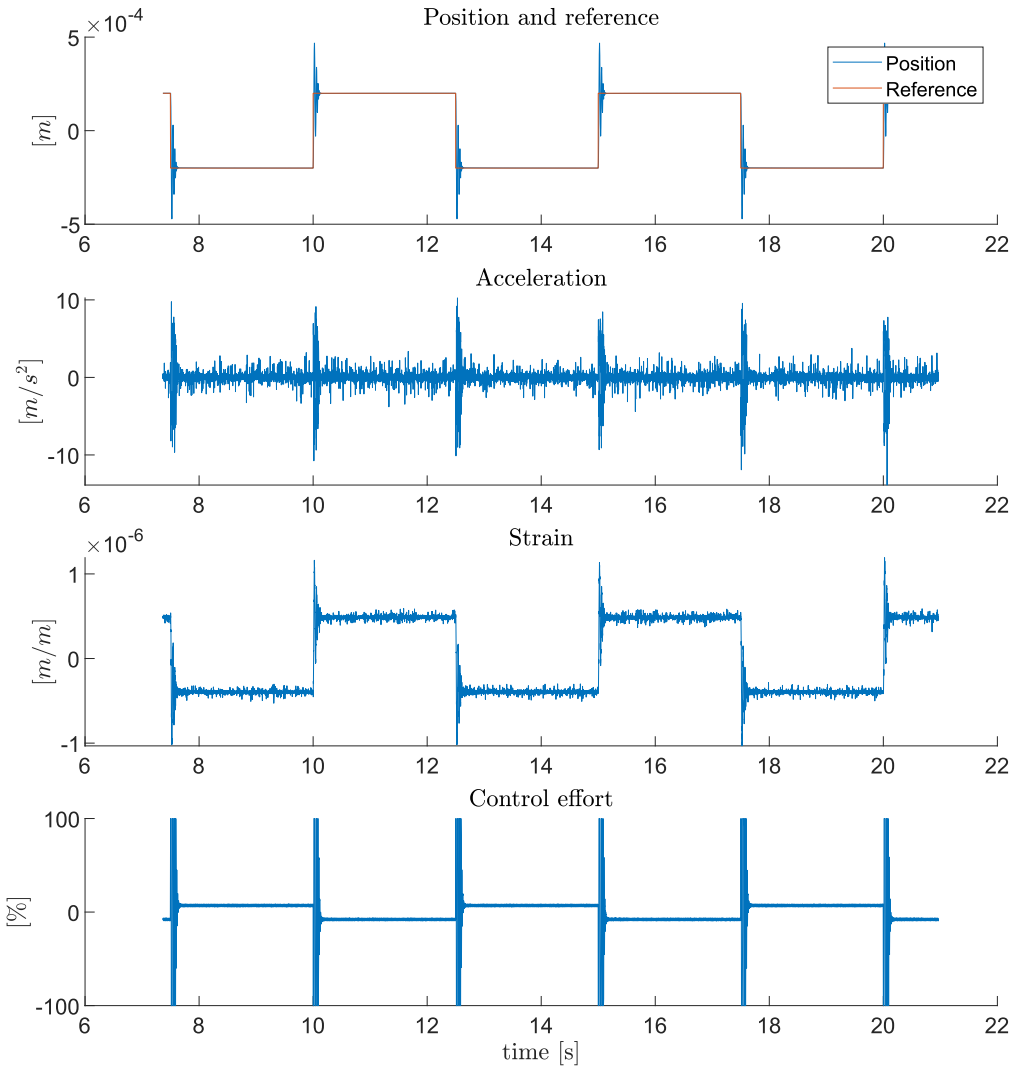

Figure C-1: Training dataset

C-2 Validation data sets

For the validation data sets, four scenarios are chosen. Two in which the stage is in closed loop control, and two in which the stage is in open loop control, and perturbed by an impulse excitation. All data sets are about 50s long, contain the same signals and have the same sampling rates. They have been recorded within a short period of time to reduce time varying

influences.

C-2-1 Closed Loop 1

Here, the stage is initiated in open loop, where control is applied from about 15s onward. During this period, the stage is required to follow a block signal reference for some cycles through closed loop PID control. Hereafter, control is removed, and the stage is allowed to dampen out naturally.

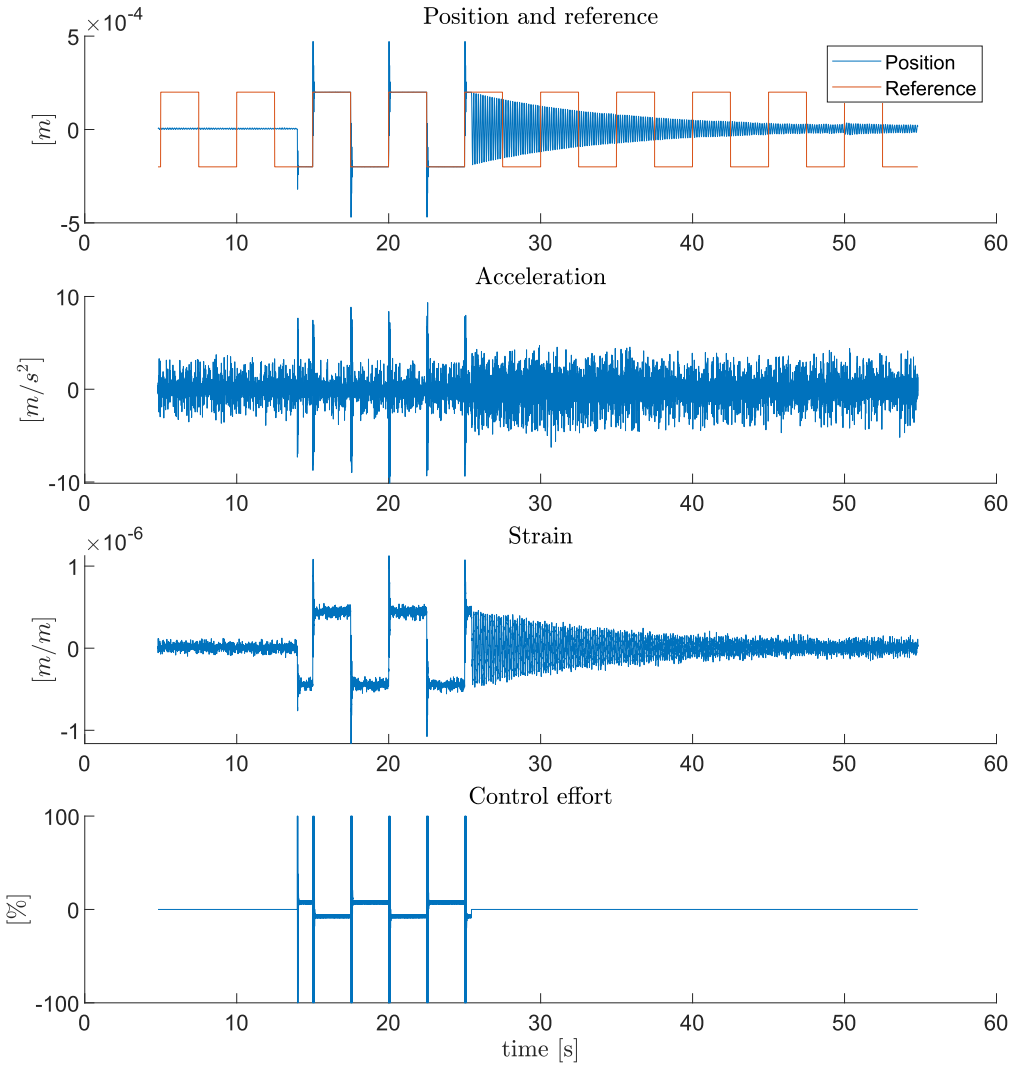

Figure C-2: Closed loop 1 data set

C-2-2 Closed loop 2

Here, the stage is again initiated in open loop whereafter control is applied at about 10s. The reference signal now contains a sinusoidal wave of about 10Hz and is kept for about 10s whereafter control is removed, and the stage is allowed to dampen out.

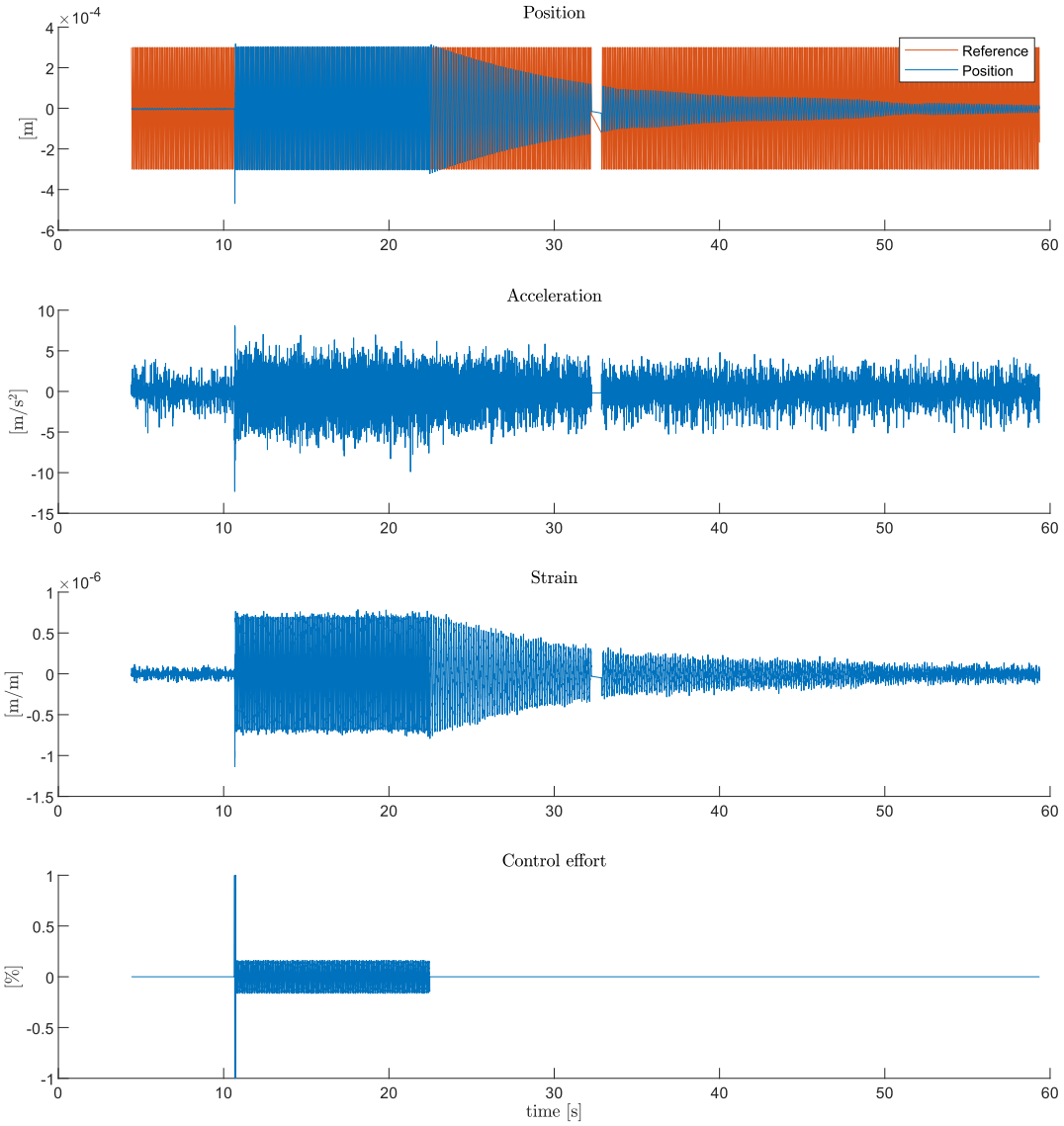

Figure C-3: Closed loop 2 data set

C-2-3 Open Loop 1

For the open loop data sets, no closed loop control is used. The stage is perturbed with an impulse of 100% control effort at 10s whereafter it is allowed to naturally dampen up until about 50s.

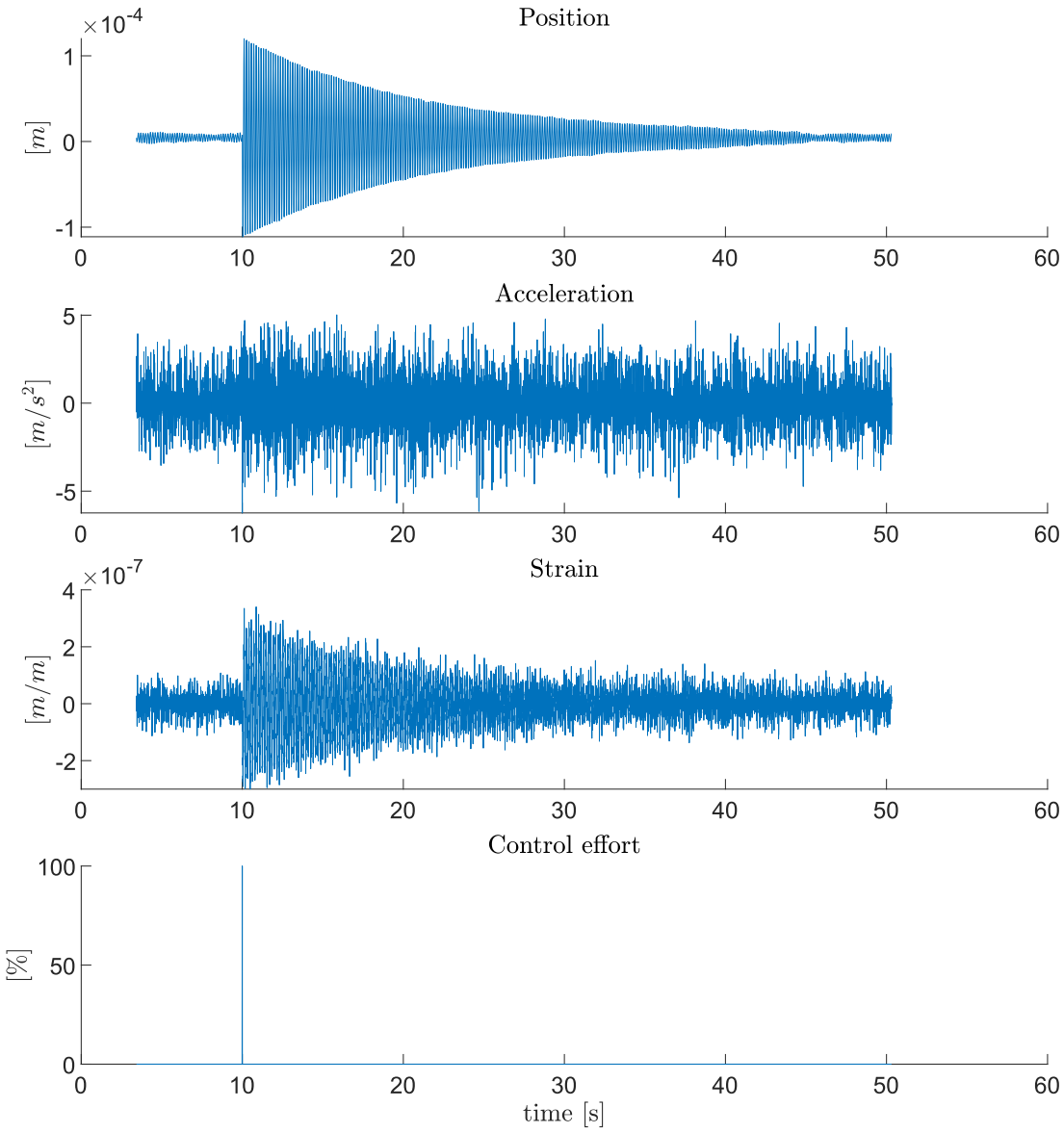

Figure C-4: Open loop 1 data set

C-2-4 Open Loop 2

The same scenario as open loop 1 presented in subsection C-2-3.

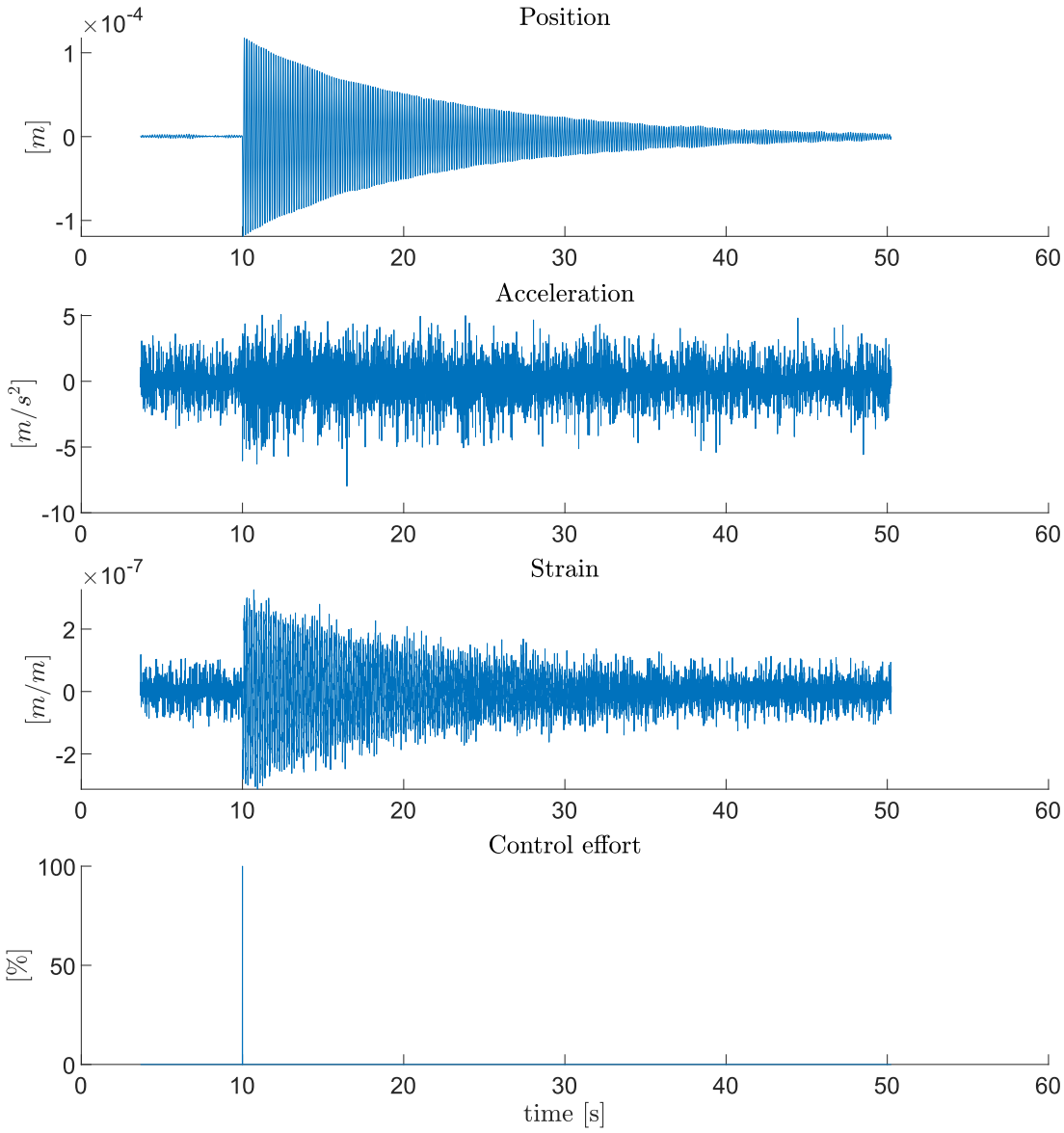

Figure C-5: Open loop 2 data set